

Ricardo Baiotto

**Métodos de imagem aplicados em dados de
ultrassom *phased array* de soldas austeníticas e
cladeados**

**Imaging methodologies applied on phased array ultrasonic data from austenitic welds
and claddings**

Porto Alegre

August 2018

Ricardo Baiotto

**Métodos de imagem aplicados em dados de ultrassom *phased*
array de soldas austeníticas e cladeados**

**Imaging methodologies applied on phased array ultrasonic data from austenitic welds
and claddings**

Trabalho realizado no Departamento de Metalurgia da Escola de Engenharia da UFRGS, dentro do Programa de Pós-Graduação em Engenharia de Minas, Metalúrgica e de Materiais –PPGE3M, como parte dos requisitos para obtenção do título de Doutor em Engenharia. Área de Concentração: Ciência e Tecnologia dos Materiais

MINISTÉRIO DA EDUCAÇÃO

UNIVERSIDADE FEDERAL DO RIO GRANDE DO SUL

Escola de Engenharia da Universidade Federal do Rio Grande Sul

Programa de Pós-Graduação em Engenharia de Minas, Metalúrgica e de Materiais –
PPGE3M

Supervisor: Thomas Gabriel Rosauero Clarke

Porto Alegre

August 2018

Ricardo Baiotto

**Métodos de imagem aplicados em dados de ultrassom *phased*
array de soldas austeníticas e cladeados**
**Imaging methodologies applied on phased array ultrasonic data from austenitic welds
and claddings**

Trabalho realizado no Departamento de Metalurgia da Escola de Engenharia da UFRGS, dentro do Programa de Pós-Graduação em Engenharia de Minas, Metalúrgica e de Materiais –PPGE3M, como parte dos requisitos para obtenção do título de Doutor em Engenharia. Área de Concentração: Ciência e Tecnologia dos Materiais

Trabalho aprovado. Porto Alegre, 23 de agosto de 2018:

**Prof. Dr Thomas Gabriel Rosauro
Clarke**
Orientador

Prof. Dr Elineudo Pinho de Moura
UFC

Prof. Dr Julio Cezar Adamowski
USP

Dr Ricardo Callegari Jacques
UFRGS

Porto Alegre
August 2018

Acknowledgements

I would like to express my gratitude to my family and friends for all the help and dedication I have been receiving during all my life, without them nothing of this would be possible. I would like to thank Prof. Dr Thomas Clarke for his supervision through my doctorate research and for the opportunity to undertake my doctoral studies at LAMEF. Furthermore, I am deeply grateful to my colleagues at LAMEF for all the friendship and assistance. I also very much appreciate the financial support given by CNPq and Shell, which made it possible to spend a year at TWI Ltd. Also, I am thankful to TWI Ltd for making its facilities available for my research and to my colleagues there, whose insights made my work progress much more smoothly. Special thanks are due to Dr Channa Nageswaran for his supervision and support during and after my time in TWI Ltd and to Dr Benjamin Knight-Gregson for valuable insights on coherence weights. Finally, I would like to give warm regards to everyone who participated and collaborated with the present work.

Abstract

The increasing trend to use austenitic welded and cladded materials in critical components employed in some industrial sectors, such as the oil&gas and nuclear industries, leads to an increasing demand for their non-destructive assessment by reliable non-destructive methods. Among the methods used to assess the integrity of austenitic welds and claddings are the Ultrasonic Phased Array methods, which are usually used to detect the presence and determine the position of defects. However, austenitic welds and claddings are challenging to inspect with Phased Array methods due to the anisotropy and inhomogeneity caused by their coarse grain microstructure, which is capable of increasing noise levels, misplace indications and create false indications. Therefore, the selection of an appropriate phased array method needs to take into account the method's ability to overcome the impairment caused by anisotropy and inhomogeneity. This thesis presents two non-conventional methods based on ultrasonic phased array imaging techniques designed to assist the structural integrity assessment of components where austenitic welds and clads are present. Both proposed methods are based on the *Total Focusing Method* (TFM); the first approach is an expansion of the adaptive delay laws concept named *Adaptive Delay Total Focusing Method* (ADTFM), while the second method uses the coherence weights combined with the TFM images. From the imaging methods applied it was possible to significantly increase the quality of the ultrasonic images in comparison with the standard TFM, primarily when it was possible to combine both approaches.

Keywords: Austenitic welds, Total Focusing Method, Full Matrix Capture, Coherence weights.

Resumo

A crescente tendência de utilização de materiais austeníticos soldados e cladeados em componentes críticos em alguns setores industriais, como nas indústrias de óleo&gás e nuclear, leva a um aumento na demanda sobre ensaios não-destrutivos confiáveis na avaliação de sua integridade estrutural. Dentre os métodos utilizados na inspeção de soldas cladeados austeníticos estão os métodos de ultrassom por *phased array*, que são normalmente utilizados na detecção e localização de defeitos. No entanto, componentes com esse tipo de microestrutura são difíceis de inspecionar por *phased array* devido a anisotropia e inomogeneidade causadas pela microestrutura de grãos grosseiros que costumam levar ao aumento do nível de ruído, ao deslocamento de indicações e ao surgimento de indicações falsas. Sendo assim, a seleção de um método de *phased array* apropriado precisa levar em conta a habilidade do método em superar os problemas causados pela anisotropia e inomogeneidade. Esta tese apresenta dois métodos de imagem por phased array ultrassônico não-convencionais pensados como formas de ajudar na determinação da integridade de componentes onde soldas e cladeados austeníticos estão presentes. Ambos os métodos tem como base o método de foco total (TFM), sendo que o primeiro é uma extensão do método de leis de atraso adaptativas chamado Método de Foco Total de Atraso Adaptativo (ADTFM) e o segundo método usa fatores de coerência associado à imagens de TFM. A partir dos métodos de imagem aplicados é possível aumentar significativamente a qualidade das imagens por ultrassom em comparação com as imagens padrão obtidas por TFM, especialmente quando foi possível utilizar ambos os métodos combinados.

Palavras-chave: Soldas Austeníticas, Total Focusing Method, Full Matrix Capture, Fatores de Coerências.

List of Figures

| | |
|--|----|
| Figure 1 – Unit cell for bcc crystals. The crystallographic directions $[100]$, $[110]$ and $[111]$ are indicated. Source: the author. | 26 |
| Figure 2 – Slowness curves for the plane (001) of a cubic crystal of GaAs. The three curves represent the three modes present. 0° is aligned with the $[100]$ direction, while 90° is aligned with the $[010]$ direction. Adapted from Auld (1). | 32 |
| Figure 3 – Slowness curves for the plane (011) of a cubic crystal of GaAs. The three curves represent the three modes present. 0° is aligned with the $[100]$ direction, while 90° is aligned with the $[011]$ direction. Adapted from Auld (1). | 36 |
| Figure 4 – Slowness curves for the plane (111) of a cubic crystal of GaAs. The three curves represent the three modes present. 0° is aligned with the $[\bar{1}11]$ direction. Image created by the author from the stiffness matrix of this material available at (1). | 37 |
| Figure 5 – Slowness surface for the longitudinal mode of GaAs, obtained by the author from the stiffness matrix of this material available at (1). | 38 |
| Figure 6 – Slowness surface for the fast transversal mode of GaAs, obtained by the author from the stiffness matrix of this material available at (1). | 38 |
| Figure 7 – Slowness surface for the slow transversal mode of GaAs, obtained by the author from the stiffness matrix of this material available at (1). | 39 |
| Figure 8 – Illustration of the phase and group velocities in a modulated wave. Source: the author. | 39 |
| Figure 9 – Illustration of the propagation of a wave with different phase and group velocities. Adapted from Auld (1) and Cheeke (2). | 40 |

| | |
|---|----|
| Figure 10 – Illustration of the graphic method to calculate the group slowness curve from the phase slowness curve. $ \mathbf{m}_g $ and $ \mathbf{m} $ are respectively the group and phase slowness moduli, while \mathbf{n}_g is the unit vector perpendicular to the slowness surface and \mathbf{n} is the phase unit vector. Adapted from Connolly (3). | 41 |
| Figure 11 – Slowness group curves plotted as a function of the phase vector for the plane (001) of GaAs calculated from Figure 2 data. 0° is aligned with the [100] direction, while 90° is aligned with the [010] direction. Image obtained by the author from the stiffness matrix of this material available at (1). | 42 |
| Figure 12 – Group slowness surface plotted as a function of the phase vector for the longitudinal mode of GaAs, obtained by the author from the stiffness matrix of this material available at (1). | 42 |
| Figure 13 – Group slowness surface plotted as a function of the phase vector for the fast transversal mode of GaAs, obtained by the author from the stiffness matrix of this material available at (1). | 43 |
| Figure 14 – Group slowness surface plotted as a function of the phase vector for the slow transversal mode of GaAs, obtained by the author from the stiffness matrix of this material available at (1). | 43 |
| Figure 15 – FMC acquisition process. Source: the author. | 44 |
| Figure 16 – TFM imaging process. Source: the author. | 46 |
| Figure 17 – Dual layer media wave path calculation method. Source: the author. | 47 |
| Figure 18 – Illustration of the ADL method. a) adapted time delay calculation from the time of flight and b) adapted time delay used to focus the phased array. Source: the author. | 54 |
| Figure 19 – Diagram showing the steps involved to obtain an ADTFM image. Source: the author. | 62 |

| | |
|--|----|
| Figure 20 – Virtual transducer excitation. (a) Pixel position and (b) illustration of wavefront propagation. The outer boundary of the test piece is considered to absorb the incoming waves perfectly in this illustration. Source: the author. | 62 |
| Figure 21 – Alloy 182 single crystal cylindrical sample used in this work before final machining. The arrow indicates the [001] direction throughout which the crystal grew. Source: the author. | 65 |
| Figure 22 – Pole figures of the single crystal obtained via EBSD indicating that the material is a cubic single crystal. The results are presented with three pole figures for the {100}, {110} and {111} family of crystallographic planes. Source: the author. | 66 |
| Figure 23 – Scanning electron microscopy of the single crystal. The plus sign structures are cross-sections of individual dendrites with the main growth direction perpendicular to the picture’s plane. Source: the author. | 67 |
| Figure 24 – Top view showing the geometry of the simulation run in CIVA. The transducer is aligned with the centre of the single crystal, and the set up is immersed in water. On the bottom left, there is a 3D representation of the geometry. Source: the author. | 68 |
| Figure 25 – A-scans simulation results for the [100] direction facing the transducer (a) and in-plane rotations of 15° (b), 30° (c) and 45° (d) from the orientation in (a). The last one corresponds to the [110] direction facing the transducer. Source: the author. | 69 |
| Figure 26 – Ray paths able to enter the single crystal and come back to the transducer for four crystallographic orientations facing the probe. The black cone represents the incident beam, while the green lines represent the refracted rays. The arrows are in the direction [100], and the angles between them and the horizontal line are indicated at the bottom of each image. Source: the author. | 70 |

| | |
|--|----|
| Figure 27 – Schematic drawing of the experimental set-up used to measure the ultrasonic velocities on the axial directions of the single crystal. Source: the author. | 73 |
| Figure 28 – Schematic drawing of the experimental set-up used to measure the ultrasonic velocities on radial directions of the single crystal. The top probe position is illustrated by the dark line probe sketch, while the other two positions are represented by the dim probe sketches. Source: the author. | 74 |
| Figure 29 – Dissimilar weld block used for this chapter. Its dimensions are 83.5 mm x 35 mm x 40 mm. The five side-drilled holes aligned on one of the block’s side have a diameter equals to 3 mm and were bored all the way through the block. On another surface one can see an additional hole; however, this hole is shallow and does not influence this study. Source: the author. | 75 |
| Figure 30 – Schematic representation of the weld sample from which the block was extracted. The rectangle in the middle of the weld represents the position from where the block was extracted. Adapted from (4) and (5). Dimensions are in millimetres. Adapted form Dissimilar project report (4). | 76 |
| Figure 31 – EBSD map used to represent the crystallographic orientations of the block. Adapted form Dissimilar project report (4). | 77 |
| Figure 32 – Macrograph of the original weld cross-section which originated the testing block. Image courtesy of TWI. | 78 |
| Figure 33 – Photograph showing the set-up used to collect the experimental data from the block underwater in the immersion tank. Source: the author. | 79 |
| Figure 34 – Illustration of the 6 dB rule using a single element transducer. The squares on the top of the figure represent what the A-scan would look like for their respective probe positions. Source: the author. | 80 |

| | |
|---|----|
| Figure 35 – Illustration of the block position mapping. The grey rectangles on the top image represent the piezoelectric transducer in its several positions throughout the block. On the bottom right corner, there is an image of the block in perspective with the transducer positioned on one of the positioning points. On both of the images, the measurement planes, at which the FMC’s were collected, are also indicated. Source: the author. | 81 |
| Figure 36 – Weld block with the modelled region highlighted. The white rectangle on top is the water layer and the imaged region is represented by the rectangle in the centre of the EBSD map. Source: the author. | 82 |
| Figure 37 – Tone burst used to excite both the phased array and virtual transducers in the weld block simulations. Source: the author. | 83 |
| Figure 38 – Lined pipe cross-section schematic drawing. The numbers 1 to 4 indicate the most probable places to nucleate a fatigue crack. Source: the author. | 86 |
| Figure 39 – Geometry of the sample used in this chapter showing in the detail circle the 0.8 mm deep notch. Dimensions are in millimetres. Source: the author. | 87 |
| Figure 40 – Macrograph of the plate showing the 0.8 mm deep notch. The scale at the bottom of the image is in millimetres. Source: the author. | 88 |
| Figure 41 – Experimental configuration used to collect the FMC from the lined plates, dimension are in millimetres. Source: the author. | 89 |
| Figure 42 – Phase slowness surface for the longitudinal mode of the single crystal. Source: the author. | 95 |
| Figure 43 – Phase slowness surface for the fast transversal mode of the single crystal. Source: the author. | 95 |
| Figure 44 – Phase slowness surface for the slow transversal mode of the single crystal. Source: the author. | 96 |
| Figure 45 – Group slowness surface for the longitudinal mode of the single crystal. Source: the author. | 97 |
| Figure 46 – Group slowness surface for the fast transversal mode of the single crystal. Source: the author. | 97 |

| | |
|---|-----|
| Figure 47 – Group slowness surface for the slow transversal mode of the single crystal. Source: the author. | 98 |
| Figure 48 – Comparison between the phase and group slowness curves of the single crystal for the (001) plane. 0° is aligned with the [100] direction, while 90° is aligned with the [010] direction. Source: the author. | 98 |
| Figure 49 – Experimental conventional TFM results for the three inspected planes. Source: the author. | 100 |
| Figure 50 – Simulation results. (a) Simulated conventional TFM with side-drilled hole; (b) simulated conventional TFM without side-drilled hole; (c) the result of the subtraction of the image in (a) by the image in (b). Source: the author. | 101 |
| Figure 51 – ADTFM results for the three inspected planes. Source: the author. . . | 103 |
| Figure 52 – Conventional TFM image of the triple joint region showing the 0.8 mm deep notch using the 10 MHz probe, linear scale and arbitrary units. Source: the author. | 105 |
| Figure 53 – Conventional TFM image of the triple joint region showing the 0.8 mm deep notch using the 10 MHz probe; the red ellipse indicates the boundary between the cladding and the steel plate. The image is in the decibel scale. Source: the author. | 106 |
| Figure 54 – Conventional TFM image of the triple joint region, showing in detail the triple joint, tip of the notch and root of the notch indications. This figure is presented on the decibel scale. Source: the author. | 107 |
| Figure 55 – Conventional TFM images of the three regions of the lined plate analysed. Data collected with the 10 MHz probe. Source: the author. | 108 |
| Figure 56 – ICF images for several P_{CF} from the 0.8 mm deep notch using the 10 MHz probe. Source: the author. | 109 |
| Figure 57 – ICF images for several P_{CF} from the 1.6 mm deep notch using the 10 MHz probe. Source: the author. | 109 |
| Figure 58 – CF images for several P_{CF} from the region without any notch using the 10 MHz probe. Source: the author. | 110 |

| | |
|---|-----|
| Figure 59 – IPCF images for several P_{PCF} from the 0.8 mm deep notch using the 10 MHz probe. Source: the author. | 111 |
| Figure 60 – ISCF images for several P_{SCF} from the 0.8 mm deep notch using the 10 MHz probe. Source: the author. | 111 |
| Figure 61 – Conventional TFM images of the three regions of the lined plate analysed. Data collected with the 15 MHz probe. Source: the author. | 113 |
| Figure 62 – ISCF images for several P_{SCF} from the 0.8 mm deep notch using the 15 MHz probe. Source: the author. | 114 |
| Figure 63 – ISCF images for several P_{SCF} from the 1.6 mm deep notch using the 15 MHz probe. Source: the author. | 114 |
| Figure 64 – ISCF images for several P_{SCF} from the unnotched region using the 15 MHz probe. Source: the author. | 115 |
| Figure 65 – ICF applied to the ADTFM image of the dissimilar weld block for four sensibility factor amplitudes. This image was obtained from the ADTFM image presented in Figure 51 (a). Source: the author. | 116 |
| Figure 66 – IPCF applied to the ADTFM image of the dissimilar weld block for four sensibility factor amplitudes. This image was obtained from the ADTFM image presented in Figure 51 (a). Source: the author. | 117 |
| Figure 67 – ISCF applied to the ADTFM image of the dissimilar weld block for four sensibility factor amplitudes. This image was obtained from the ADTFM image presented in Figure 51 (a). Source: the author. | 118 |
| Figure 68 – IPCF images for several P_{PCF} from the 1.6 mm deep notch using the 10 MHz probe. Source: the author. | 136 |
| Figure 69 – IPCF images for several P_{PCF} from the region without any notch using the 10 MHz probe. Source: the author. | 137 |
| Figure 70 – ISCF images for several P_{SCF} from the 1.6 mm deep notch using the 10 MHz probe. Source: the author. | 137 |
| Figure 71 – ISCF images for several P_{SCF} from the region without any notch using the 10 MHz probe. Source: the author. | 138 |

| | |
|---|-----|
| Figure 72 – ICF applied to the ADTFM image of the dissimilar weld block for four sensibility factor amplitudes. This image was obtained from the ADTFM image presented in Figure 51 (b). Source: the author. | 139 |
| Figure 73 – IPCF applied to the ADTFM image of the dissimilar weld block for four sensibility factor amplitudes. This image was obtained from the ADTFM image presented in Figure 51 (b). Source: the author. | 140 |
| Figure 74 – ISCF applied to the ADTFM image of the dissimilar weld block for four sensibility factor amplitudes. This image was obtained from the ADTFM image presented in Figure 51 (b). Source: the author. | 141 |
| Figure 75 – ICF applied to the ADTFM image of the dissimilar weld block for four sensibility factor amplitudes. This image was obtained from the ADTFM image presented in Figure 51 (c). Source: the author. | 142 |
| Figure 76 – IPCF applied to the ADTFM image of the dissimilar weld block for four sensibility factor amplitudes. This image was obtained from the ADTFM image presented in Figure 51 (c). Source: the author. | 143 |
| Figure 77 – ISCF applied to the ADTFM image of the dissimilar weld block for four sensibility factor amplitudes. This image was obtained from the ADTFM image presented in Figure 51 (c). Source: the author. | 144 |

List of Tables

| | |
|--|----|
| Table 1 – Color key for the grain orientations presented in Figure 31 | 77 |
| Table 2 – Average velocity measured using the shear wave contact probe. | 91 |
| Table 3 – Average velocity measured using the longitudinal wave contact probe. | 91 |
| Table 4 – Immersion measurements results for $V_{L\langle 100 \rangle}$ | 91 |
| Table 5 – Immersion measurements results for $V_{L\langle 110 \rangle}$ | 91 |
| Table 6 – Experimental velocities | 93 |
| Table 7 – Stiffness constants from contact velocities measurements | 93 |
| Table 8 – Stiffness constants C_{11} and C_{12} | 94 |

List of abbreviations and acronyms

| | |
|-------|---|
| ADL | Adapted delay law |
| ADTFM | Adaptive total focusing method |
| CF | Coherence factor |
| EBSA | Electron backscatter diffraction |
| EDM | Electrical discharge machining |
| FEA | Finite element analysis |
| FMC | Full matrix capture |
| GTAW | Gas tungsten arc welding |
| MINA | Modelling anisotropy from notebook of arc welding |
| PCF | Phase coherence factor |
| SAFT | Synthetic Aperture Focusing Technique |
| SCF | Signal coherence factor |
| SMAW | Shielded metal arc welding |
| SNR | Signal to noise ratio |
| TFM | Total focusing method |
| TOF | Time of flight |

List of symbols

| | |
|---------------------------------|---|
| $\alpha_1, \alpha_2, \alpha_3,$ | Polynomial equation coefficients |
| α_4 | |
| α, β, γ | Rotation angles |
| Γ | Christoffel matrix |
| δ | Kronecker delta |
| ϵ | Strain |
| θ_1, θ_2 | Incidence and refraction angle |
| ρ | Density |
| σ | Standard deviation |
| σ_m | Standard deviation of the mean |
| σ_p | Minimum standard deviation for a phase distribution |
| σ_0 | Standard deviation of a random phase distribution between $-\pi$ and π , equals to $\pi/\sqrt{3}$ |
| τ | Stress |
| χ | Generic measurement |
| $\bar{\chi}$ | mean of χ |
| ω | Angular frequency |
| A | A-scan |
| \mathbf{B} | Generic vector |
| C | Stiffness matrix |

| | |
|------------------|---|
| c, c_1, c_2 | Wave velocity, Wave velocity in medium 1, Wave velocity in medium 2 |
| CF | Coherence factor |
| CI | Coherence Intensity |
| C_{ij} | Stiffness matrix element |
| $f_1, f_2, f_3,$ | |
| $f_4, f_5, f_6,$ | Ferrari's fourth order polynomial solution method parameters |
| $f_7, f_8, f_9,$ | |
| f_{10} | |
| I_{TFM} | TFM pixel intensity |
| ICF | TFM pixel intensity after multiplication by CF |
| $IPCF$ | TFM pixel intensity after multiplication by PCF |
| $ISCF$ | TFM pixel intensity after multiplication by SCF |
| \mathbf{K} | Response matrix (DORT) |
| k | Wave number |
| \mathbf{m} | Phase slowness vector |
| \mathbf{m}_g | Group slowness vector |
| N | Number of elements in the array |
| n | Direction cosine |
| \mathbf{n} | Phase unit vector |
| \mathbf{n}_g | Group unit vector |
| PCF | Phase coherence factor |

| | |
|------------------------|--|
| P_{CF} | Coherence factor sensitivity |
| P_{PCF} | Phase coherence factor sensitivity |
| P_{SCF} | Signal coherence factor sensitivity |
| R | Combined coordinate transformation matrix |
| \mathbf{r} | Coordinate transformation matrix around an axis |
| s | Phase sign of an A-scan at a specific time of flight |
| SCF | Signal coherence factor |
| t_s | Student's t factor |
| $t_{x,y,m}$ | Time of flight for focusing point (x, y) and transducer m |
| \mathbf{V} | Phase velocity vector |
| \mathbf{V}_g | Group velocity vector |
| \mathbf{v}_m | Velocity vector |
| X | Generic quantity |
| X_{xym}^a, Y_{xym}^a | Coordinates of the intersection point for a focusing point at (x,y) and the transducer m |
| x, y | Focusing point coordinates |
| X_m^0, Y_m^0 | Coordinates of the centre of a transducer m |

Contents

| | | |
|------------|--|-----------|
| 1 | INTRODUCTION | 22 |
| 2 | OBJECTIVES | 24 |
| 2.1 | General objective | 24 |
| 2.2 | Specific objectives | 24 |
| 3 | BACKGROUND STUDY | 25 |
| 3.1 | Anisotropy and inhomogeneity | 25 |
| 3.2 | Elastic wave propagation in anisotropic media | 28 |
| 3.2.1 | Christoffel Equation | 28 |
| 3.2.2 | Slowness curves and surfaces | 31 |
| 3.2.3 | Phase and group velocities | 37 |
| 3.3 | Full matrix capture and total focusing method | 44 |
| 3.4 | Ultrasonic inspection in anisotropic and inhomogeneous materials | 50 |
| 3.4.1 | Decomposition of the time reversal operator and multiple scattering filter | 50 |
| 3.4.2 | Grain orientation assessment | 51 |
| 3.4.3 | Ultrasonic wave propagation problem | 52 |
| 3.4.4 | Adaptive ultrasonic imaging | 53 |
| 3.4.5 | Coherence weights | 54 |
| 3.5 | Summary | 59 |
| 4 | METHODOLOGY | 60 |
| 4.1 | Adaptive delay total focusing method | 60 |
| 4.1.1 | Adaptive delay total focusing method description | 61 |
| 4.1.2 | Single crystal | 63 |
| 4.1.2.1 | Single crystal specimen description and experimental set-up | 65 |
| 4.1.2.2 | Acoustic wave propagation simulation | 66 |
| 4.1.2.3 | Mechanical properties computation procedure | 71 |

| | | |
|------------|---|------------|
| 4.1.3 | Description of the test sample | 74 |
| 4.1.4 | Experimental methodology | 78 |
| 4.1.5 | Simulation methodology | 81 |
| 4.2 | Coherence weights | 84 |
| 4.2.1 | Mechanically lined pipes | 84 |
| 4.2.2 | Lined plates description and experimental set-up | 85 |
| 4.3 | Summary | 89 |
| 5 | RESULTS AND DISCUSSION | 90 |
| 5.1 | Adaptive delay total focusing method | 90 |
| 5.1.1 | Single crystal experiment results | 90 |
| 5.1.2 | ADTFM results | 99 |
| 5.2 | Coherence weights | 104 |
| 5.2.1 | Coherence weights applied on lined plate's images | 104 |
| 5.2.2 | Coherence weights applied on dissimilar weld block images | 115 |
| 6 | CONCLUSION | 119 |
| | BIBLIOGRAPHY | 121 |
| | APPENDIX | 127 |
| | APPENDIX A – EBSD INTRODUCTION AND METHODOLOGY | 128 |
| A.1 | Introduction to EBSD | 128 |
| A.2 | EBSD methodology | 129 |
| | APPENDIX B – CONFIDENCE INTERVAL AND UNCERTAINTY PROP- AGATION | 131 |
| B.1 | Best estimate for the population mean and standard deviation | 131 |
| B.2 | Confidence interval using Student's t distribution | 132 |

| | | |
|------------|--|------------|
| B.3 | Error propagation | 133 |
| | APPENDIX C – COMPLEMENTARY IMAGES | 136 |

1 INTRODUCTION

Austenitic materials are often used in the construction and cladding of critical components and structures for the oil&gas and nuclear industries due to their characteristics, such as their corrosion resistance, strength, toughness and unnecessary heat treatment after welding (3). As a result of the high potential risk involved in the manipulating petrochemicals and radioactive materials, the non-destructive assessment of critical austenitic parts, especially the welded ones, is a significant concern for those industrial sectors. Among the ultrasonic inspection techniques which demonstrated viability on the inspection of austenitic materials is the phased array ultrasonics. However, the intrinsic anisotropy and inhomogeneity of austenitic materials make their inspection via ultrasonic methods challenging (4–6).

The usage of phased array ultrasonics to assess austenitic materials has been studied in several works (4, 7–15). Despite all the effort put into the problem of ultrasonic inspection of austenitic materials, this issue has not been entirely solved yet. Therefore, the development of non-destructive imaging techniques and applications capable of identifying, locate and measure defects is welcome by the industry as a way to assure the safe operation of those components and making its usage more cost effective by increasing their lifetime. This thesis will use the Total Focusing Method (TFM) analysis technique as a starting point for two methods capable of addressing the issues caused by the anisotropy and inhomogeneity in austenitic materials.

The first is a novel approach intended to minimise the anisotropy and inhomogeneity problems by applying the concept of adaptive delay laws (ADL) into the TFM imaging method. This method is named Adaptive Delay Total Focusing Method (ADTFM). The ADTFM was developed as a way to correct the position of indications in austenitic welds. The sample used to demonstrate the ADTFM is a dissimilar austenitic weld block with side-drilled holes. This sample was initially developed as part of the DISSIMILAR project (4). During the DISSIMILAR project, the Electron backscatter diffraction (EBSD) data,

used in this thesis as a description of the block's grain orientation, was assessed. In order to obtain the stiffness matrix of the material, which is a requirement of the ADTFM, a single crystal specimen of the same alloy as the dissimilar weld block was used. The single crystal specimen was also created during the DISSIMILAR project (4). However, its mechanical stiffness matrix was obtained as part of the investigations undertaken for this thesis via acoustic measurements using single element probes. The second approach uses three different coherence weights to reduce the signal to noise ratio and the presence of false indications in TFM images both from the dissimilar weld block and from a plate, which mimics the triple joint region of mechanical lined pipes. Both methods were combined and used in the inspection of the dissimilar weld block with the intention of blending the advantages of the coherence weights and ADTFM, producing images with high signal to noise ratio, reduced presence and amplitude of false indications and with the true indications correctly positioned.

2 OBJECTIVES

2.1 General objective

To identify the location of reflectors and reduce the amplitude and presence of false indications of phased array results from austenitic welds and claddings by the study and evaluation of non-conventional imaging methods based on FMC/TFM (Full Matrix Capture / Total Focusing Method).

2.2 Specific objectives

- To develop a new imaging method, based on Adaptive Delay Laws (ADL) and FMC/TFM, capable of correcting the position of a side-drilled hole indication from an austenitic weld sample.
- To apply the Coherence Weights methods in lined pipe's triple joint mock-up specimens FMC data and in austenitic weld sample data in order to reduce the amplitude of false indications and noise.

3 BACKGROUND STUDY

This chapter begins with an introduction about mechanical anisotropy and inhomogeneity in the first section, followed by an introduction to the Christoffel Equation and slowness surface in Section 3.2. Subsequently, in Section 3.3, the Full Matrix Capture and Total Focusing Method data acquisition and imaging procedure are introduced. Subsequently, Section 3.4 expounds a review of the ultrasonic inspections methods used in anisotropic and inhomogeneous materials.

3.1 Anisotropy and inhomogeneity

It is common for some materials to have their atoms arranged in a periodic long-range way. It is said that such materials are crystalline and the arrangement pattern is called crystal structure. This pattern can be represented by its unit cell (16). Crystal structures can be grouped into seven crystal systems according to the geometry of the unit cell, namely cubic, tetragonal, orthorhombic, monoclinic, rhombohedral, triclinic and hexagonal (8,16). Figure 1 presents a unit cell for a body centred cubic (bcc) crystal. The anisotropy of a crystal is dictated by the symmetry of the group system it belongs to. Triclinic materials have no symmetry and are fully anisotropic. Therefore their elastic behaviour requires 21 independent stiffness constants to be described, while the cubic materials are the most symmetric ones and require only three independent stiffness constants to describe their elastic behaviour (8).

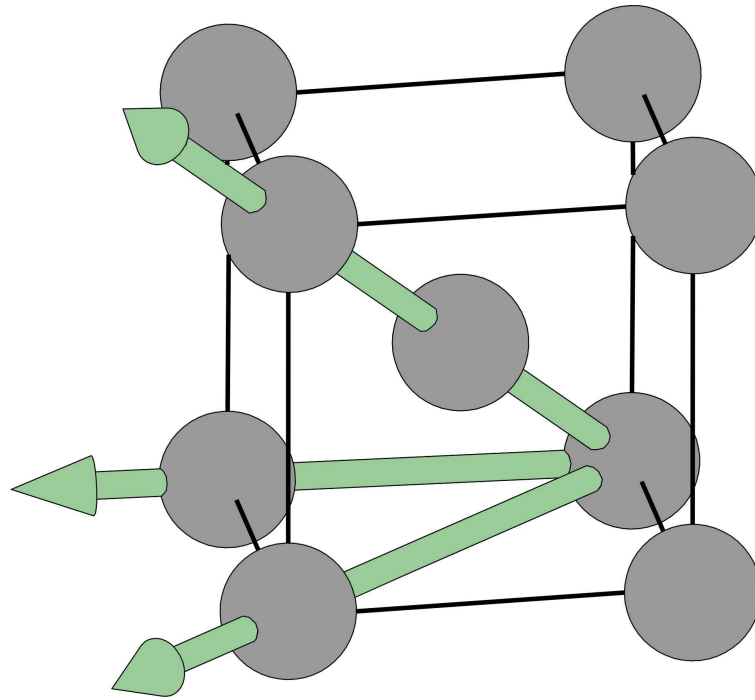


Figure 1 – Unit cell for bcc crystals. The crystallographic directions $[100]$, $[110]$ and $[111]$ are indicated. Source: the author.

Connolly (3) explains that the mechanical anisotropy comes from the directional dependence of the inter-atomic forces, which leads to distinct elastic properties in different directions. Auld (1) exemplifies this concept by saying that a compression along the $[110]$ direction in a cubic crystal is subjected to a different stiffness than a compression in the $[010]$ direction. Due to this and the dependence of the sound wave velocities on the material's mechanical properties, there is a dependence of such velocities on the propagation angle.

In a polycrystalline material, the boundary between adjacent crystallites or grains can work as an interface for a sound beam travelling through it. This boundary can make the beam change its propagation direction due to reflection, refraction and mode conversion taking place in the grain boundary. The reason for this to happen lies in the acoustic impedance mismatch in the interface between adjacent grains, which is caused by the grains' anisotropy and the variation of the crystallographic orientation between the grains (8).

When the grain size is small compared to the wavelength of the acoustic wave and the grains are randomly orientated the material can be considered isotropic and homogeneous (3,8,9). However, when the grain size is close to the wavelength of the sound wave employed, the inhomogeneity and anisotropy characteristics of the material become more important. Usually, when the grains are as big as one-tenth of the wavelength (17), significant scattering loss starts to take place.

In short, the influence of microstructure on the scattering loss can be classified into three models (4,8). The geometric regime describes a polycrystalline as a thick-layered medium where the wavelength is much smaller than the grain size. Where an increase in the grain size reduces the number of interfaces inside the material, reducing the attenuation; however, the dependence of the frequency on the attenuation can be neglected (8,18). The second is the Rayleigh regime, in this regime, the grains are much smaller than the wavelength. In the Rayleigh regime the attenuation increases with the grain size and frequency. The last one is called stochastic regime and dominates when the grain size is around the same order of magnitude as the wavelength. The attenuation in the stochastic regime, similarly as in the Rayleigh regime, increases with the grain size and frequency, but less intensely (8).

In practice, the grain size of austenitic welds and overlay claddings are in the stochastic regime when inspected by conventional or phased array ultrasonic probes. With this in mind, it follows that anisotropy and inhomogeneity have three main adverse effects on ultrasonic inspection on such cases (4):

- Increased backscattered energy;
- Increased attenuation;
- Increased distortion.

The increased backscattered energy rises when a sound beam reaches a grain boundary, and the energy is partially reflected towards the transducer, which increases the background noise level (4,19,20). Also, since some of the energy is reflected, less energy is available

to propagate further into the material, increasing the attenuation (4, 20). Some of the attenuation is caused by the absorption of the wave energy by the material, but its contribution is smaller (4). Considering that the grain boundary behaves as an acoustic interface when a sound beam reaches a grain boundary, it can shift its propagation direction and mode conversion can occur. This sort of interference in the beam is usually referred to as beam skewing and further detail can be found in the book from the German Society for Non-Destructive Testing (21).

3.2 Elastic wave propagation in anisotropic media

This section is divided into three subsections, and it aims to present mathematical tools to describe and represent the behaviour of acoustic waves in anisotropic media. The first part deals with the Christoffel equation, which is used to describe uniform plane waves and was demonstrated to be useful when modelling acoustic plane waves propagating in anisotropic materials. In the second subsection, there is an introduction to the representation of the solutions of the Christoffel equation via slowness curves and surfaces. Lastly, the third subsection is about the concept of group velocity and the group velocity slowness curves.

3.2.1 Christoffel Equation

The velocity of an ultrasonic beam is affected by the material's mechanical properties, namely density and stiffness (4). Through the wave equation, it is possible to evaluate how a variation in the mechanical properties will affect the ultrasonic beam. The wave equation for uniform plane waves can be reduced to the Christoffel Equation (Equation 3.1) which applies both to the isotropic and anisotropic media (1, 22). In the Christoffel Equation,

$$\left(k^2\Gamma_{im} - \rho\omega^2\delta_{im}\right)v_m = 0, \quad (3.1)$$

k is the wave number, ρ is the material's density, ω is the angular frequency, δ_{im} is the Kronecker delta and, v_m is the velocity vector. The matrix Γ_{im} is the Christoffel matrix, defined in Equation 3.2, whose elements are functions of the plane wave propagation direction and the stiffness constants of the medium (1).

$$\Gamma_{im} = C_{ijkm}n_jn_m \quad (3.2)$$

In Equation 3.2, C_{ijkm} is the material's stiffness matrix, and n_j and n_m are direction cosines of the normal to the wavefront. The most general representation of Γ is for the triclinic crystal system. The expanded Christoffel matrix for this case is presented in Equation 3.3.

$$\Gamma = \begin{bmatrix} \Gamma_{11} & \Gamma_{12} & \Gamma_{13} \\ \Gamma_{21} & \Gamma_{22} & \Gamma_{23} \\ \Gamma_{31} & \Gamma_{32} & \Gamma_{33} \end{bmatrix} \quad (3.3)$$

where

$$\Gamma_{11} = C_{11}n_x^2 + C_{66}n_y^2 + C_{55}n_z^2 + 2C_{56}n_yn_z + 2C_{15}n_zn_x + 2C_{16}n_xn_y$$

$$\Gamma_{22} = C_{66}n_x^2 + C_{22}n_y^2 + C_{44}n_z^2 + 2C_{24}n_yn_z + 2C_{46}n_zn_x + 2C_{26}n_xn_y$$

$$\Gamma_{33} = C_{55}n_x^2 + C_{44}n_y^2 + C_{33}n_z^2 + 2C_{34}n_yn_z + 2C_{35}n_zn_x + 2C_{45}n_xn_y$$

$$\Gamma_{12} = \Gamma_{21} = C_{16}n_x^2 + C_{26}n_y^2 + C_{45}n_z^2 + (C_{46} + C_{25})n_yn_z + (C_{14} + C_{56})n_zn_x + (C_{12} + C_{66})n_xn_y$$

$$\Gamma_{13} = \Gamma_{31} = C_{15}n_x^2 + C_{46}n_y^2 + C_{35}n_z^2 + (C_{45} + C_{36})n_yn_z + (C_{13} + C_{55})n_zn_x + (C_{14} + C_{56})n_xn_y$$

$$\Gamma_{23} = \Gamma_{32} = C_{56}n_x^2 + C_{24}n_y^2 + C_{34}n_z^2 + (C_{44} + C_{23})n_yn_z + (C_{36} + C_{45})n_zn_x + (C_{25} + C_{46})n_xn_y$$

In Equation 3.3, n_x , n_y and n_z are the direction cosines in the respective direction and C_{ij} are the stiffness matrix components written using Voigt notation. Rose (22) explains that for a non-trivial solution of Equation 3.1 it is required that:

$$\left| \frac{k^2}{\omega^2} \Gamma_{im} - \rho \delta_{im} \right| = 0 \quad (3.4)$$

Replacing Γ_{im} in Equation 3.4 by Equation 3.2 one can solve the determinant for the slowness, k/ω , as a function of the propagation direction defined by the direction cosines. For cubic materials, such as those used in this work, the expanded form of Equation 3.4 is presented in Equation 3.5.

$$\begin{vmatrix} \left(\frac{k}{\omega}\right)^2 [C_{11}n_x^2 + C_{44}(1-n_x^2)] - \rho & \left(\frac{k}{\omega}\right)^2 [C_{12} + C_{44}]n_xn_y & \left(\frac{k}{\omega}\right)^2 [C_{12} + C_{44}]n_xn_z \\ \left(\frac{k}{\omega}\right)^2 [C_{12} + C_{44}]n_xn_y & \left(\frac{k}{\omega}\right)^2 [C_{11}n_y^2 + C_{44}(1-n_y^2)] - \rho & \left(\frac{k}{\omega}\right)^2 [C_{12} + C_{44}]n_yn_z \\ \left(\frac{k}{\omega}\right)^2 [C_{12} + C_{44}]n_xn_z & \left(\frac{k}{\omega}\right)^2 [C_{12} + C_{44}]n_yn_z & \left(\frac{k}{\omega}\right)^2 [C_{11}n_z^2 + C_{44}(1-n_z^2)] - \rho \end{vmatrix} = 0 \quad (3.5)$$

When solving Equation 3.4 one will find up to three real values for k/ω for every propagation direction. Those values represent the three different modes present in the material: a longitudinal vibration mode and two transversal modes. The transversal ones vibrate in an orthogonal direction between each other. Since the phase slowness is the inverse of the phase velocity, it is straightforward to visualise how the phase velocity varies with the propagation direction in a material. The solution of Equation 3.4 usually requires the use of numerical computation (1); however, in some cases, it is possible to use an analytic approach. For example, for a cubic crystal it is possible to obtain the Equations 3.6, 3.7, 3.8, 3.9, 3.10 and 3.11 for some of the key orientations:

$$V_{S1\{100\}} = V_{S2\langle 100 \rangle} = \sqrt{\frac{C_{44}}{\rho}} \quad (3.6)$$

$$V_{L\langle 100 \rangle} = \sqrt{\frac{C_{11}}{\rho}} \quad (3.7)$$

$$V_{S2\langle 110 \rangle} = \sqrt{\frac{C_{11} - C_{12}}{2\rho}} \quad (3.8)$$

$$V_{L\langle 110 \rangle} = \sqrt{\frac{C_{11} + C_{12} + 2C_{44}}{2\rho}} \quad (3.9)$$

$$V_{S1\langle 111 \rangle} = V_{S2\langle 111 \rangle} = \sqrt{\frac{C_{11} - C_{12} + C_{44}}{3\rho}} \quad (3.10)$$

$$V_{L\langle 111 \rangle} = \sqrt{\frac{C_{11} + 2C_{12} + 4C_{44}}{3\rho}} \quad (3.11)$$

In the equations above, V_{S1} is the shear wave mode with out-of-the-plane vibration phase velocity, V_{S2} is the shear wave mode with in-plane vibration phase velocity and, V_{L1} is the longitudinal vibration mode phase velocity. The indexes subscribed next to the phase velocities indicate the family of crystallographic directions or family of crystallographic planes where the equations are valid. Auld (1) also introduces the anisotropy factor for the cubic crystal, A , which is defined by the ratio of the squares of the shear wave phase velocities $V_{S2\langle 100 \rangle}$ and $V_{S2\langle 110 \rangle}$, resulting in Equation 3.12.

$$A = \frac{2C_{44}}{C_{11} - 2C_{12}} \quad (3.12)$$

3.2.2 Slowness curves and surfaces

Slowness surfaces or curves can be used as a better representation of the results provided by the solution of Equation 3.4. Those curves are obtained when one considers the wave propagating in a specific plane of the material. As an illustration, one can find in Figure 2 the slowness curves for the plane (001) of GaAs, whose elastic constants are $C_{11} = 118.8$ GPa, $C_{12} = 53.8$ GPa and $C_{44} = 59.4$ GPa. These values were taken from Auld (1), where some of the slowness curves for this material are also presented.

In order to obtain slowness curves for different planes other than the (001), it is required to transform the stiffness matrix \mathbf{C} to the appropriate orientation. To build the background needed to describe the transformation of the matrix \mathbf{C} , the coordinate transform for vectors will be introduced first. Bond (23) said that in order to transform the orientation axis of a vector or rotate the vector, one needs to multiply it by an appropriate matrix. This operation is shown for an arbitrary vector \mathbf{B}_i in Equation 3.13.

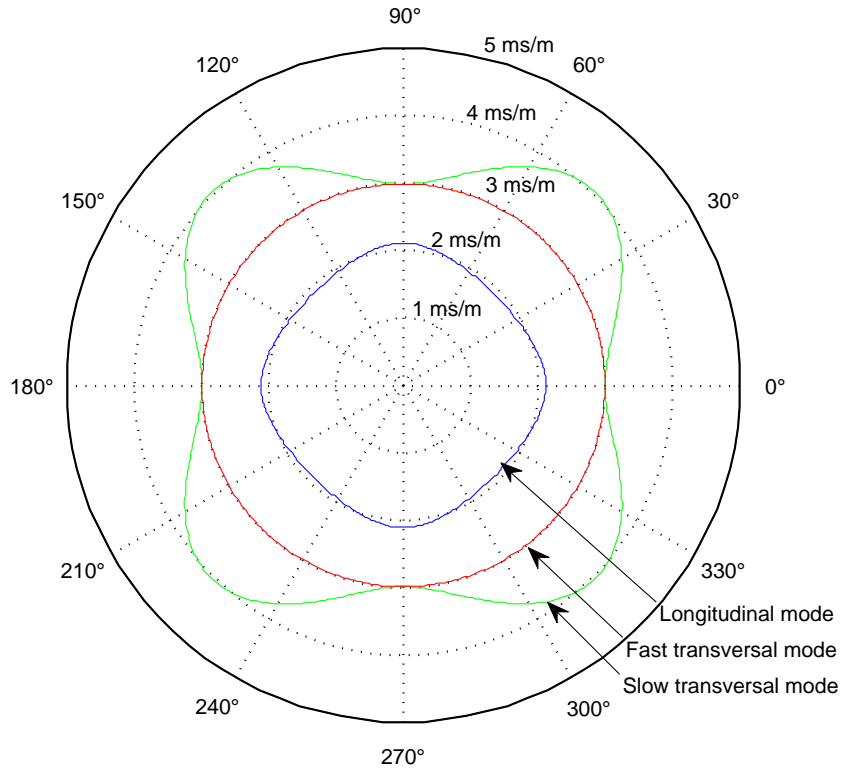


Figure 2 – Slowness curves for the plane (001) of a cubic crystal of GaAs. The three curves represent the three modes present. 0° is aligned with the $[100]$ direction, while 90° is aligned with the $[010]$ direction. Adapted from Auld (1).

$$\mathbf{B}'_i = \mathbf{r}_{ij} \mathbf{B}_j \quad (3.13)$$

To rotate \mathbf{B}_j around x axis by an α angle, the rotation matrix, now termed \mathbf{r}^x , assumes the form presented in Equation 3.14.

$$\mathbf{r}^x = \begin{bmatrix} 1 & 0 & 0 \\ 0 & \cos\alpha & \sin\alpha \\ 0 & -\sin\alpha & \cos\alpha \end{bmatrix} \quad (3.14)$$

Similarly, the respective rotation matrices for rotations around the y axis by an angle β and around z axis by an angle γ are presented in Equations 3.15 and 3.16.

$$\mathbf{r}^y = \begin{bmatrix} \cos\beta & 0 & -\sin\beta \\ 0 & 1 & 0 \\ \sin\beta & 0 & \cos\beta \end{bmatrix} \quad (3.15)$$

$$\mathbf{r}^z = \begin{bmatrix} \cos\gamma & \sin\gamma & 0 \\ -\sin\gamma & \cos\gamma & 0 \\ 0 & 0 & 1 \end{bmatrix} \quad (3.16)$$

Where β and γ are the rotation angles around y and z , respectively.

For a rotation around the three dimensions of space, one can rotate \mathbf{B}_j by Equations 3.14, 3.15 and 3.16 successively (1) as follows in Equations 3.17.

$$\begin{aligned} \mathbf{B}'_i &= \mathbf{r}^x_{ij} \mathbf{B}_j \\ \mathbf{B}''_i &= \mathbf{r}^y_{ij} \mathbf{B}'_j \\ \mathbf{B}'''_i &= \mathbf{r}^z_{ij} \mathbf{B}''_j \end{aligned} \quad (3.17)$$

The equations above can be combined into a single equation, presented as Equation 3.18 below.

$$\mathbf{B}'''_i = \mathbf{R}_{ij} \mathbf{B}_j \quad (3.18)$$

Where:

$$\mathbf{R}_{ij} = \mathbf{r}^x_{ik} \mathbf{r}^y_{kl} \mathbf{r}^z_{lj}. \quad (3.19)$$

There are several ways to combine \mathbf{r}^x , \mathbf{r}^y and \mathbf{r}^z (23). Among the options, the extrinsic transformation sequence defined by Equation 3.19 was chosen in the present work.

The same principle used to transform the axis of a vector applies for tensors. To introduce the coordinate transformation of \mathbf{c} , it is convenient to first present the Hooke's law in full subscript notation (Equation 3.20).

$$\tau_{ij} = \mathbf{C}_{ijkl} \epsilon_{kl} \quad (3.20)$$

In Equation 3.20, τ_{ij} is the stress tensor ¹ and ϵ_{kl} is the strain tensor. According to Auld (1), to transform both the stress and strain, one can multiply those matrices by the transformation matrix \mathbf{R} as follows in Equations 3.21 and 3.22, where τ'_{ij} is the transformed stress matrix and ϵ'_{kl} is the transformed strain matrix.

$$\tau'_{ij} = \mathbf{R}_{ik} \mathbf{R}_{jl} \tau_{kl} \quad (3.21)$$

$$\epsilon'_{ij} = \mathbf{R}_{ik} \mathbf{R}_{jl} \epsilon_{kl} \quad (3.22)$$

Bond (23) developed a matrix technique capable to benefit from the simplicity of the Voigt notation, contrasting with the full subscripts notation (1). To use Bond's technique, first Equation 3.19 is expanded and presented in Equation 3.23

$$\mathbf{R}_{ij} = \begin{bmatrix} \cos(\beta)\cos(\gamma) & \cos(\beta)\sin(\gamma) & -\sin(\beta) \\ \cos(\gamma)\sin(\alpha)\sin(\beta) - \cos(\alpha)\sin(\gamma) & \sin(\alpha)\sin(\beta)\sin(\gamma) + \cos(\alpha)\cos(\gamma) & \cos(\beta)\sin(\alpha) \\ \cos(\alpha)\cos(\gamma)\sin(\beta) + \sin(\alpha)\sin(\gamma) & \cos(\alpha)\sin(\beta)\sin(\gamma) - \cos(\gamma)\sin(\alpha) & \cos(\alpha)\cos(\beta) \end{bmatrix} \quad (3.23)$$

From the elements of \mathbf{R} two matrices are built and are shown in Equations 3.24 and 3.25.

¹In this text the stress is represented by the greek letter tau in order to avoid confusion with the letter sigma, which is used elsewhere in this work to represent the standard deviation.

$$\mathbf{R}^\tau = \begin{bmatrix} R_{11}^2 & R_{12}^2 & R_{13}^2 & 2R_{12}R_{13} & 2R_{13}R_{11} & 2R_{11}R_{12} \\ R_{21}^2 & R_{22}^2 & R_{23}^2 & 2R_{22}R_{23} & 2R_{23}R_{21} & 2R_{21}R_{22} \\ R_{31}^2 & R_{32}^2 & R_{33}^2 & 2R_{32}R_{33} & 2R_{33}R_{31} & 2R_{31}R_{32} \\ R_{21}R_{31} & R_{22}R_{32} & R_{23}R_{33} & R_{22}R_{33} + R_{23}R_{32} & R_{21}R_{33} + R_{23}R_{31} & R_{22}R_{31} + R_{21}R_{32} \\ R_{31}R_{11} & R_{32}R_{12} & R_{33}R_{13} & R_{12}R_{33} + R_{13}R_{32} & R_{13}R_{31} + R_{11}R_{33} & R_{11}R_{32} + R_{12}R_{31} \\ R_{11}R_{21} & R_{12}R_{22} & R_{13}R_{23} & R_{12}R_{23} + R_{13}R_{22} & R_{13}R_{21} + R_{11}R_{23} & R_{11}R_{22} + R_{12}R_{21} \end{bmatrix} \quad (3.24)$$

$$\mathbf{R}^\epsilon = \begin{bmatrix} R_{11}^2 & R_{12}^2 & R_{13}^2 & R_{12}R_{13} & R_{13}R_{11} & R_{11}R_{12} \\ R_{21}^2 & R_{22}^2 & R_{23}^2 & R_{22}R_{23} & R_{23}R_{21} & R_{21}R_{22} \\ R_{31}^2 & R_{32}^2 & R_{33}^2 & R_{32}R_{33} & R_{33}R_{31} & R_{31}R_{32} \\ 2R_{21}R_{31} & 2R_{22}R_{32} & 2R_{23}R_{33} & R_{22}R_{33} + R_{23}R_{32} & R_{21}R_{33} + R_{23}R_{31} & R_{22}R_{31} + R_{21}R_{32} \\ 2R_{31}R_{11} & 2R_{32}R_{12} & 2R_{33}R_{13} & R_{12}R_{33} + R_{13}R_{32} & R_{13}R_{31} + R_{11}R_{33} & R_{11}R_{32} + R_{12}R_{31} \\ 2R_{11}R_{21} & 2R_{12}R_{22} & 2R_{13}R_{23} & R_{12}R_{23} + R_{13}R_{22} & R_{13}R_{21} + R_{11}R_{23} & R_{11}R_{22} + R_{12}R_{21} \end{bmatrix} \quad (3.25)$$

The variables \mathbf{R}^τ and \mathbf{R}^ϵ can be used to rewrite Equations 3.21 and 3.22 in Voigt notation (1, 23), as follows in Equations 3.26 and 3.27.

$$\boldsymbol{\tau}'_i = \mathbf{R}_{ij}^\tau \boldsymbol{\tau}_j \quad (3.26)$$

$$\boldsymbol{\epsilon}'_i = \mathbf{R}_{ij}^\epsilon \boldsymbol{\epsilon}_j \quad (3.27)$$

Rearranging Equations 3.26 and 3.27 and inserting the Voigt notation version of Equation 3.20, $\boldsymbol{\tau}_i = \mathbf{c}_{ij} \boldsymbol{\epsilon}_j$, the Equation 3.28 is obtained.

$$\boldsymbol{\tau}' = \mathbf{R}^\tau \mathbf{C} \mathbf{R}^{\epsilon^{-1}} \boldsymbol{\epsilon}' \quad (3.28)$$

Equation 3.28 indicates that the transformation of \mathbf{C} into \mathbf{C}' can be performed via Equation 3.29.

$$\mathbf{C}' = \mathbf{R}^T \mathbf{C} \mathbf{R}^{\epsilon^{-1}} \quad (3.29)$$

By applying Equation 3.29 to transform the coordinates of \mathbf{C} by the set of angles α , β and γ before the solution of Equation 3.4, it is possible to plot the slowness curves for the new orientation. Using, again, the stiffness matrix of GaAs as an example it follows the resulting slowness curves for the planes (011) in Figure 3 and (111) in Figure 4.

By varying β or γ in small steps, it is possible to construct the slowness curve, which contains the slowness values for all crystallographic orientations of a given crystal. Examples of the slowness curves for the three acoustic modes of a GaAs crystal are presented in Figures 5, 6 and 7 below.

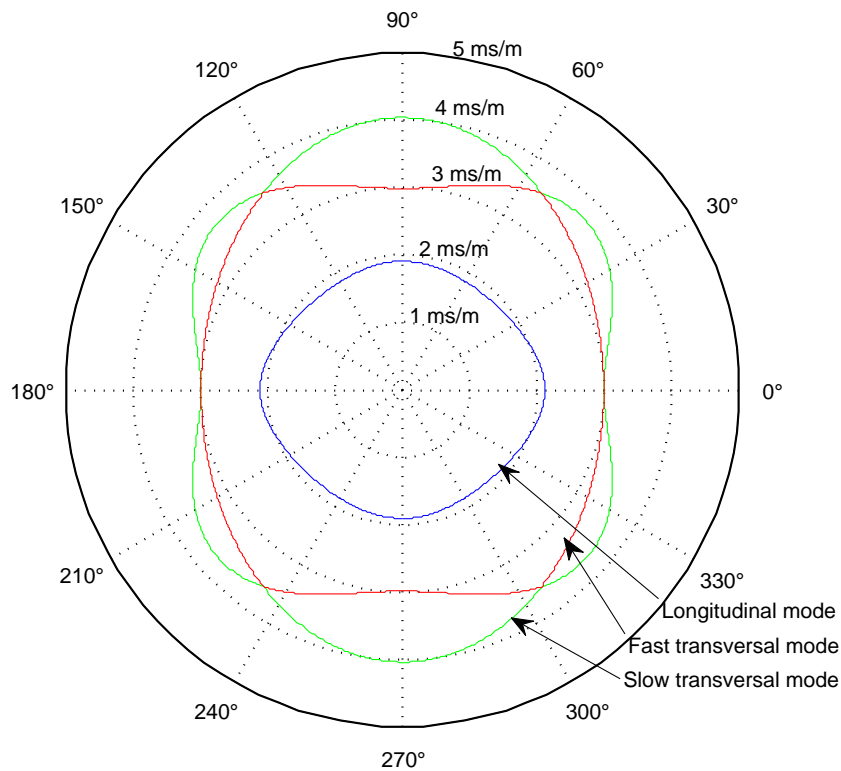


Figure 3 – Slowness curves for the plane (011) of a cubic crystal of GaAs. The three curves represent the three modes present. 0° is aligned with the $[100]$ direction, while 90° is aligned with the $[011]$ direction. Adapted from Auld (1).

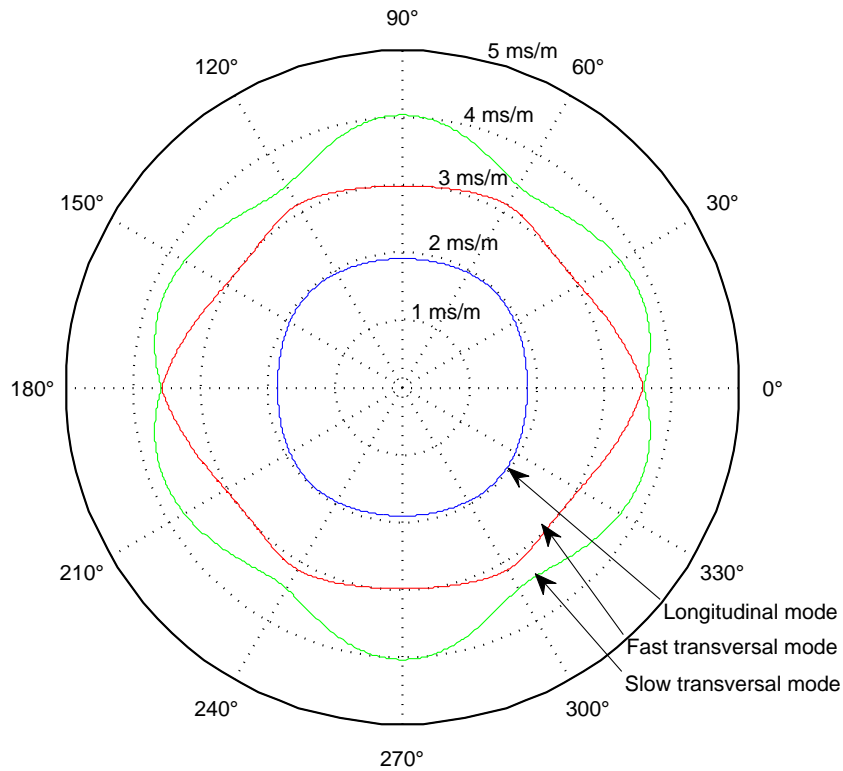


Figure 4 – Slowness curves for the plane (111) of a cubic crystal of GaAs. The three curves represent the three modes present. 0° is aligned with the $[\bar{1}11]$ direction. Image created by the author from the stiffness matrix of this material available at (1).

3.2.3 Phase and group velocities

The velocities described until now are called phase velocities, however, for modulated waves, it is possible that the carrier wave and the modulation envelope propagation velocities are not equal. The carrier velocity is the phase velocity defined previously in this text, while the modulation envelope velocity is denominated group velocity. The concepts of phase and group velocity are presented in Figure 8 below. For details about the mathematical description of the group velocity the reading of Auld's (1), Connolly's (3), Rose's (22), Royer's and Dieulesaint's (24) and Achenbach's (25) texts are recommended.

Cheeke (2) and Auld (1) highlight that, in a pulse of acoustic energy, the wavefronts travel in the direction of the wave vector \mathbf{k} , which is parallel to the phase velocity. However, the wave envelope travels in the direction of the group velocity whose direction can be different from the direction of the \mathbf{k} (1-3, 24). Figure 9 illustrates this concept.

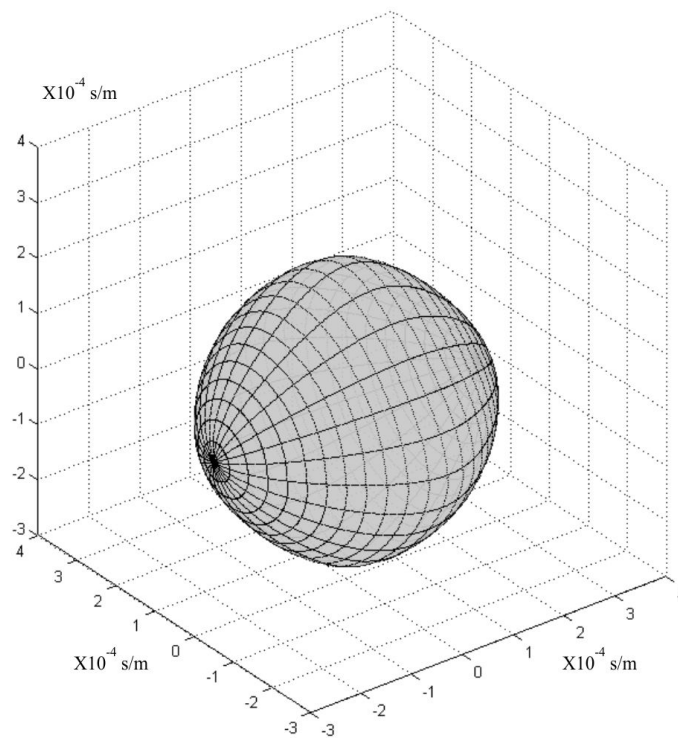


Figure 5 – Slowness surface for the longitudinal mode of GaAs, obtained by the author from the stiffness matrix of this material available at (1).

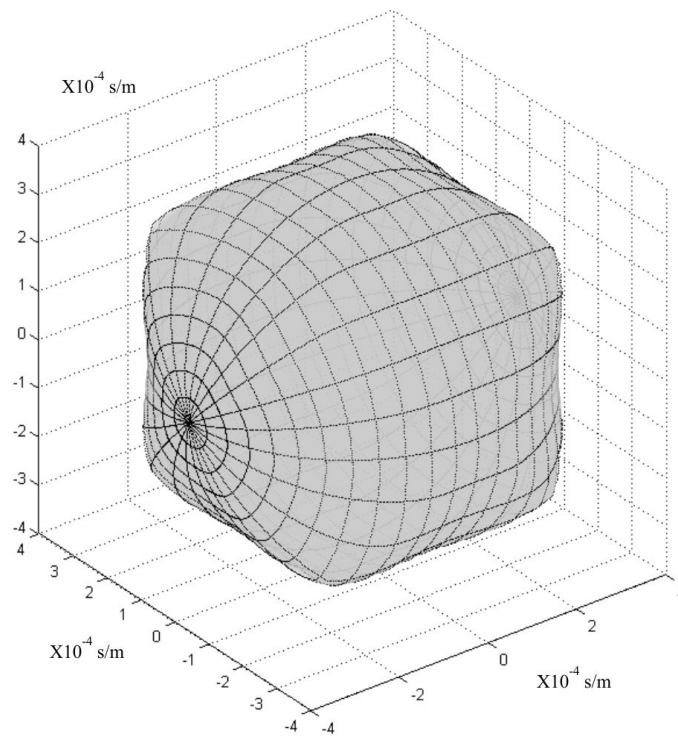


Figure 6 – Slowness surface for the fast transversal mode of GaAs, obtained by the author from the stiffness matrix of this material available at (1).

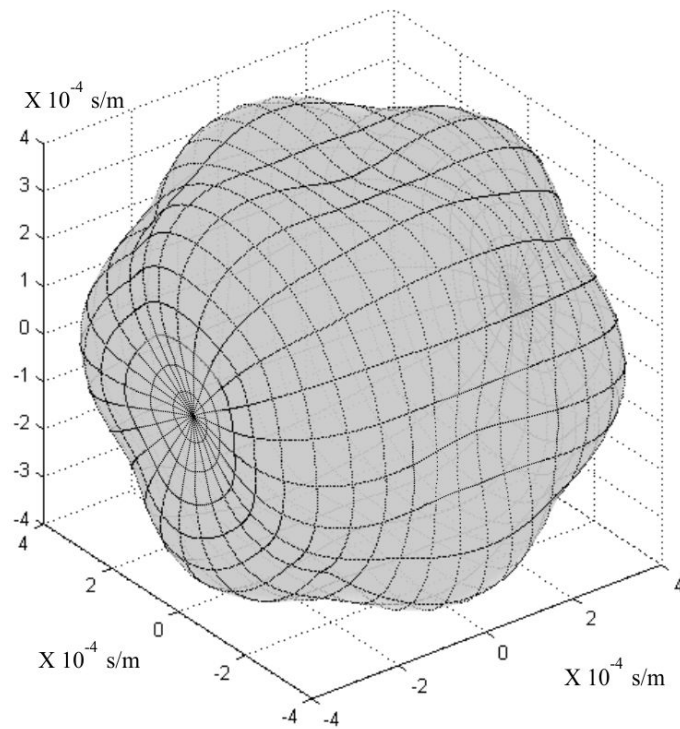


Figure 7 – Slowness surface for the slow transversal mode of GaAs, obtained by the author from the stiffness matrix of this material available at (1).

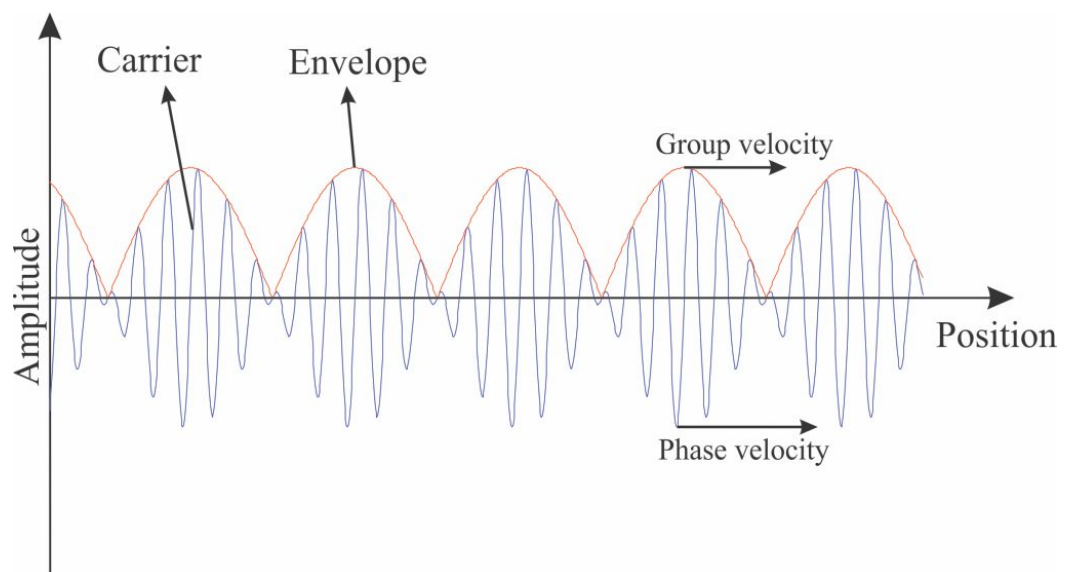


Figure 8 – Illustration of the phase and group velocities in a modulated wave. Source: the author.

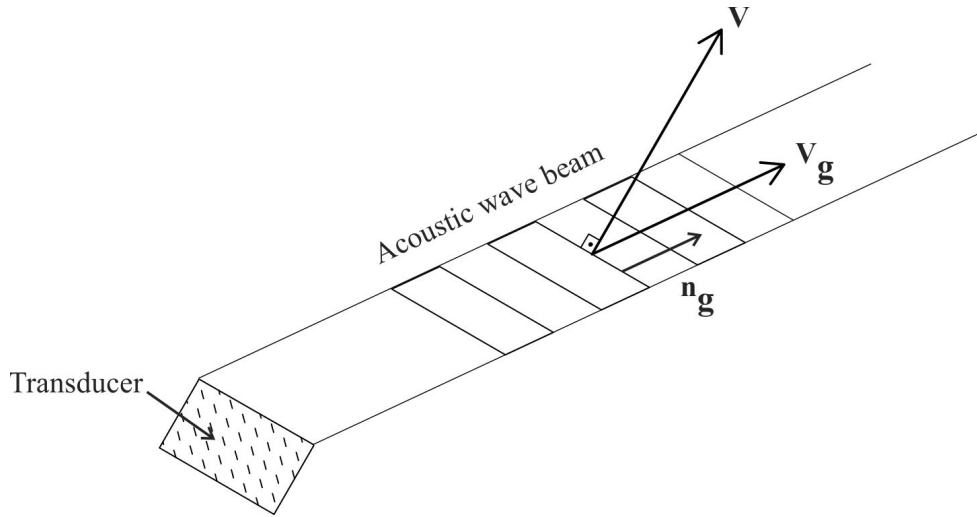


Figure 9 – Illustration of the propagation of a wave with different phase and group velocities. Adapted from Auld (1) and Cheeke (2).

Royer (24) demonstrates the wave energy velocity and the group velocity to be equal and normal to the slowness surface. More specifically, the relation between the group velocity and phase velocity is expressed by Equation 3.30.

$$\mathbf{V} = \mathbf{V}_g \cdot \mathbf{n} \quad (3.30)$$

In Equation 3.30, \mathbf{V} is the phase velocity vector, \mathbf{V}_g is the group velocity vector and \mathbf{n} is the phase unit vector. Through the rearrangement of Equation 3.30 it is possible to rewrite it in terms of the slowness vectors, this is shown in Equation 3.31, where \mathbf{m}_g and \mathbf{m} are respectively the group and phase slowness, and \mathbf{n}_g is the unit vector perpendicular to the slowness surface.

$$\mathbf{m}_g = \mathbf{m} \cdot \mathbf{n}_g \quad (3.31)$$

Given that, it is possible to calculate graphically the group slowness curves from the slowness surfaces; this procedure is illustrated by Figure 10, which was based on a figure presented by Connolly (3).

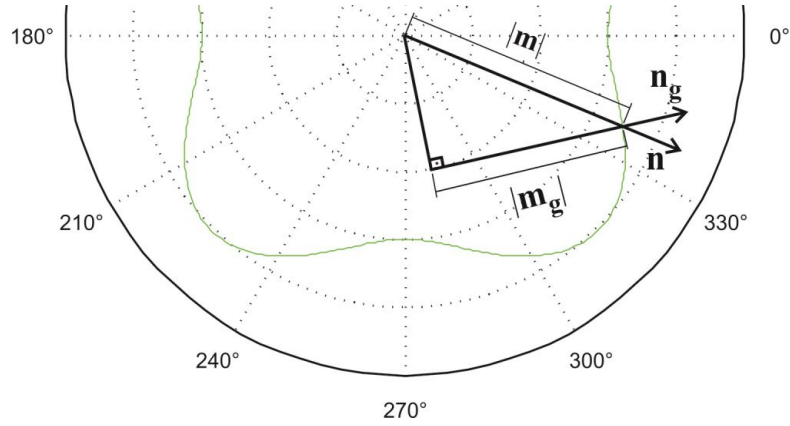


Figure 10 – Illustration of the graphic method to calculate the group slowness curve from the phase slowness curve. $|m_g|$ and $|m|$ are respectively the group and phase slowness moduli, while n_g is the unit vector perpendicular to the slowness surface and n is the phase unit vector. Adapted from Connolly (3).

Using the slowness curves presented in Figure 2, the group velocity slowness curves for GaAs were calculated for illustration purposes; the results are presented in Figure 11 as a function of the phase vector. Also, in order to complement the phase slowness surfaces presented in Figures 5, 6 and 7, the group slowness surfaces are presented as a function of the phase vector in Figures 12, 13 and 14. The method to create these group slowness surfaces uses the slowness curves employed to create the phase slowness surfaces and applies the graphic method illustrated in Figure 10 to create group slowness curves. The group slowness curves are then assembled to form Figures 12, 13 and 14 in the same way their phase counterparts were.

For some directions it is possible to have the slowness surface perpendicular to the phase vector, resulting in a group velocity vector equal to the phase velocity vector. In such cases, it is said that the wave mode is pure (24). For example, the longitudinal and second, or slow, transversal modes of Figure 2 are pure for the families of directions $\langle 100 \rangle$ and $\langle 110 \rangle$, while the first, or fast, transversal mode is pure for the $\{100\}$ plane family. When the mode is not pure it is said to be quasi-longitudinal or quasi-transversal (22).

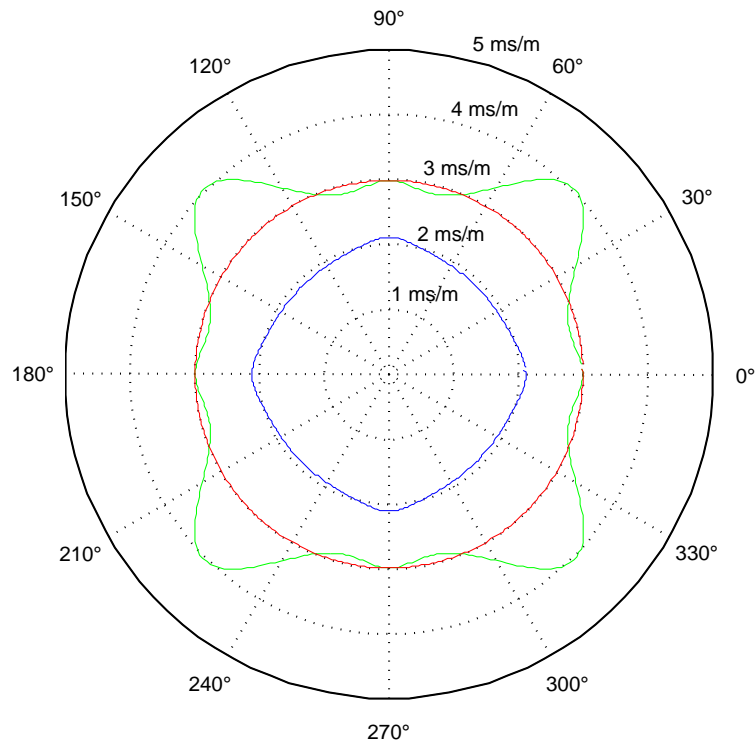


Figure 11 – Slowness group curves plotted as a function of the phase vector for the plane (001) of GaAs calculated from Figure 2 data. 0° is aligned with the [100] direction, while 90° is aligned with the [010] direction. Image obtained by the author from the stiffness matrix of this material available at (1).

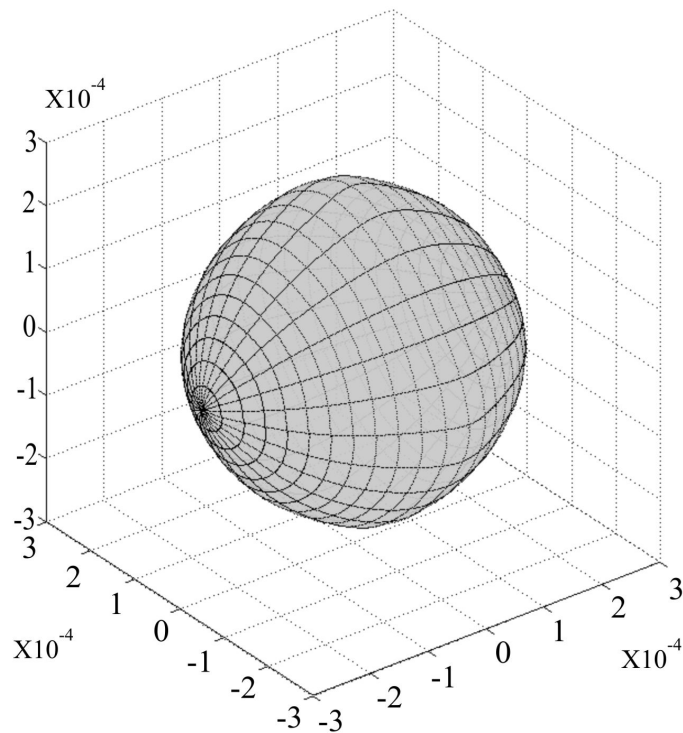


Figure 12 – Group slowness surface plotted as a function of the phase vector for the longitudinal mode of GaAs, obtained by the author from the stiffness matrix of this material available at (1).

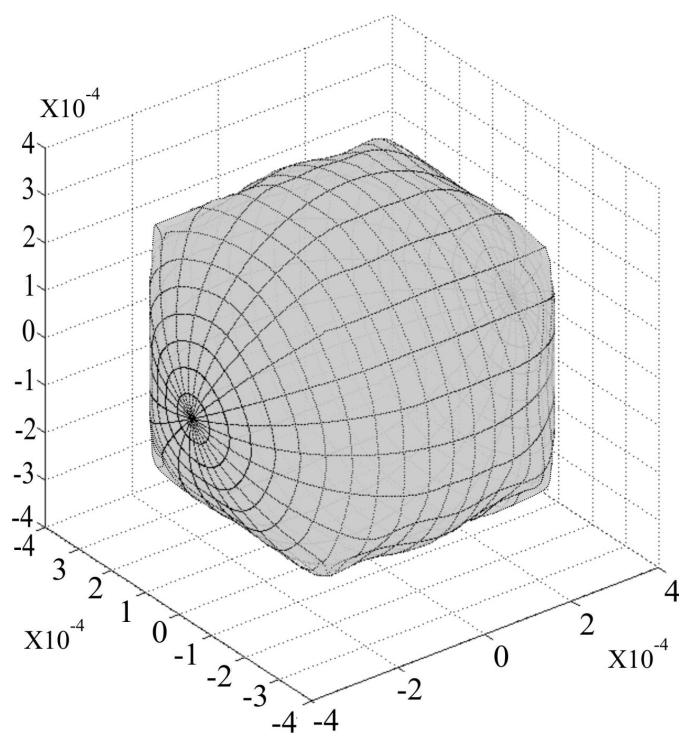


Figure 13 – Group slowness surface plotted as a function of the phase vector for the fast transversal mode of GaAs, obtained by the author from the stiffness matrix of this material available at (1).

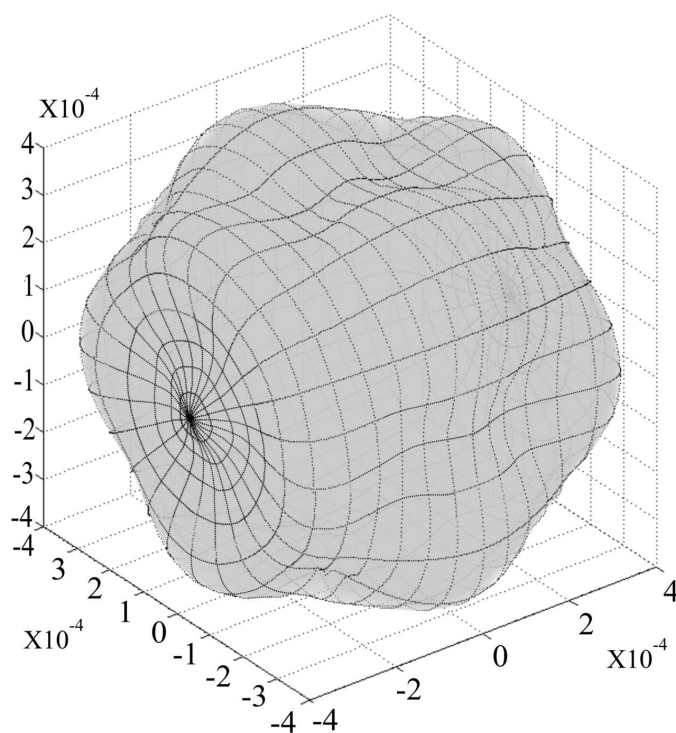


Figure 14 – Group slowness surface plotted as a function of the phase vector for the slow transversal mode of GaAs, obtained by the author from the stiffness matrix of this material available at (1).

3.3 Full matrix capture and total focusing method

Conventional array ultrasonic inspection typically uses combinations of its elements to mimic a single element transducer, so that one may focus the ultrasonic beam in a specific point of the material, or to generate a plane wavefront (26). This approach does not take into account all the information the array can provide. The maximum information one can take from an ultrasonic array can be obtained from the Full Matrix Capture (FMC), which is a matrix containing the A-scans from all the possible combinations of emitter and receiver transducers (26). The FMC is acquired by firing one element of the array at a time and receiving the material's response with all the elements in the array. Once every element has been fired and the data acquisition completed, the resulting dataset is the FMC (26,27). Figure 15 illustrates the FMC acquisition process.

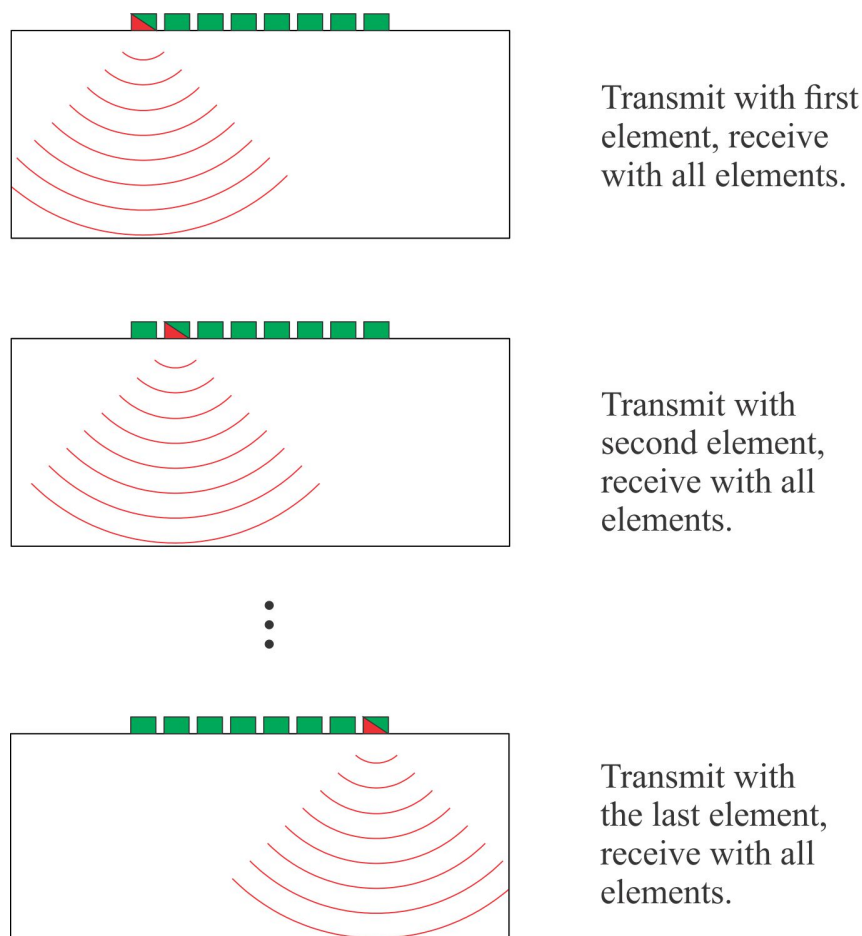


Figure 15 – FMC acquisition process. Source: the author.

In order to obtain useful images out of the FMC, it is necessary to post-process it. Virtually all the delay laws that can directly be applied to the phased array can be synthesised by manipulating the FMC, resulting in equivalent results. In addition to conventional delay laws, the FMC or a subset of the FMC data gives the opportunity to generate images by methods that are not viable to employ in conventional phased array imaging. SAFT (synthetic aperture focusing techniques) method, which is commonly used in radar (SAR - synthetic aperture radar) and sonar imaging (SAS - synthetic aperture sonar) is a known example of such post-processing techniques. SAFT uses only the A-scans received by the same transducer responsible for its emission. Hence, it does not require the acquisition of the whole FMC. Further details about this imaging technique, which will not be used here, can be found in the references (28–30).

The FMC can also be manipulated to focus, with all the combinations of transducers in every point of a region of interest inside the field of view of the array (31–33). This procedure is called Total Focusing Method (TFM) and can be mathematically represented by Equation 3.32 based on Holmes et al. (26) work. Figure 16 illustrates this imaging method. Both the FMC and TFM, on a first glance, are thought to be time-consuming and computationally demanding to obtain; however, it is possible to obtain TFM images in real-time with commercially available equipment (34).

$$I_{TFM}(x, y) = \left| \sum_{m=1}^N \sum_{n=1}^N A_{m,n} \left(t_{x,y,m} + t_{x,y,n} \right) \right| \quad (3.32)$$

In Equation 3.32 $I_{TFM}(x, y)$ is the intensity of the pixel located at (x, y) coordinate; $A_{m,n}$ is the A-scan taken from the FMC for transmitter m and receiver n ; N is the number of elements in the array; $t_{x,y,m}$ and $t_{x,y,n}$ are the time taken by the sound to travel between the transmitting element m and the focusing point and between the focusing point and the receiving element n , respectively. Due to reciprocity principle, $t_{x,y,m}$ is independent of the

propagation direction, i.e. $t_{x,y,m}$ is the same regardless of the transducer is the transmitter or receiver. Given that, the time of flight is defined by Equation 3.33.

$$t_{x,y,m} = \frac{\sqrt{(x - X_m^0)^2 + (y - Y_m^0)^2}}{c} \quad (3.33)$$

In Equation 3.33, X_m^0 and Y_m^0 are the coordinates of the centre of the transducer m and c is the sound speed of the medium.

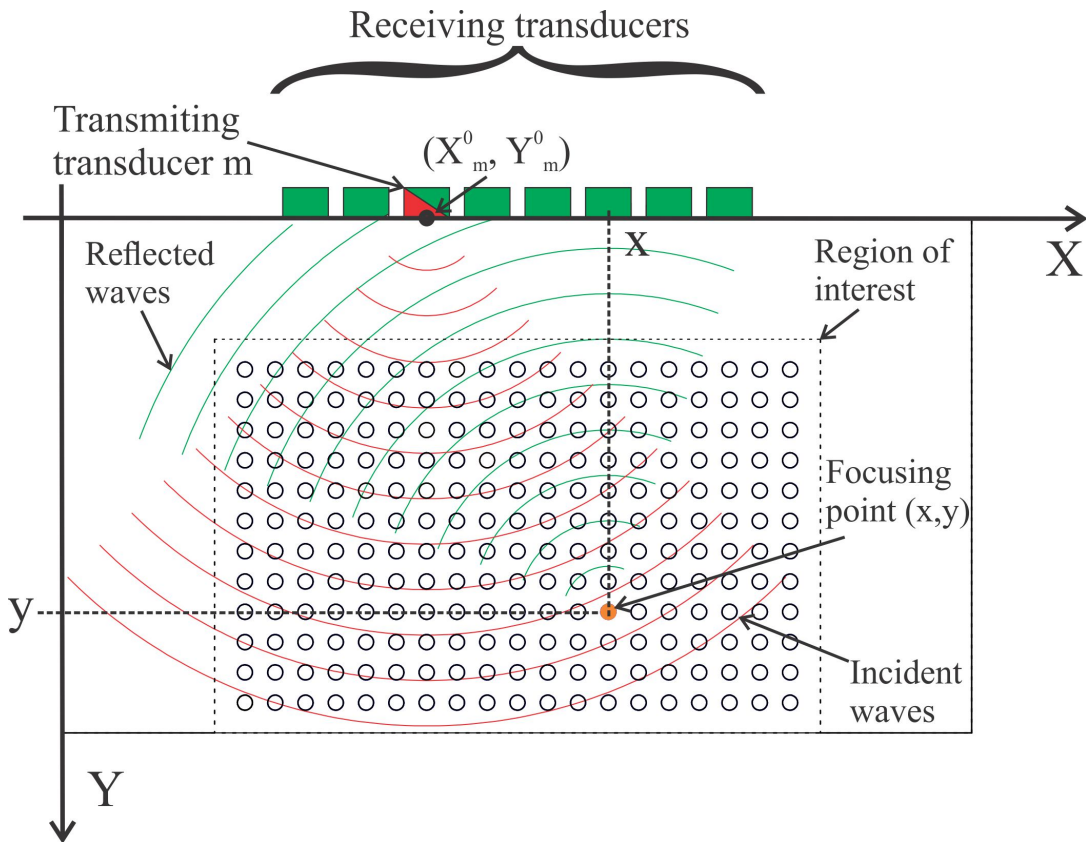


Figure 16 – TFM imaging process. Source: the author.

Equation 3.33 only works when the array is positioned directly on a homogeneous and isotropic test piece. This usually is not the case for real-world applications. Normally, a shoe, wedge or water layer, with different acoustic wave speed than the test sample, is present between the transducer and the test sample. Due to the acoustic wave speed mismatch between them, it is necessary to recalculate the wave path and rewrite Equation

3.33, which leads to Equation 3.34 (31). An illustration of the dual layer media problem is presented in Figure 17

$$t_{x,y,m} = \frac{\sqrt{(X_{x,y,m}^a - X_m^0)^2 + (Y_{x,y,m}^a - Y_m^0)^2}}{c_1} + \frac{\sqrt{(x - X_{x,y,m}^a)^2 + (y - Y_{x,y,m}^a)^2}}{c_2} \quad (3.34)$$

In Equation 3.34 X_m^0 and Y_m^0 are the coordinates of the centre of the transducer; x and y represent the coordinates of the focusing point, $X_{x,y,m}^a$ and $Y_{x,y,m}^a$ are the coordinates of the intersection point between the two media; c_1 and c_2 are the acoustic wave velocities of the coupling medium and the test piece, respectively. For this equation, the transducer's coordinates and the focusing point coordinates are known, but the intersection point between the two media where the wave beam refracts is not known. Nevertheless, assuming that the refraction follows Fermat's principle, it is possible to derive Snell's law (31), which is presented in Equation 3.35.

$$\frac{\sin(\theta_1)}{c_1} = \frac{\sin(\theta_2)}{c_2} \quad (3.35)$$

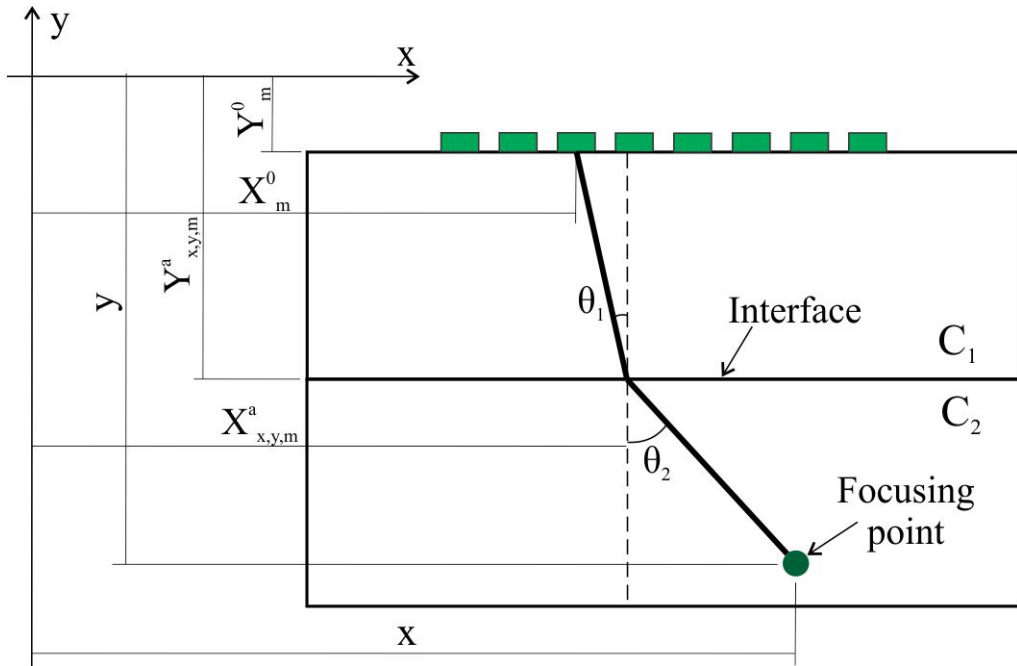


Figure 17 – Dual layer media wave path calculation method. Source: the author.

In Equation 3.35, θ_1 and θ_2 are the incidence and refraction angles, respectively (see Figure 17). To obtain the incidence point, one first needs to rewrite Snell's law into its general form (35), presented in Equation 3.36

$$\frac{c_1}{c_2} \frac{(x - X_{x,y,m}^a)}{(X_{x,y,m}^a - X_m^0)} = \frac{\sqrt{(x - X_{x,y,m}^a)^2 + (y - Y_{x,y,m}^a)^2}}{\sqrt{(X_{x,y,m}^a - X_m^0)^2 + (Y_{x,y,m}^a - Y_m^0)^2}} \quad (3.36)$$

By rearranging Equation 3.36 and considering a planar interface, i.e. considering $Y_{x,y,m}^a$ constant, it is possible to obtain a 4th order polynomial (35), which is presented in Equation 3.37.

$$\alpha_4 X_{x,y,m}^a{}^4 + \alpha_3 X_{x,y,m}^a{}^3 + \alpha_2 X_{x,y,m}^a{}^2 + \alpha_1 X_{x,y,m}^a + \alpha_0 = 0, \text{ where:} \quad (3.37)$$

$$\alpha_4 = \beta - 1,$$

$$\alpha_3 = -\beta (2x + 2X_m^0) + 2x + 2X_m^0,$$

$$\alpha_2 = -X_m^0{}^2 + \beta X_m^0{}^2 - 4X_m^0 x + 4\beta X_m^0 x - x^2 + \beta x^2 - (Y_{x,y,m}^a - Y_m^0)^2 + \beta (y - Y_{x,y,m}^a)^2,$$

$$\alpha_1 = 2xX_m^0 - 2\beta xX_m^0{}^2 + 2X_m^0 x^2 - 2\beta X_m^0 x^2 + 2x (Y_{x,y,m}^a - Y_m^0)^2 - 2\beta X_m^0 (y - Y_{x,y,m}^a)^2,$$

$$\alpha_0 = -x^2 X_m^0{}^2 + \beta x^2 X_m^0{}^2 - x^2 (Y_{x,y,m}^a - Y_m^0)^2 + \beta X_m^0{}^2 (y - Y_{x,y,m}^a)^2 \text{ and}$$

$$\beta = \frac{c_2^2}{c_1^2}.$$

This polynomial equation can be solved by Ferrari's analytical method (35, 36). For a polynomial of the form presented in Equation 3.37, the solution through Ferrari's method is obtained by solving Equations 3.38 to 3.47 below (31, 35):

$$f_1 = \frac{-3\alpha_3^2}{8\alpha_4^2} + \frac{\alpha_2}{\alpha_4} \quad (3.38)$$

$$f_2 = \frac{\alpha_3^3}{8\alpha_4^3} - \frac{\alpha_3\alpha_2}{2\alpha_4^2} + \frac{\alpha_1}{\alpha_4} \quad (3.39)$$

$$f_3 = \frac{-3\alpha_3^4}{256\alpha_4^4} + \frac{\alpha_2\alpha_3^2}{16\alpha_4^3} - \frac{\alpha_3\alpha_1}{4\alpha_4^2} + \frac{\alpha_0}{\alpha_4} \quad (3.40)$$

$$f_4 = -\frac{f_1^2}{12} - f_3 \quad (3.41)$$

$$f_5 = -\frac{f_1^3}{108} + \frac{f_1 f_3}{3} - \frac{f_2^2}{8} \quad (3.42)$$

$$f_6 = -\frac{f_5}{2} \pm \sqrt{\frac{f_5^2}{4} + \frac{f_4^3}{27}} \quad (3.43)$$

$$f_7 = \sqrt[3]{f_6} \quad (3.44)$$

$$f_8 = -\frac{5}{6}f_1 + f_7 - \frac{f_4}{3f_7} \quad (3.45)$$

$$f_9 = \sqrt{f_1 + 2f_8} \quad (3.46)$$

$$f_{10} = -\frac{\alpha_3}{4\alpha_4} + \frac{\pm_1 f_9 \mp_2 \sqrt{-\left[3f_1 + 2f_8 \pm_1 \left(\frac{2f_2}{f_9}\right)\right]}}{2} \quad (3.47)$$

It is also possible to solve Equation 3.36 numerically or iteratively, but the computation time required would significantly increase (35). Therefore, due to its relative implementation simplicity, solution time and accurate results, Ferrari's analytical method was preferably used throughout the present work. In their work, Weston et al. (35), highlight the impossibility to apply an analytical method for non-planar interfaces because in those cases the Snell's law results in a polynomial with order greater than four. For such situations, it is required to solve the equation with numerical or interactive methods.

3.4 Ultrasonic inspection in anisotropic and inhomogeneous materials

To address the problems caused by anisotropy and inhomogeneity in ultrasonic inspection of coarse-grained material, one needs first to consider reducing the sound frequency used in the inspection. By reducing the sound frequency, the inspection system moves towards the Rayleigh regime (4). However, this method is often not enough to overcome the anisotropy and inhomogeneity issue or the resolution loss caused by a lower frequency culminates in less meaningful or even useless results. Several other approaches in the literature can be used to deal with this matter; some of them, primarily those commonly used in linear phased array inspection, are briefly explained next in this text.

3.4.1 Decomposition of the time reversal operator and multiple scattering filter

The decomposition of the time reversal operator, also known by its French acronym DORT, is a selective detection and focusing technique (37). Once the FMC is obtained, the response matrix \mathbf{K} is calculated by truncating the full matrix in overlapping time windows followed by a short-time Fourier analysis (20). This procedure results in a complex matrix $\mathbf{K}(t, f)$ that allows the calculation of the delays to back-propagate the signal into the material and focus them in a specific scatterer (20, 38). However, when this technique is applied to a noisy material, multiple scattering is dominant and the produced results are poor (20).

It was observed that when the multiple scattering is strong, \mathbf{K} is close to a random matrix, but when single scattering dominates it assumes the form of a Hankel matrix (20). Hence, it was possible to define \mathbf{K} as a sum of two matrices; one taking into account the multiple scattering and another the single scattering (20, 39, 40). The contribution of the target is restricted to the single scattering part of \mathbf{K} and the structural grain noise contribution is present in both parts of \mathbf{K} . So, by reducing the multiple scattering part of \mathbf{K} it is possible to reduce the noise in the images. This reduction was demonstrated to be

beneficial to the performance of the inspection on a sample of Inconel600 [®](20). The fact that this method does not require any information about the grain structure is one of its main advantages.

3.4.2 Grain orientation assessment

Another approach to deal with the anisotropy and inhomogeneity issues on ultrasonic phased array inspection is to assess the grain orientation through modelling or measurements. With this approach, it is possible to calculate appropriate delay laws in order to properly focus the ultrasonic beam by taking the beam skewing caused by the material into account. Several methods have been developed to obtain the grain orientation; among them there is the direct measurement of the grain orientation from macrograph (10) or EBSD (electron backscattering diffraction) (4,41,42). It is important to notice that, besides those methods being the most accurate, they are destructive since it is required to cut the part under analysis to obtain a macrograph or EBSD image. Whereas the images produced by those methods are only capable of representing the sample in the vicinity of where they came from, it is sometimes necessary to repeat the analysis on multiple cuts over the sample. This extra work increases the cost and the time taken to acquire the necessary information, especially for the extensive and high-resolution EBSD images.

For the specific problem of anisotropic and inhomogeneous welds, MINA (Modelling anisotropy from notebook of arc welding) (11) was developed as a non-destructive alternative to assess the grain orientation problem. Mina's objective is to describe the grain orientation using data from the welding report such as the diameter of electrodes, chamfer geometry and number of passes (11,43). Overall, MINA achieved its objective in several occasions(10,11,43–46).

However, the orientation map provided by MINA needs to be fed to a software capable of modelling the sound wave propagation such as the ATHENA code (11,47). Originally, MINA was developed to feed ATHENA (11), nevertheless other software tools can also be used, such as PZFlex (10,48).

Ogilvy (49) developed another way to predict the grain orientation, which was used elsewhere (3,50,51). Nevertheless, this orientation parametrisation is only valid for single V-butt welds (49,50). This approach estimates the grain orientation by considering the material transversely isotropic and calculating the angle of the elastic constants as a function of the weld axis system (3,49).

Furthermore, it has been demonstrated that it is possible to assess critical parameters of a weld by employing an inverse model that manipulates experimental data via a genetic algorithm (46). Fan et al. (46) proposed a method inspired by the work of Gueudre et al. (44), which utilises MINA's formulation as a way to represent the weld stiffness matrix orientation. The experimental set up consisted of two phased array probes positioned along the welded sample; one working as a generator and the other as a receptor. The acoustic waves emitted by the generator interacted with the weld, reflected at the bottom surface of the specimen and arrived at the receptor. The registered time of flight was used in the genetic algorithm to determine the set of MINA's parameters that better describes the acoustic behaviour of the test piece.

3.4.3 Ultrasonic wave propagation problem

When one of the approaches described in the subsection 3.4.2 is used, it is necessary to employ a propagation method to be able to identify the path taken by the acoustic beams inside the material and obtain useful data about the integrity of the component. Among the several approaches developed to achieve this, there are the ray-tracing methods, used by some authors with Ogilvy model of grain orientation in V-butt welds (3,49,50), that can be used in association with MINA as well (52) and possibly with other forms of grain orientation modelling and measurements.

There are various kinds of ray-tracing methods; some of them are described by Nowers et al. (52) and Connolly (3). Nowers et al. (52) describe two methods based on an algorithm used to solve the travelling salesman problem called Dijkstra's algorithm and another interactive method that bends a simulated ray in order to find the fastest path between an emitting and an exit point. The later follows the Fermat's principle which

states that a ray will follow the fastest path. Connolly (3), on the other hand, describes a method where a ray is assigned with phase vector and to an initial point, then, the ray is allowed to travel along its group vector until it finds a boundary or an anisotropic inhomogeneous region. When a boundary is found the ray is terminated, reflected or refracted. Also, in an anisotropic region, from time to time, the ray direction is corrected according to the crystallographic orientation of the material. Among the interesting results brought by Connolly's thesis, the identification of regions inside the weld where ultrasonic beams cannot penetrate from specific starting points is emphasised here.

It is also possible to feed grain orientation data directly into finite element packages capable of dealing with acoustic wave propagation problems in order to model the inspection (5, 10). For example, Limthongkul (5) used PZFlex to model the sound field incident to the back wall of an austenitic weld block, which is one of the samples used in the present work. In addition, there is also a commercial software tool that relies on semi-analytical ray-tracing to model ultrasonic wave propagation called CIVA which is commercialised by EXTENDE (3, 53).

3.4.4 Adaptive ultrasonic imaging

The concept of adaptive ultrasonic imaging relies on corrections in the delay law used to focus the ultrasonic energy of a phased array probe in a point of interest inside the material. Those corrections can be obtained experimentally or with the aid of computer simulation (4). Regardless of the employment of an experimental or computational method, the operation principle remains the same. According to Channa et al. (12), every element, one at a time, is fired and the the same element acquires the signal after it interacts with a target. After repeating this for all the elements in the phased array, one can calculate the adapted delay law (ADL) needed to be applied to the array in order to force the ultrasonic beam from every element to reach the target at same time. The delay, also called temporal phasing, can be challenging to calculate from experimental data due to excessive attenuation imposed by the material, i.e. the target signal is not distinguishable from the background noise (4). Also, for the experimental route, a reflector or target to serve as a

focusing point for the phased array is needed. This may raise the need to manufacture a calibration block with a geometric feature inserted, such as a side-drilled hole, to be able to calculate the ADL. For those reasons, the experimental approach is often not suitable for thick section samples, and when chosen, a strict qualification procedure must be applied (4). The process to calculate the ADL is illustrated by Figure 18.

In Figure 18, the elements are fired one at a time (part a) and the time of flight from the transducer to the target and back to the same transducer is recorded (blue bars). After the calculation of the adapted time delays required to be applied in every transducer is calculated (red bars), the ADL is applied to the array (part b).

3.4.5 Coherence weights

Hollman et al. (54) explain that conventional ultrasonic imaging sums signals from the elements in the array. However, due to beam skewing, their amplitude can be positive or negative at the focusing point, which means that when peaks and troughs from different transducers meet in the focusing point, they will cancel each other. Similarly, when troughs or peaks from different transducers meet they will constructively interfere with each other, increasing the final amplitude. This is referred to as coherent sum (54). On the other hand, if the signals are squared before summation, troughs cease to exist and all the signals add up constructively, which is referred to as incoherent sum (54).

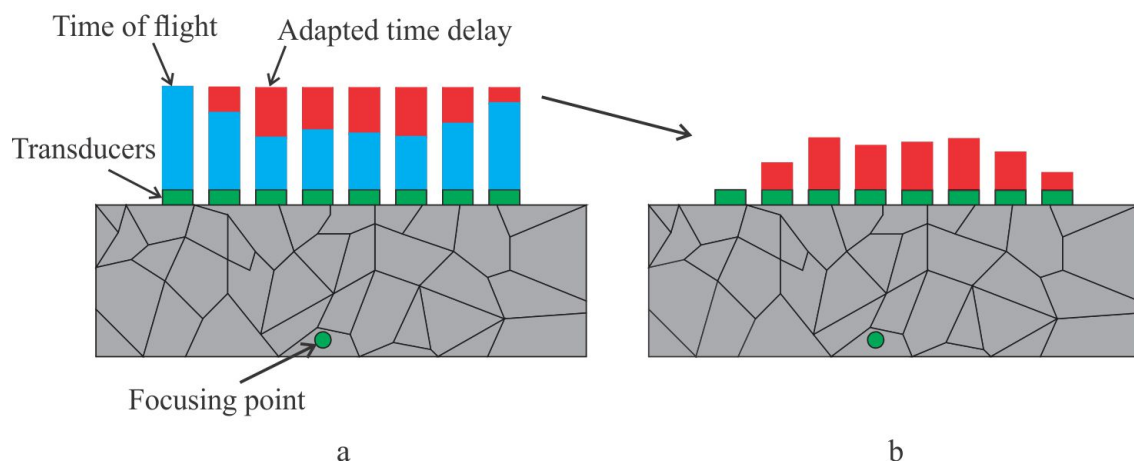


Figure 18 – Illustration of the ADL method. a) adapted time delay calculation from the time of flight and b) adapted time delay used to focus the phased array. Source: the author.

With this in mind, Mallart and Fink (55) developed a method based on the ratio between the coherent sum squared to the incoherent sum, which was termed Coherence Factor (CF) (54, 56). To apply Mallart and Fink's (55) line of thought to a TFM image, first the coherent intensity, CI, of the signals sensed by the array elements is defined by Equation 3.48.

$$CI = \left| \sum_{m=1}^N \sum_{n=1}^N A_{m,n} (t_{x,y,m} + t_{x,y,n}) \right|^2 \quad (3.48)$$

In Equation 3.48 N is the number of transducer in the linear array, $A_{m,n}$ is the A-scan coming from emitter transducer m and receptor transducer n , t is the time of flight for a wave to travel between the focusing point (x, y) and the emitter or receptor. Applying the Cauchy-Schwartz inequality, $0 \leq |\sum_i a_i b_i|^2 \leq \sum_i |a_i|^2 \cdot \sum_i |b_i|^2$, to 3.48 by setting $a_i = A_{m,n} (t_{x,y,m} + t_{x,y,n})$ and $b_i = 1$, Equation 3.49 is obtained.

$$0 \leq \left| \sum_{m=1}^N \sum_{n=1}^N A_{m,n} (t_{x,y,m} + t_{x,y,n}) \right|^2 \leq \sum_{m=1}^N \sum_{n=1}^N |A_{m,n} (t_{x,y,m} + t_{x,y,n})|^2 \quad (3.49)$$

By normalizing Equation 3.49 with its rightmost term, one obtains Equation 3.50 which calculates CF to be used with images created via TFM.

$$CF(x, y) = \left(\frac{|\sum_{m=1}^N \sum_{n=1}^N A_{m,n} (t_{x,y,m} + t_{x,y,n})|^2}{N^2 \sum_{m=1}^N \sum_{n=1}^N |A_{m,n} (t_{x,y,m} + t_{x,y,n})|^2} \right)^{P_{CF}} \quad (3.50)$$

In Equation 3.50 the exponent P_{CF} is the sensitivity factor used by Knight-Gregson et al. (56) to adjust how steep the difference between a coherent and an incoherent region is.

The parameter CF can be considered to be a normalised measure of the coherence of the backscattered signal from an (x, y) point in the material. This parameter was shown to be independent of the scattering, attenuation and transmitted energy and only depends on the spatial correlation function of the acoustic pressure field incident in the array (55).

The primary function of CF is to reduce the side lobes (57, 58); since it is unlikely that signals with the same time of flight but coming from side lobes will have the same

phase as those coming from the main lobe. As a consequence, their CF will be relatively small and if Equation 3.50 is applied to all the (x, y) points in the image a weighting matrix is created which can be multiplied by the TFM image in order to improve its SNR. Equation 3.51 demonstrates this, where $ICF(x, y)$ is the weighted pixel intensity matrix, that latter will be used to plot the modified image.

$$ICF(x, y) = CF(x, y) * I_{TFM}(x, y) \quad (3.51)$$

Originally, Mallart and Fink (55) developed this approach as a focusing criterion to be used to correct aberrations in medical ultrasonics, and it has been used for this purpose ever since (54, 57, 58), but it has also been used in NDT demonstrating to be beneficial when applied with TFM (56). Knight-Gregson et al. (56) used the CF with TFM imaging in order to attenuate noise and improve the signal to noise ratio (SNR). Also, with the introduction of P_{CF} , it is possible to adjust CF to resolve specular reflections better .

Camacho et al. (59, 60) developed other forms capable of reducing side lobes and grating lobes influence in the ultrasonic imaging. Unlike the method developed by Mallart and Fink (55), those methods are based on the analysis of the phase distribution of the data. Camacho et al. (59) explain that a simple way to verify if the signals come from the focusing point, i.e. if they come from the main lobe, is to look at the phase variations. In their work this was done by calculating the standard deviation of the normalised phase of the signals at the focusing point. In other words, if the signals are coming from a focusing point, their phases will present little dispersion between the elements, but if the signals come from the side or grating lobes the phase dispersion will be closer to random.

Nevertheless, an issue arises when dealing with the normalised phase of the signals. For example, if the phases are normalised between the interval $(-\pi, +\pi)$, when the average of the phases coming from a focusing point is close to $-\pi$ or π , hence close to the discontinuity present around these two values, their standard deviation will be much higher than if the phase average was close to, for instance, zero. To bypass this problem an additional set of phases was created, equal to the original one, but subtracting π in

case the original phase is negative or adding π in case the phase is positive. This operation moves the phase average away from the discontinuity. Next the standard deviation of both sets of phases are computed, but only the smaller standard deviation is taken into account.

With this in mind, Equation 3.52 was developed (59) to calculate what was called Phase Coherence Factor (59) (PCF):

$$PCF(x, y) = \begin{cases} 1 - \frac{\sigma_p(x, y) * P_{PCF}}{\sigma_0}, & \text{if } \frac{\sigma_p(x, y) * P_{PCF}}{\sigma_0} < 1, \\ 0, & \text{otherwise} \end{cases} \quad (3.52)$$

Where $PCF(x, y)$ is the phase coherence factor for a focusing point located at the coordinates (x, y) , $\sigma_p(x, y)$ is the minimum standard deviation of the two sets of phases at the (x, y) focusing point, σ_0 is the standard deviation of a random phase distribution between $-\pi$ and π , equals to $\pi/\sqrt{3}$, and P_{PCF} is the sensitivity factor which behaves differently than P_{CF} but is intended to serve the same purpose.

Unlikely P_{CF} , P_{PCF} does not have a maximum value, dictated by $\sigma_p(x, y)$. This maximum value is reached when $\sigma_p(x, y) * P_{PCF} = \sigma_0$. At this point the upper part of Equation 3.52 becomes negative and $PCF(x, y)$ needs to be brought back to zero in order to keep $PCF(x, y)$ between zero and one. With $PCF(x, y)$ kept between zero and one, it is possible to use it as a weighting matrix for the TFM image. Similarly to Equation 3.51, Equation 3.53 is created, where $IPCF(x, y)$ is the weighted pixel intensity matrix, equivalent to $ICF(x, y)$.

$$IPCF(x, y) = PCF(x, y) * I_{TFM}(x, y) \quad (3.53)$$

Camacho et al. (59) presented in their article another weighting factor, also based on the phase distribution of the signals, termed Sign Coherence Factor (SCF). This coherence factor is calculated by splitting the normalised phases into two parts: one for the phases comprised in the interval $(-\pi/2, \pi/2]$ and another for the phases in the intervals $[-\pi, -\pi/2]$ and $(\pi/2, \pi]$, which separates the data by their polarity. This data is then

classified as coherent or incoherent by a coherence criterion, which states that the data set is coherent only if all the signals have the same polarity.

To be able to calculate SCF, first the variable $s_{m,n}(x, y)$ is defined. This variable is the phase sign of the signal from a (m, n) pair of transducers when focusing on a (x, y) point and is calculated by Equation 3.54 below:

$$s_{m,n}(x, y) = \begin{cases} -1, & \text{if } A_{m,n}(t_{x,y,m} + t_{x,y,n}) < 0, \\ +1, & \text{if } A_{m,n}(t_{x,y,m} + t_{x,y,n}) \geq 0. \end{cases} \quad (3.54)$$

The variance of $s_{m,n}(x, y)$ over all the emitter and receiver combinations for a given focusing point, $\sigma(x, y)^2$, is:

$$\sigma(x, y)^2 = N \sum_{m=1}^N \sum_{n=1}^N s_{m,n}^2 - \left(\sum_{m=1}^N \sum_{n=1}^N s_{m,n} \right)^2 \quad (3.55)$$

Equation 3.55 can be applied to Equation 3.52 and making the sensitivity factor and σ_0 equals 1 it creates Equation 3.56 below:

$$SCF(x, y) = \left| 1 - \sqrt{1 - \left[\frac{1}{N} \sum_{m=1}^N \sum_{n=1}^N s_{m,n}(x, y) \right]^2} \right|^{P_{SCF}}, \quad (3.56)$$

where $SCF(x, y)$ is the sign coherence factor for the (x, y) focusing point and P_{SCF} is its sensitivity factor. $SCF(x, y)$ is applied to $I_{TFM}(x, y)$ in the same way as P_{CF} and P_{PCF} , which leads to Equation 3.57, where $ISCF(x, y)$ is the weighted pixel intensity matrix, equivalent to $ICF(x, y)$ and $IPCF(x, y)$.

$$ISCF(x, y) = SCF(x, y) * I_{TFM}(x, y) \quad (3.57)$$

Camacho et al. (59) demonstrated that SCF is stricter than PCF . PCF and SCF have been used in several opportunities (56, 60–62) with success. However, when Zhang et al. (63) compared SCF with other imaging methods they demonstrated that, besides SCF providing images with better resolution than TFM, this coherence weighting factor can conceal specular reflections in the images and must be used carefully.

3.5 Summary

This chapter presented the concepts needed as a foundation for the work described further on in this thesis alongside the mathematical tools and methods used throughout the text. The main points are the description of the Christoffel Equation used to model the wave propagation inside inhomogeneous and anisotropic materials, which leads to the description of the phase and group slowness surfaces and the description of the FMC/TFM imaging methods and its variations present in the literature. Among those methods, the approaches from which the methods investigated in this thesis are based on are introduced.

4 METHODOLOGY

This chapter is divided into two sections, in the first one the Adaptive Delay Total Focusing Method (ADTFM), intended to correct the position of indication in acoustic images of austenitic materials, is introduced alongside a detailed description of the methodology required for its employment. The sample used to test the ADTFM is presented, as well as the experimental procedure used in the acquisition of the mechanical stiffness matrix via acoustic measurements in a cylindrical single crystal. The first section ends with the experimental methodology employed to obtain the data of the test piece. In the second section, the mechanically lined pipes and the sample built to mimic the triple joint region located near the girth weld area of those pipes are presented. This sample was used to demonstrate the capabilities of the coherence weights in reducing the signal to noise ratio and the amplitude and presence of false indications in TFM images. The second section is completed by the description of the experimental procedure to collect the experimental data used to create the TFM images.

4.1 Adaptive delay total focusing method

The nuclear and the oil & gas industry face an important issue regarding the inspection of austenitic welds to ensure the safe operation of their equipment (4). This issue is a consequence of the anisotropic and inhomogeneous characteristics of those materials, from the ultrasonics point of view, caused by its coarse grain structure. Section 3.1 described the anisotropy and inhomogeneity of such materials in more details. This section introduces the concept of Adaptive Delay Total Focusing Method or ADTFM, which was developed as an alternative to reduce the problems caused by anisotropy and inhomogeneity in austenitic materials, followed by the methodology used in its application.

4.1.1 Adaptive delay total focusing method description

The adaptive delay total focusing method, or ADTFM, works by obtaining the time of flight for all the combinations of transducers and focusing points in a suitable software package such as PZFlex¹ (48) using a representation of the crystallographic orientation such as one of those described at Section 3.4.2. The usage of PZFlex in this work can be justified by its ability to introduce the orientation map from spreadsheets accurately and in a simple way in comparison with other FEA packages at disposal. From the available options, it was chosen to represent the crystallographic orientation map using the EBSD map due to its accuracy and availability. From the time of flight calculated via this simulation, the ADL is calculated for every focusing point and stored for later use as delay laws in the experimental FMC.

The proposed method can be visualised in detail in the diagram presented in Figure 19. Once with a description of the materials crystallographic orientation, the first step, as mentioned above, is to simulate the time of flight (TOF) for all the combinations of transducers and focusing points. Nonetheless, this step would require a model to run once for every one of the possible combinations. As an example, for a 32 elements probe and using a TFM grid of 20 x 40 points, the number of runs would be $32 * 20 * 40 = 25600$. Solving such amount of simulations would require an impractical amount of time even in standard cluster computers. A way to dramatically reduce the computation time can be achieved by insonifying the virtual transducer located on the focusing point and configuring the phased array elements only as receivers instead of insonifying the model via the phased array elements one at a time. This approach is similar to the one employed by Van Pamel et al. (64). Figure 20 illustrates the idea of the virtual transducer excitation. By insonifying the focusing point only half of the wave path is modelled, reducing the simulation time even further by a factor of two when the model is run in the time domain, such as in PZFlex's models. With this, there is a reduction in the amount of time required to run all the simulations by, approximately, a factor equal to twice the number of transducers in the phased array probe.

¹Other software can be potentially used for this task, but in this work the discussion will focus on PZFlex since it was the software package used here.

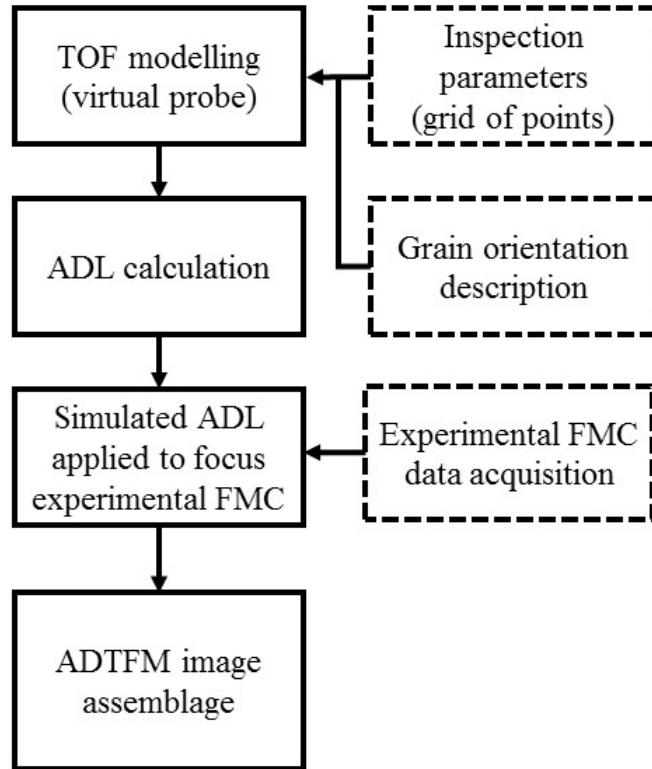


Figure 19 – Diagram showing the steps involved to obtain an ADTFM image. Source: the author.

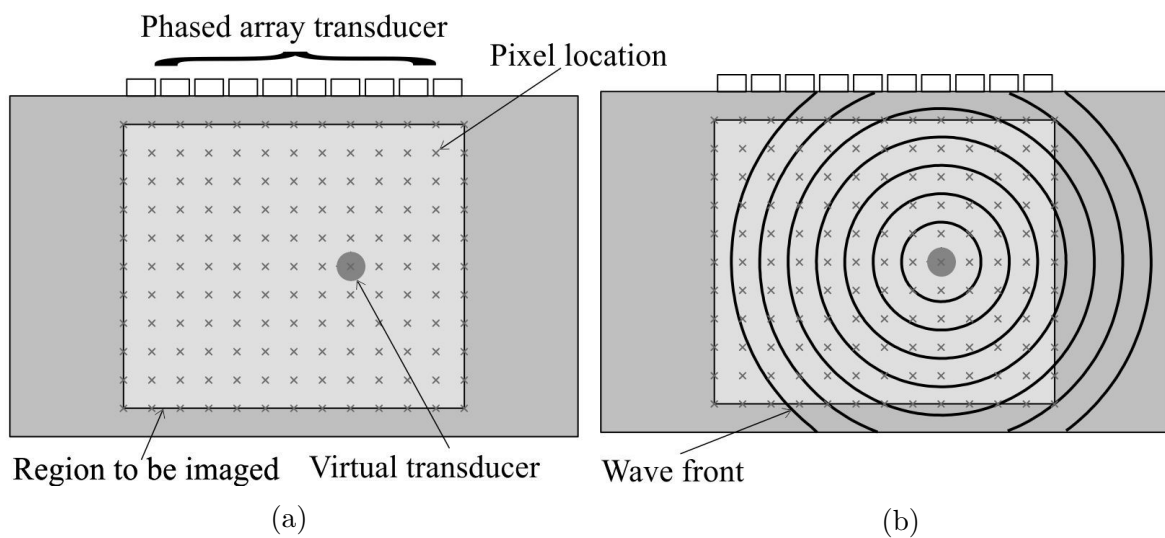


Figure 20 – Virtual transducer excitation. (a) Pixel position and (b) illustration of wave-front propagation. The outer boundary of the test piece is considered to absorb the incoming waves perfectly in this illustration. Source: the author.

As seen in Figure 20 the virtual transducer is circular and centred into the focusing point. The circular shape allows the excitation of omnidirectional waves. After the model is run once for every focusing point and the acoustic waves emanating from it are recorded with the phased array probe elements, it is possible to calculate the TOF via Equation 4.1.

$$TOF_{x,y,m,n} = t_{x,y,m} + t_{x,y,n} + \frac{d}{c_{avg}} \quad (4.1)$$

In Equation 4.1 d is the diameter of the circular virtual element placed centred at the focusing point; c_{avg} is the average sound speed velocity inside the material, considered to be 5700 m/s. Due to the resolution required of the final value of $TOF_{x,y,m,n}$ and the small diameter of the virtual transducer, it is possible to neglect and remove the last term from Equation 4.1. The terms $t_{x,y,m}$ and $t_{x,y,n}$ of this equation refers to the time taken for the wave to leave the boundary of the virtual transducer located at the focusing point in the coordinates (x, y) and to reach the transducer m and n in the phased array, respectively. The usage of the virtual transducer is possible because the path, and consequently the TOF, of the ultrasonic beam between two points is the same regardless the direction of the ultrasonic beam; i.e. the path of a beam leaving point A to reach point B is the same as if the beam leaves point B and reaches point A . The independence from the propagation direction on the TOF calculation was termed *principle of reciprocity* by Van Pamel et al. (64), who used it to improve the control over the scattering of a defect.

The simulated TOF can be used as delay laws for an FMC obtained experimentally, instead of being calculated with an equation such as Equations 3.33 or 3.34. Equation 3.32 than becomes Equation 4.2.

$$I_{TFM}(x, y) = \left| \sum_{m=1}^N \sum_{n=1}^N A_{m,n} (TOF_{x,y,m,n}) \right| \quad (4.2)$$

4.1.2 Single crystal

In order to the solve Christoffel Equation (Equation 3.1) or to model the propagation of acoustic waves in solid materials, one needs the mechanical stiffness matrix. Only on

rare occasions this is obtained by measurements. Usually, the mechanical stiffness matrix is obtained in the literature, which leads to discrepancies between the actual stiffness matrix and the data employed when direct measurements are not a viable option. The discrepancies can worsen if the stiffness matrix used is not from the same alloy. Nonetheless, it is common to find works where the stiffness matrix was obtained from previous studies on similar, but not the same alloy. References (3, 4, 8, 41, 64) are some examples of works which made use of stiffness matrices from literature instead of direct measurements.

Two main reasons explain why stiffness matrix measurements are rare; the first one is merely the difficulty in obtaining a suitable single crystal sample of the material where such parameters can be adequately assessed. The second reason is that, at least for Nickel based aerospace materials, there is a limited variation between the stiffness matrix of similar alloys, which can be verified by comparing the results obtained, for example, in references (8, 64–68). Nevertheless, there is an improvement on the accuracy of a model or data processing by assessing the stiffness matrix of a single crystal made of the same alloy as the test piece. Thereby, it is recommended to measure the stiffness matrix when possible in order to reduce the uncertainties in advanced ultrasonics inspection methods (4).

In this subsection, the methodology used in the study of a single crystal sample of the Nickel Alloy 182 is presented. A more complex measurement approach, such as those described by Castagnède et al. (69), Every and Sachse (70) and Barazanchy et al. (71), could not be employed due to the constraint imposed by the limited amount of material available. Therefore, an acoustic method, based on acoustic velocities measurements in specific directions, was used instead. The alloy used to grow the single crystal is often used as a filler material in overlay clads and weld joints of Nickel Alloy 600, austenitic stainless steel and low alloy steels (72). A particular application of this material is in nuclear power plants where it is used as cladding material (4, 73) and in dissimilar weld joints (72, 74). The weld block sample studied in this chapter and described in Subsection 4.1.3 comes from a dissimilar weld made using Alloy 182 as filler material, hence the justification to study the single crystal in this work.

4.1.2.1 Single crystal specimen description and experimental set-up

The single crystal sample was grown from GTAW consumable rods of Alloy 182 into a cylinder with the direction [001] parallel to the cylinder axis. Afterwards, the sample has undergone fine machining in order to produce a smooth surface resulting in a cylinder of 18.72 mm of diameter and 70 mm of length. In Figure 21 a picture of the single crystal before the machining is presented. The density of the single crystal sample was calculated from the mass and geometry of the sample. The results obtained rendered an average density equal to 8384 kg/m^3 with a standard deviation of 68 kg/m^3 .

After machining, a disc was cut from the cylinder in order to produce an appropriate sample to be assembled in an SEM (scanning electron microscope) to perform an EBSD (electron backscatter diffraction) analysis. The EBSD analysis objective was to confirm the success of the solidification process, i.e. to verify if it is, in fact, a single crystal orientated in the intended direction. In addition to the EBSD analysis, some SEM images were obtained to visualise the microstructure of the sample. Both the EBSD analysis and the SEM images were taken on one of the disc's planes, perpendicular to the cylinder axis.

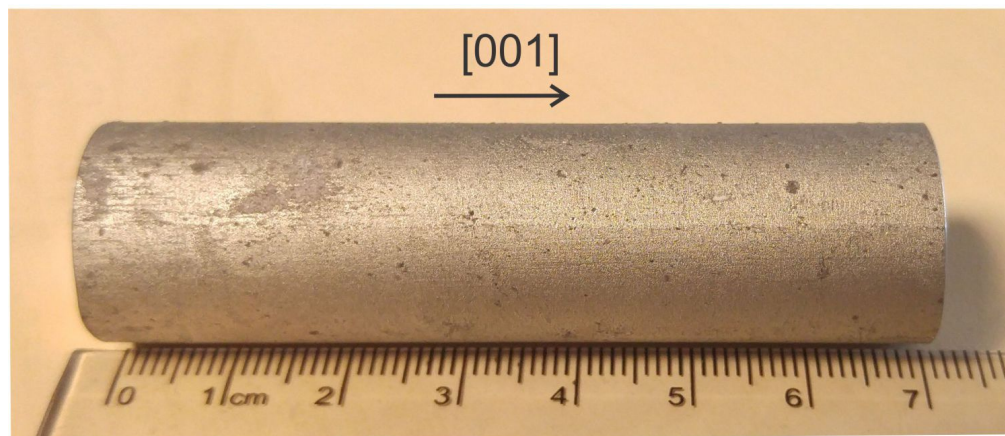


Figure 21 – Alloy 182 single crystal cylindrical sample used in this work before final machining. The arrow indicates the [001] direction throughout which the crystal grew. Source: the author.

Figure 22 displays the pole figures obtained with the EBSD analysis in three families of planes, namely the families $\{100\}$, $\{110\}$ and $\{111\}$. Those pole figures, obtained from a grid of measurement points that encompasses most of the disc's surface, confirms that

the sample is a single crystal with the family of directions $\langle 100 \rangle$ closely orientated to the cylinder axis.

An SEM image is shown in Figure 23, where one can identify the presence of multiple dendrites growing perpendicular to the image plane and parallel to the cylinder axis. In this figure, it is possible to notice that the arms of the dendrites have the same orientation. This microstructure suggests that the multiple dendrites grew within a constricted direction dispersion range, which is in accordance with the EBSD data. According to Wang et al. (74), some elements can highly segregate during the single crystal solidification process, which can impair the material's properties. This segregation can be visualised in Figure 23 on the region around the boundaries of adjacent dendrite arms by a whiter shade. However, since the proposal of this single crystal sample is to study its stiffness matrix and the fact that this alloy was not designed to be used in single crystal parts, possible performance problems are not a concern in this work.

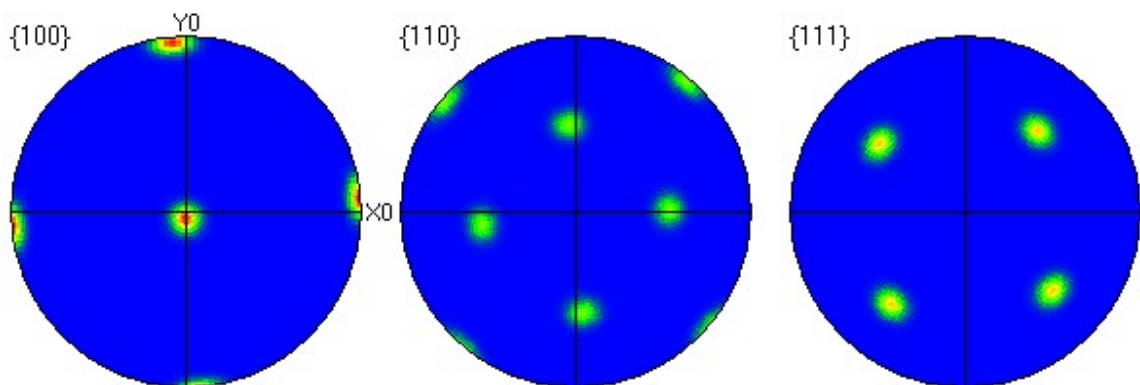


Figure 22 – Pole figures of the single crystal obtained via EBSD indicating that the material is a cubic single crystal. The results are presented with three pole figures for the $\{100\}$, $\{110\}$ and $\{111\}$ family of crystallographic planes. Source: the author.

4.1.2.2 Acoustic wave propagation simulation

In order to create an understanding about the behaviour of acoustic waves travelling inside the single crystal sample a 2D model in the semi-analytical software platform CIVA was created. The model encompasses the (001) plane of the single crystal and uses a single element probe with a diameter of 10 mm positioned 20 mm away of the single crystal

lateral surface, or 29.36 mm away from the specimen centre. Water was used as a coupling medium between the transducer and the test piece. Figure 24 presents the geometry of the model. Notice that the axis of the transducer is aligned with the centre of the single crystal.

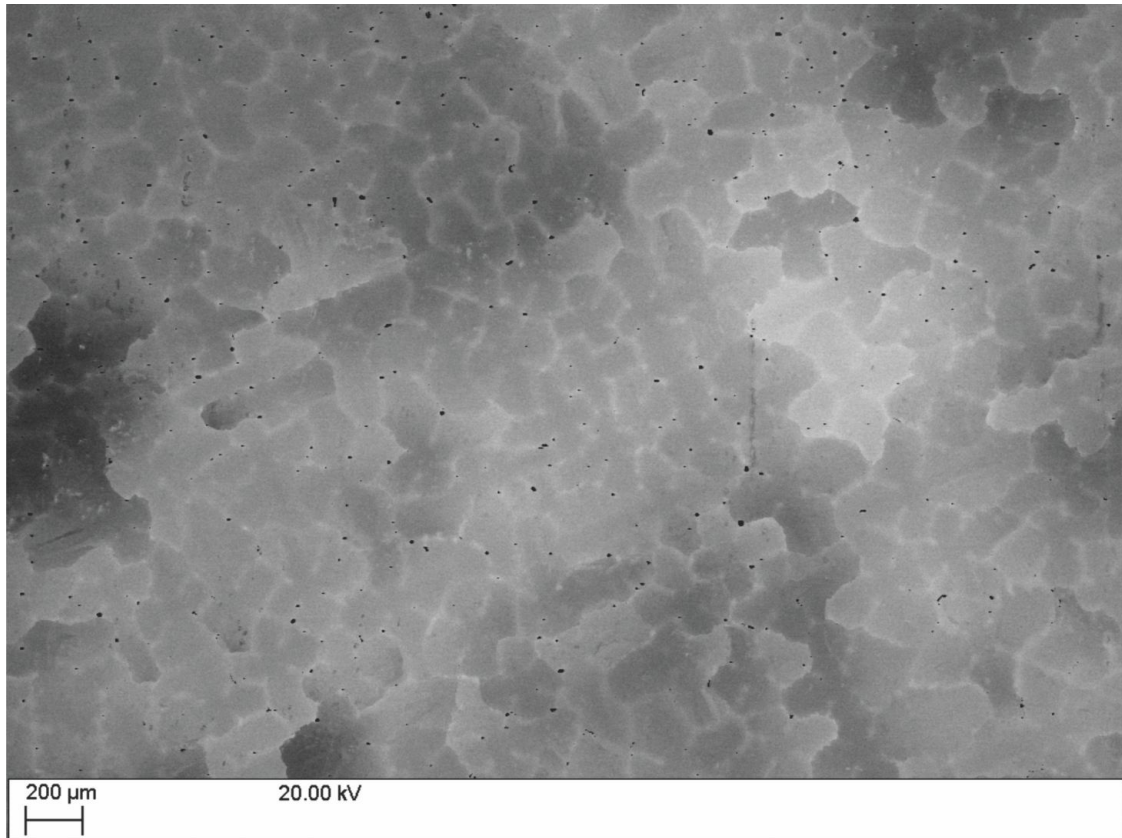


Figure 23 – Scanning electron microscopy of the single crystal. The plus sign structures are cross-sections of individual dendrites with the main growth direction perpendicular to the picture’s plane. Source: the author.

Firstly, the single crystal orientation was set in such a way that the $[100]$ direction was pointed towards the transducer; then the transducer was excited with a Gaussian tone burst with 10 MHz^2 as the central frequency. The sampling frequency was adjusted to 50 MHz. During the simulation, enough travel time was granted for the tone burst to propagate up to the opposite side of the single crystal and reflect all the way back to the transducer. Meanwhile, the signals coming back to the transducer were recorded. Figure 25a presents the signal received back in the transducer as an A-scan.

²Since the TOF is not a function of the transducer frequency and the objective of this simulation is not to model the attenuation or any other quantity influenced by the frequency, the simulation was run only with one of the frequencies used in the experiments.

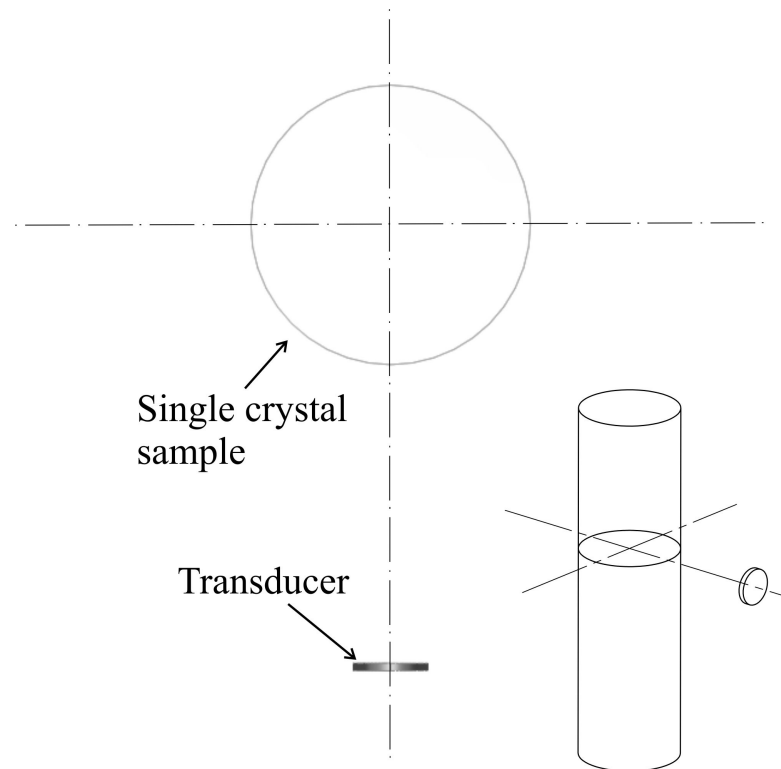
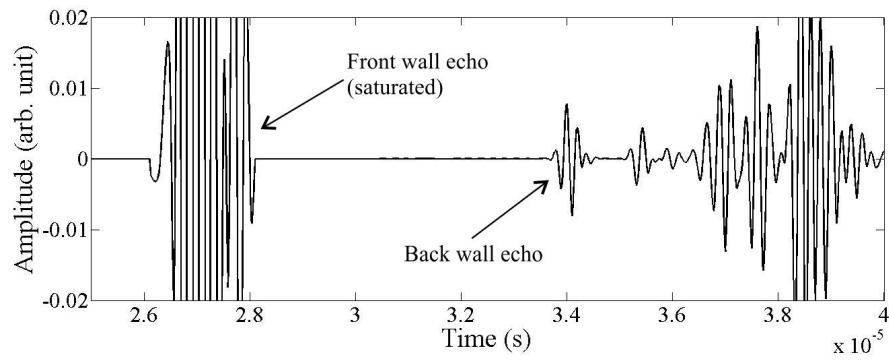
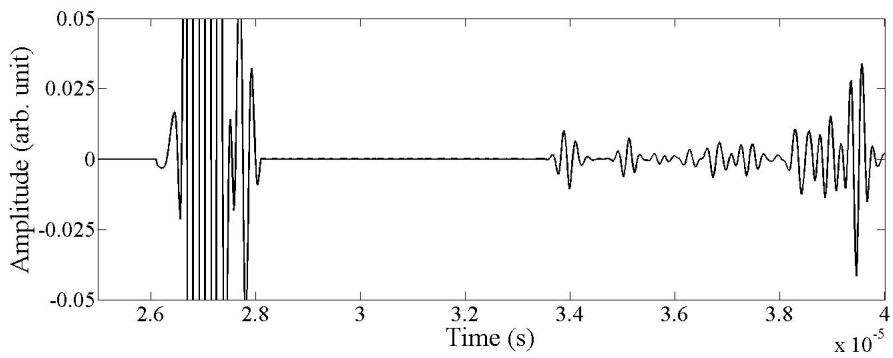


Figure 24 – Top view showing the geometry of the simulation run in CIV4. The transducer is aligned with the centre of the single crystal, and the set up is immersed in water. On the bottom left, there is a 3D representation of the geometry. Source: the author.

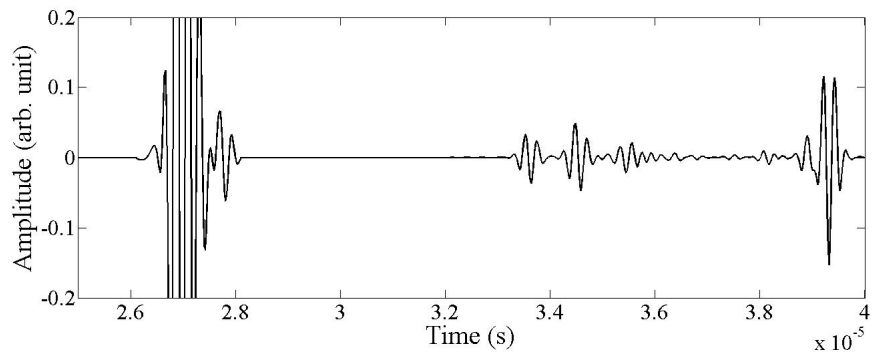
With the intent to evaluate the behaviour of acoustic waves for other orientations of the single crystal, the model was run in batch mode. The batch mode consisted of varying the crystallographic orientation facing the transducer, in the plane (001), from the [100] direction, by a 5° step up to 45° , which is equivalent to say that the [110] direction was facing the transducer. Due to the symmetry of cubic crystals, there is no need to carry the simulation any further. Figures 25b, 25c and 25d present the A-scans for 15° , 30° and 45° rotation angles, respectively. The A-scans for the other directions are not present for the sake of brevity.



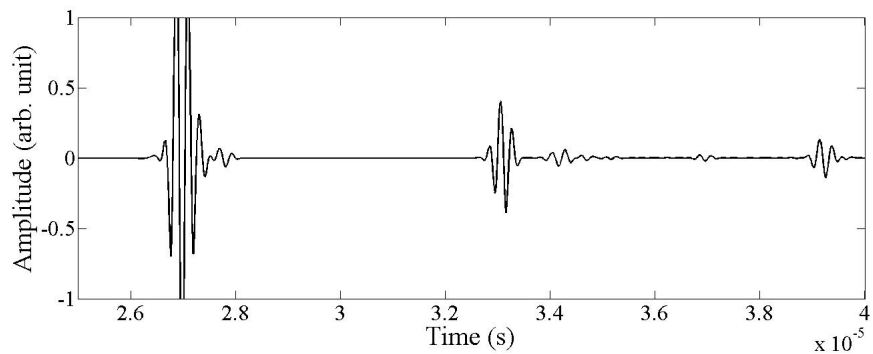
(a) [100].



(b) 15° rotation from the orientation in (a).



(c) 30° rotation from the orientation in (a).



(d) 45° rotation from the orientation in (a) or direction [110].

Figure 25 – A-scans simulation results for the [100] direction facing the transducer (a) and in-plane rotations of 15° (b), 30° (c) and 45° (d) from the orientation in (a). The last one corresponds to the [110] direction facing the transducer. Source: the author.

By analysing the images in Figure 25, it is possible to notice a back wall reflection in all figures between 33 and 34 μs . Figure 26 complements Figure 25, in the former the ray paths capable of reaching back the transducer for the four incidence angles are presented. It is possible to notice in Figure 26 that only for 0° and 45° rays are reaching back the transducer without changing its direction inside the material. Those angles correspond respectively to the $[100]$ and $[110]$ crystallographic directions. Since the back wall reflections present in Figures 25b and 25c do not occur at a right angle to the surface and the propagation direction is tilted, they must be neglected. This behaviour is in accordance with what was observed by Juva and Lenkkeri (75) due to the acoustic beam skewing. The reason why this happens lies in the slowness curve of cubic crystals. In Figure 2 one can notice that, for the longitudinal mode, the only crystallographic directions where the acoustic beam is perpendicular to the slowness curve is for the $[100]$ and $[110]$ directions.

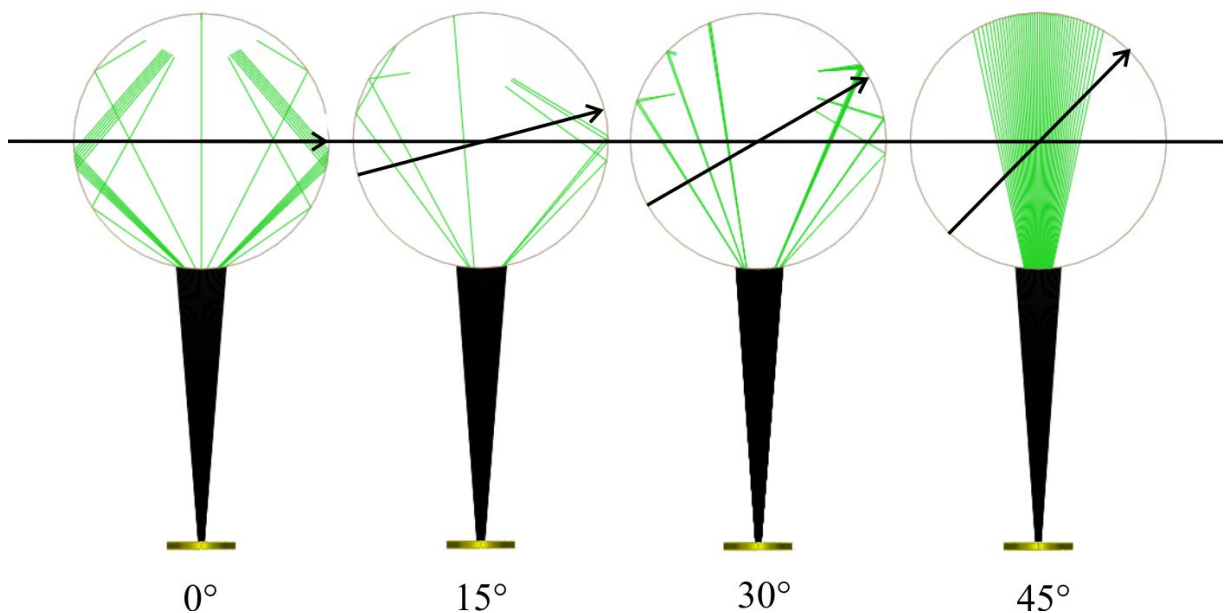


Figure 26 – Ray paths able to enter the single crystal and come back to the transducer for four crystallographic orientations facing the probe. The black cone represents the incident beam, while the green lines represent the refracted rays. The arrows are in the direction $[100]$, and the angles between them and the horizontal line are indicated at the bottom of each image. Source: the author.

It is possible to notice in Figures 25a and 25d the considerable amplitude discordance of the back wall reflection between the $[100]$ and $[110]$ directions. This discrepancy was

observed by Juva and Lenkkeri (75) when studying a spherical austenitic stainless steel single crystal and was attributed by them to the curvature of the slowness curve around those crystallographic directions. For cubic crystals, in the $\{100\}$ planes, the slowness curvature is considerably weaker around the $\langle 110 \rangle$ directions than around the $\langle 100 \rangle$ directions, this can be visualised in Figure 2. For a weaker curvature, the acoustic beam deviates less than for a stronger curvature, therefore, the amplitude of the back wall reflection when one of the $\langle 110 \rangle$ directions is facing the transducer is higher than the amplitude when one of the $\langle 100 \rangle$ directions is facing the transducer. Figure 26 illustrates the effect of the curvature of the slowness curve on the signal amplitude. For the first case, it is noticeable that only the signal reaching the sample's surface at a constricted range around 90° is capable of reaching the back wall and travel back to the transducer. Meanwhile, for the second case, where an $\langle 110 \rangle$ direction is facing the transducer, the incidence angle range is considerably broader.

4.1.2.3 Mechanical properties computation procedure

From the insight obtained with the acoustic wave propagation simulation, it was possible to design an experimental procedure to assess the mechanical stiffness matrix of the single crystal sample. Due to the symmetry of the cubic crystal, its stiffness matrix has only three independent elements, namely C_{11} , C_{12} and C_{44} . So, by solving three of the Equations 3.6 to 3.11, it is possible to obtain these stiffness matrix elements and define the stiffness matrix. Due to the single crystal sample geometry, the equations chosen were Equation 3.6, 3.7 and 3.9.

Two methods were employed to measure those velocities. The first one was used to measure the velocities of the modes capable of propagating along the axis of the sample or direction $[001]$, which were the $V_{S1[001]}$ and $V_{L[001]}$ velocities. The second method measured the velocity of the longitudinal mode on the planes $\{001\}$. The time of flight on both methods was obtained by carefully measuring the appropriate peak position in the A-scans using the gate function of the equipment. As discussed in Section 4.1.2.2, due to the way the ultrasonic beam propagates in these planes the only directions where it was possible

to measure the velocities were on the directions belonging to the families $\langle 100 \rangle$ and $\langle 110 \rangle$ present in them. Those velocities are the $V_{L\langle 100 \rangle}$ and $V_{L\langle 110 \rangle}$.

$V_{S1[001]}$ and $V_{L[001]}$ were measured using a 0° shear wave probe and a longitudinal wave probe, respectively, directly coupled in one of the extremities of the sample which produced a beam travelling through the axis of the sample. This configuration allowed time of flight measurements to be taken in the axial direction, which coincides with the $[001]$ crystallographic direction. In Figure 27 an illustration of this set-up is presented. From the time of flight values and the length of the cylindrical sample, it was possible to calculate the transversal ultrasonic wave propagation velocity, $V_{S1[001]}$, and the longitudinal ultrasonic wave velocity, $V_{L[001]}$. The later can be compared with $V_{L\langle 100 \rangle}$ obtained via the measurement method detailed later in this section.

Due to the symmetry of cubic crystals and the invariance of the first transversal mode of cubic crystals in the $\{100\}$ family of planes, it is possible to state that $V_{S1[001]} = V_{S1\{100\}}$. Since both transversal wave modes have the same slowness in the $\langle 100 \rangle$ directions, it is also possible to state that $V_{S1[001]} = V_{S2\langle 100 \rangle}$. Similarly, for the transversal waves, it can be attested that $V_{L[001]} = V_{L\langle 100 \rangle}$. These initial measurements allowed the solution of Equations 3.6 and 3.7 for their respective stiffness matrix elements. However, since $V_{S1\{100\}}$ and $V_{L\langle 100 \rangle}$ are only measured on the axis of the specimen the relevance of the measurements is impaired. This problem is solved for $V_{L\langle 100 \rangle}$ with the immersion experiment; however, since it is not possible to propagate shear waves in water, $V_{S1\{100\}}$ measurements could not be improved.

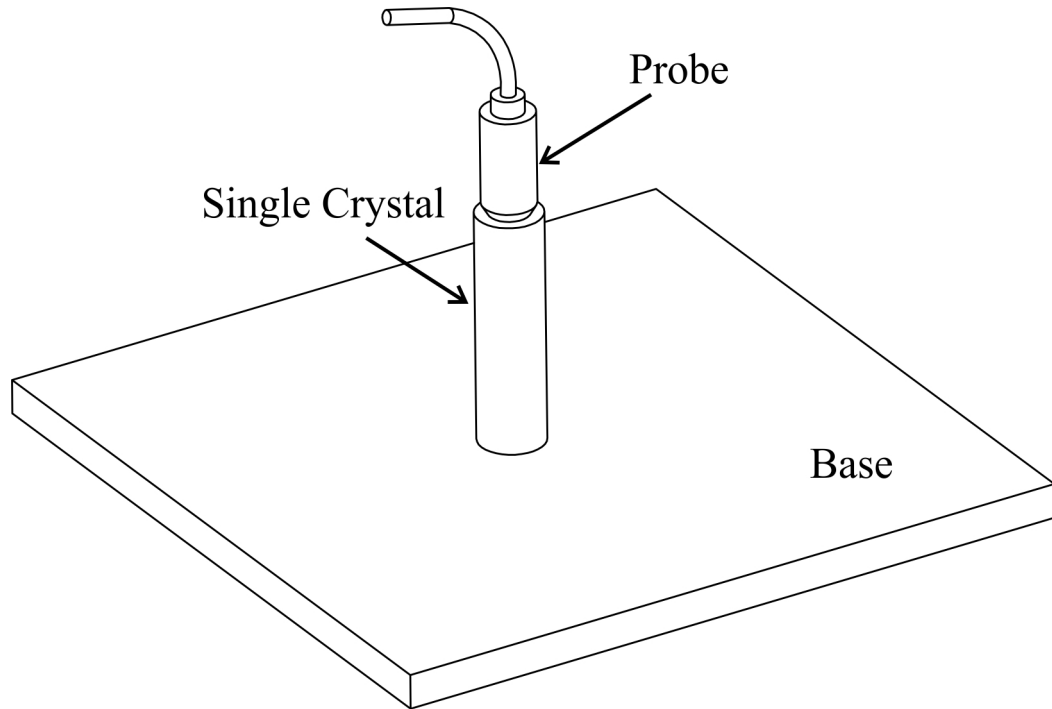


Figure 27 – Schematic drawing of the experimental set-up used to measure the ultrasonic velocities on the axial directions of the single crystal. Source: the author.

After the measurements described above, the determination of $V_{L\langle 100 \rangle}$ and $V_{L\langle 110 \rangle}$ took place using a method that mimics the simulation run in CIVA, described in Section 4.1.2.2. Figure 28 illustrates the assemblage used for these measurements, which consist in the single crystal being attached to a turntable using a specially designed fixture to assure its correct positioning. Also, the probe was fixed radially, aiming towards the single crystal centre in a plane parallel to the (001) plane and 20 mm away of the sample's surface. The measurements were conducted with the set-up immersed on water at 22°C using two longitudinal wave probes, one at a time, where one of them operated at 10 MHz and the other one at 15 MHz. The orientation of the single crystal regarding the probe was adjusted by rotating the turn-table and observing the back wall echo position. Following that, time of flight measurements were conducted in the four members of the families of directions $\langle 100 \rangle$ and $\langle 110 \rangle$ present in the plane at which the specimen rotated (plane (001)). After the eight time of flights were acquired the probe was axially moved, regarding the axis of the sample, in order to acquire the same time of flights, but on a different plane. This procedure was repeated on a third plane in order to improve the statistical significance of the experiment.

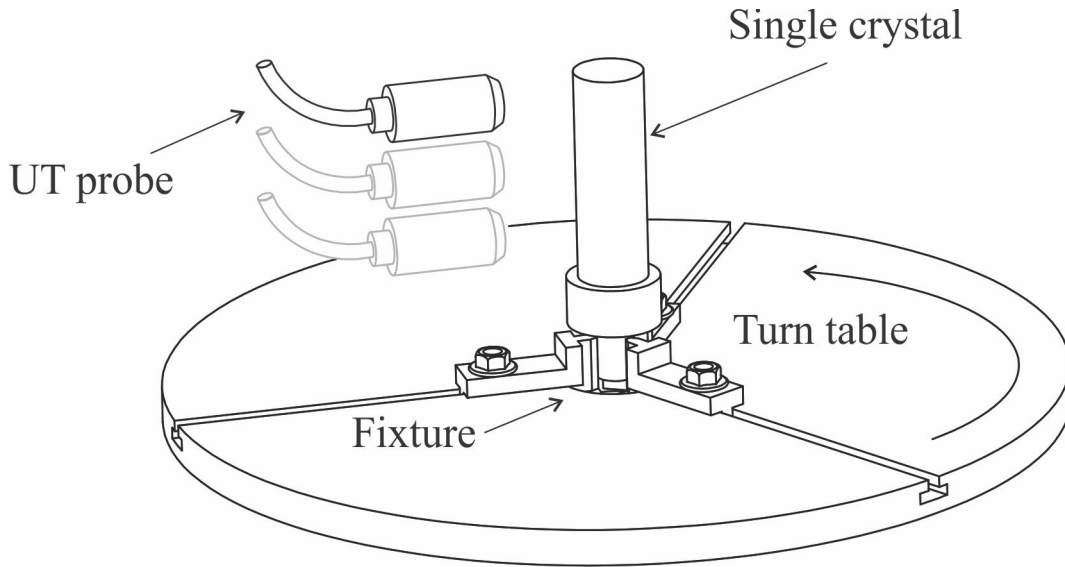


Figure 28 – Schematic drawing of the experimental set-up used to measure the ultrasonic velocities on radial directions of the single crystal. The top probe position is illustrated by the dark line probe sketch, while the other two positions are represented by the dim probe sketches. Source: the author.

The two velocities measured with the immersion set up, $V_{L\langle 100 \rangle}$ and $V_{L\langle 110 \rangle}$, were composed by twelve measurements each. Those measurements were composed by three for each of the four orientations in three different planes. Taking into account the measurements obtained with the contact probe, $V_{L\langle 100 \rangle}$ was measured in all the possible directions, in contrast with $V_{L\langle 110 \rangle}$ that was only measured in the three planes parallel to (100). Like the $V_{S1\{100\}}$ measurements, the results of $V_{L\langle 110 \rangle}$ were impaired by not measuring this velocity in all possible orientations. However, such impairment is much less significant than for the shear wave case since these velocity measurements were taken in twelve positions around the sample. The determination of the $V_{L\langle 100 \rangle}$ in the plane (100) together with its contact probe measurements allows one to solve Equation 3.7 for C_{11} with greater precision. While the measurements of $V_{L\langle 110 \rangle}$ on the plane (100) allow the evaluation of Equation 3.9.

4.1.3 Description of the test sample

The test sample used in this chapter is a weld block with five machined side-drilled holes mainly composed of the Nickel Alloy 182; Figure 29 shows a picture of this test piece. The weld block is a part of a dissimilar weld joint between a 316L stainless steel plate

and a 50D carbon steel plate. The later was clad with 309L/308L stainless steel and the joint was created to represent the weld joint used in the nozzle safe-end transition of nuclear power plants to connect the nuclear pressure vessel with its primary cooling circuit (4).

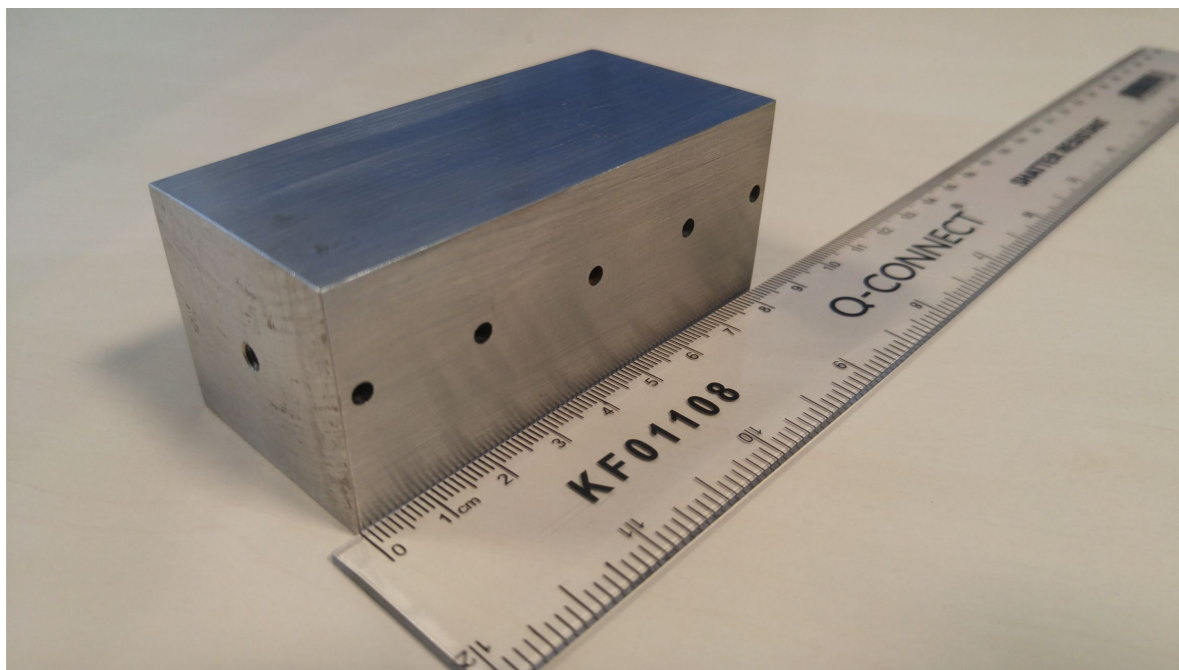


Figure 29 – Dissimilar weld block used for this chapter. Its dimensions are 83.5 mm x 35 mm x 40 mm. The five side-drilled holes aligned on one of the block's side have a diameter equals to 3 mm and were bored all the way through the block. On another surface one can see an additional hole; however, this hole is shallow and does not influence this study. Source: the author.

In Figure 30 a schematic view of the dissimilar joint and the approximate position from where the block was extracted are presented. This figure was created based on those presented in (4,5). According to Figure 30, the carbon steel side of the joint was buttered with Nickel Alloy 182 weld filler beforehand. Following the buttering, the two plates were joined together with GTAW and SMAW weld process also using Nickel Alloy 182 as weld filler material. The first weld process was used only for the root pass, while SMAW was used for all the remaining passes. Further details about the welding procedure involved in the construction of this joint can be found in (4).

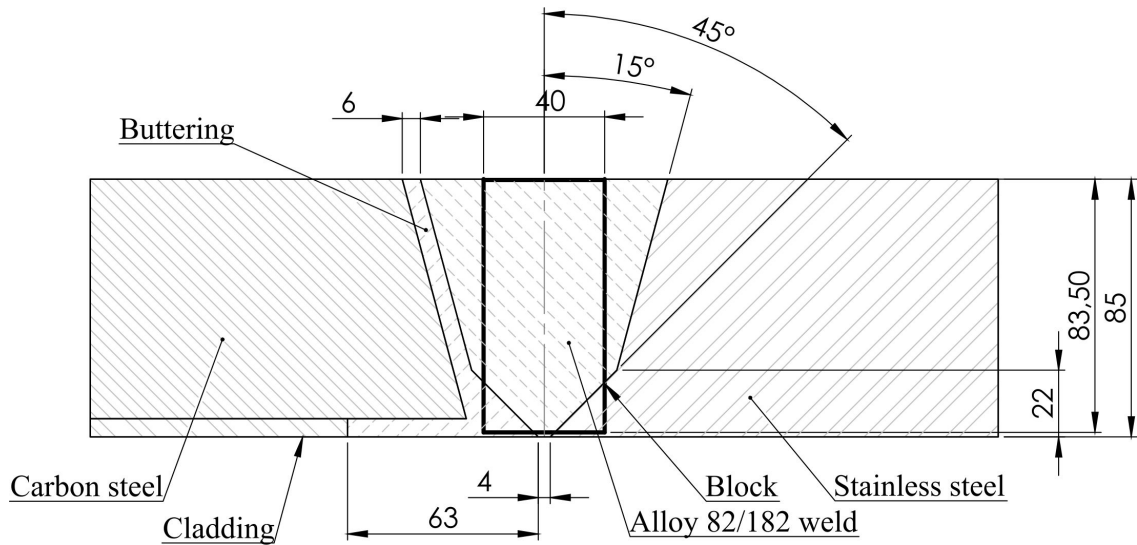


Figure 30 – Schematic representation of the weld sample from which the block was extracted. The rectangle in the middle of the weld represents the position from where the block was extracted. Adapted from (4) and (5). Dimensions are in millimetres. Adapted from Dissimilar project report (4).

The weld block was mapped via EBSD in order to obtain the crystallographic orientation of its grains. It was pointed out in (4) that the map describing the weld grain structure and orientation needs to be fine enough to capture significant scatterers. However, due to the high cost involved in an EBSD analysis over a large area, it is important to use a step size as large as possible. The upper limit for the step size was determined by considering that, for ultrasonic waves, significant scattering loss starts to take place when the scatterer is at least one-tenth of the wavelength (4,17). With this rule and considering a 1.5 MHz probe generating a wave with a wavelength of approximately 3.8 mm, a 40 μm grid size, rendering almost 10 measurement points for the smallest significant scatterer, it was considered to be enough to resolve any meaningful detail and was defined as the grid step size for the EBSD analysis.

The availability of the EBSD results and its successful use as a description of the crystallographic orientation of the block in previous works (4,5) were considered to be valid justifications for its use in the present work. Nonetheless, when considering the use of a 2.25 MHz probe, which was the probe frequency used here and described in more detail along this chapter, the wavelength becomes approximately 2.7 mm for an average wave velocity of 5700 m/s. This smaller wavelength raises concern about the resolution of

the EBSD map because the equivalent minimum scatterer for this wavelength would be 0.27 mm, which renders less than seven EBSD points for the smallest significant scatterer. However, as it will be demonstrated throughout this thesis, this resolution reduction in the EBSD map can be considered to be acceptable to model the pathway taken by the ultrasonic waves. Figure 31 presents the EBSD map used in this chapter; the colours represent the crystallographic orientations exposed on Table 1. The angles α , β and γ are the rotation angles introduced in Section 3.2.2, where the rotation matrices were described. Further considerations about the EBSD measurements and data processing are available at Appendix A.

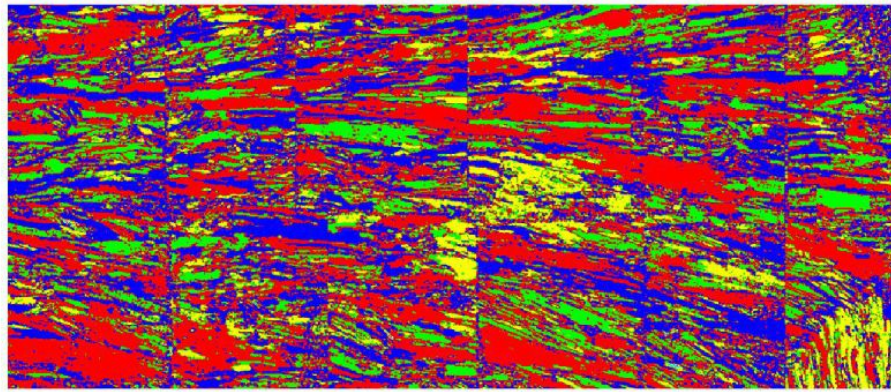


Figure 31 – EBSD map used to represent the crystallographic orientations of the block. Adapted from Dissimilar project report (4).

Table 1 – Color key for the grain orientations presented in Figure 31

| Colour | α (°) | β (°) | γ (°) |
|---------|--------------|-------------|--------------|
| Red | 0 | 0 | 0 |
| Green | 352.3 | 176.1 | 195.4 |
| Yellow | 255.8 | 331.5 | 4.9 |
| Blue | 272.2 | 355.3 | 43.7 |
| Cyan | 322.3 | 5.1 | 6.0 |
| Magenta | 326.0 | 200.5 | 221.0 |

For comparison, Figure 32 presents a macrograph of the joint, where it is possible to identify the passes of buttering and weld. However, this macrograph does not come

from the block, but from a different position on the same dissimilar weld. Nonetheless, the lengthwise uniformity of the weld was previously investigated rendering the conclusion that it can be considered to be uniform from the ultrasonics point of view (4).³

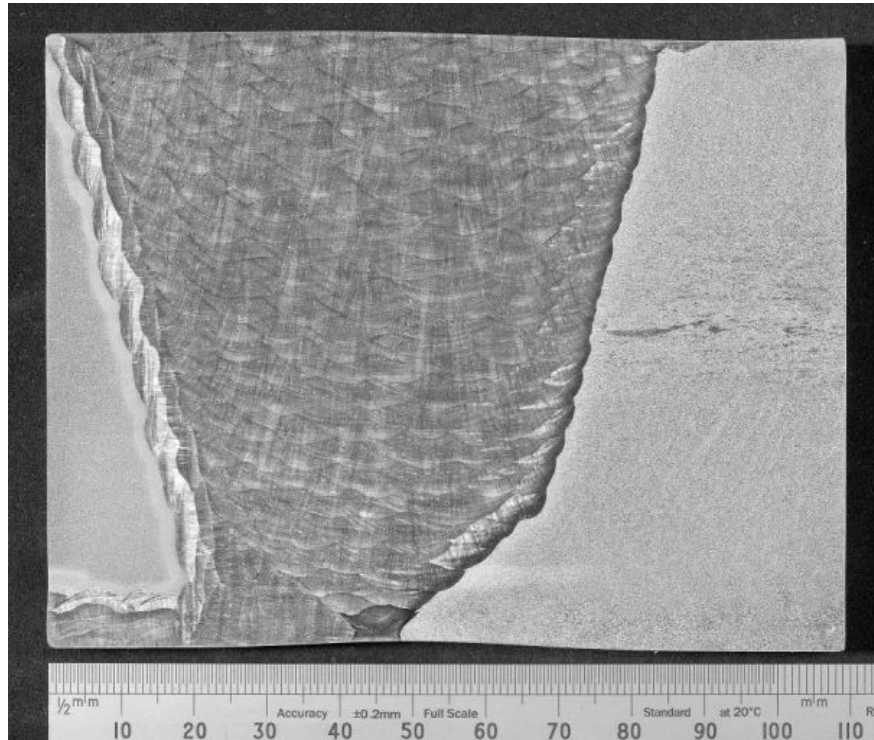


Figure 32 – Macrograph of the original weld cross-section which originated the testing block. Image courtesy of TWI.

4.1.4 Experimental methodology

The acquisition of the experimental FMC was performed in an immersion tank equipped with an automated manipulation arm used to position a phased array transducer containing 32 piezoelectric elements with a central frequency of 2.25 MHz. Figure 33 presents a photograph showing the set-up. The pitch of the transducer was equal to 0.75 mm and the elevation of the elements was 12 mm. To feed the transducer and collect the FMC data an M2M MultiX++ phased array system controlled by the M2M Multi 2000 software was used. Since the side-drilled holes are 15 mm below the front wall, a gain of 62 dB on the A-scans to balance the high attenuation of the block needed to be applied.

³For the lengthwise uniformity analysis a 1 MHz probe was employed. However, because only the block was available, which is a small fraction of the welded plate, the uniformity analysis could not be repeated with the higher frequency probe used in this work.

Unavoidably, the A-scans become saturated around the front wall due to such a high gain. Nonetheless, since the front wall is not a concern in this work, the signal saturation around it is not an issue.

The position of the probe regarding the block is of paramount importance in order to match the simulation results with the experimental data. The correct position of the block was assured by correctly mapping the block position with the phased array probe via the 6 dB rule (76) using the immersion tank's automated manipulator. As illustrated by Figure 34, the 6 dB rule states that if a transducer, initially positioned parallel and above a surface, represented by the right transducer and A-scan, is gradually moved outside this surface the amplitude of the surface's reflection drops. When half of the beam is outside the surface and half still above it, as the central image in Figure 34 shows, the amplitude drop is equal to half the original amplitude, which is the same as a 6 dB drop. Further moving the transducer out of the sample decreases the A-scan amplitude even more, until no signal from the front wall is present in the A-scan. This last position can be visualised in the left part of the figure ⁴.

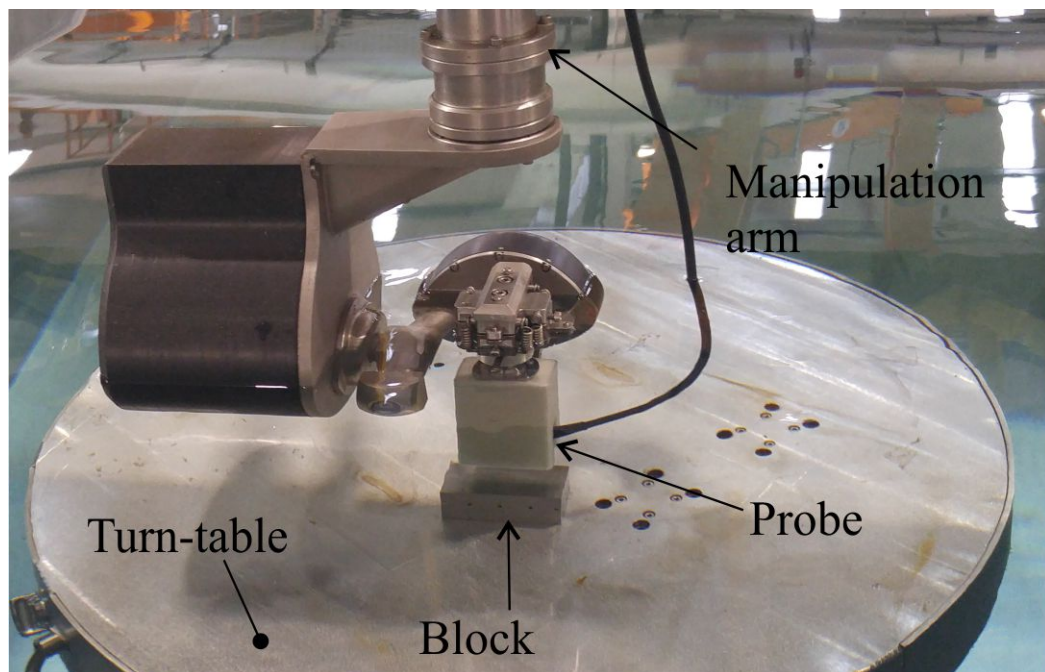


Figure 33 – Photograph showing the set-up used to collect the experimental data from the block underwater in the immersion tank. Source: the author.

⁴Diffraction effects at the edge of the block did not affect the amplitude of the signal significantly and were not taken into account.

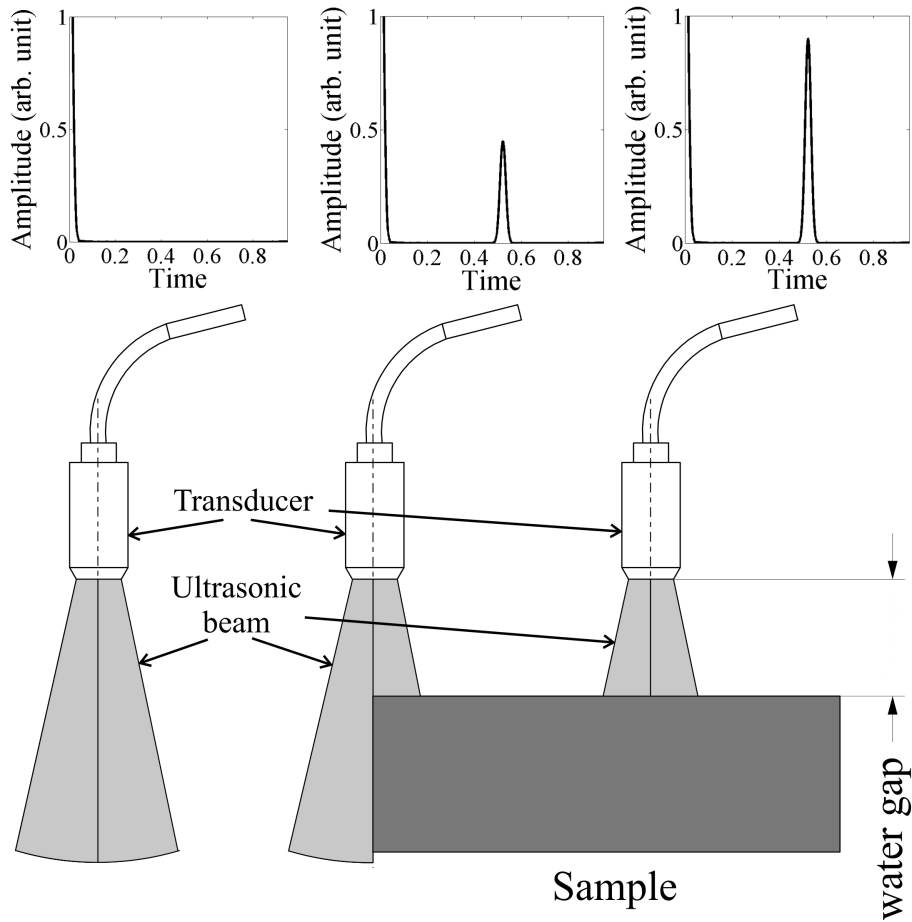


Figure 34 – Illustration of the 6 dB rule using a single element transducer. The squares on the top of the figure represent what the A-scan would look like for their respective probe positions. Source: the author.

The block position mapping was carried out by applying the 6 dB rule on several regions of the block using the element of the phased array probe employed for the FMC data acquisition previously described. Two measurements were carried out on each broadside plus one measurement on each of the remaining two sides. Figure 35 illustrates the general set-up of those measurements, where a top view of the block with each measurement position indicated by an out-of-scale representation of a piezoelectric element.

The FMC acquisition was carried out with the centre of the 32 elements arranged in the middle of the test block. Data for two additional parallel inspection planes were obtained to verify the reproducibility of the method. The measurement planes are also illustrated in Figure 35. The acquired data were exported by Multi 2000 in .txt files, which were fed to a Matlab algorithm and combined with the simulated TOF.

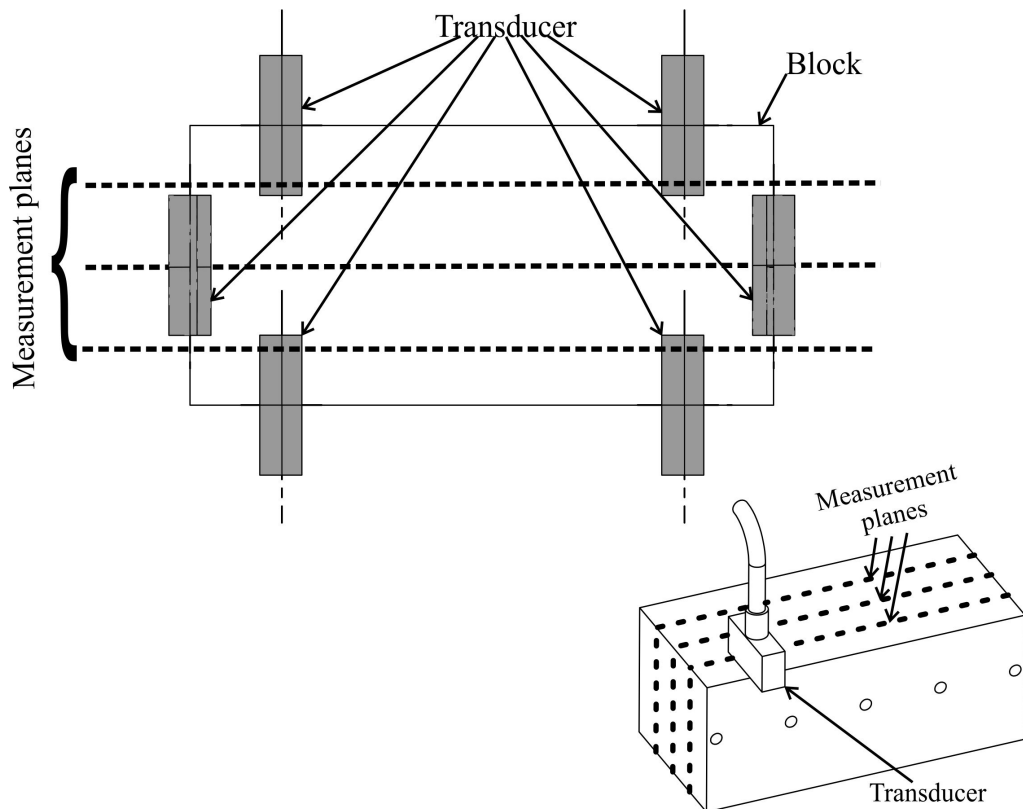


Figure 35 – Illustration of the block position mapping. The grey rectangles on the top image represent the piezoelectric transducer in its several positions throughout the block. On the bottom right corner, there is an image of the block in perspective with the transducer positioned on one of the positioning points. On both of the images, the measurement planes, at which the FMC's were collected, are also indicated. Source: the author.

4.1.5 Simulation methodology

The finite element modelling involving the block was carried out in PZFlex, which is a finite element software package capable of running time domain acoustic models with structured mesh. The results obtained by the simulations described in this subsection were later analysed and post-processed in Matlab by algorithms written for this purpose. Besides the possibility to employ 3D models in PZFlex, a 2D geometry was chosen due to the significant reduction in the solution time. However, as Limthongkul (5) states in his dissertation, 2D models have problems in correctly representing the acoustic wave propagation due to the unrealistic 2D stress condition assumption. Despite this drawback, results indicate that the accuracy of the model can be considered suitable to simulate the TOF of the weld block.

The model encompasses the central region of the block with 40 mm in the direction of the front wall and the total height of the block, which is equal to 35 mm. A 15 mm water gap separates the phased array from the sample. The same transducer characteristics as the experimental phased array probe, described at Section 4.1.4, were used in the simulation in order to match both the experimental and simulation results. The structured mesh used had approximately 2.9×10^6 nodes in two regions, one for the water layer and the other for the block, with different mesh sizes. The first had a mesh size equivalent to one-thirtieth of the wavelength of the sound wave in water (1483 m/s), while the second used a mesh size equal to one-thirtieth of the longitudinal sound wave wavelength for an isotropic homogeneous material with its longitudinal wave velocity equal to 5700 m/s. In Figure 36 the model geometry without the central side-drilled hole is presented.

The grid where the virtual probe was positioned, which later becomes the pixels of the final image, was defined as 33 horizontal points by 51 vertical points, with a step between adjacent points equal to 0.5 mm. The grid was horizontally centred in the block with its uppermost boundary 5 mm below the front wall. The rectangle, which defines the outer boundaries of the grid inserted in the model, is also displayed in Figure 36.

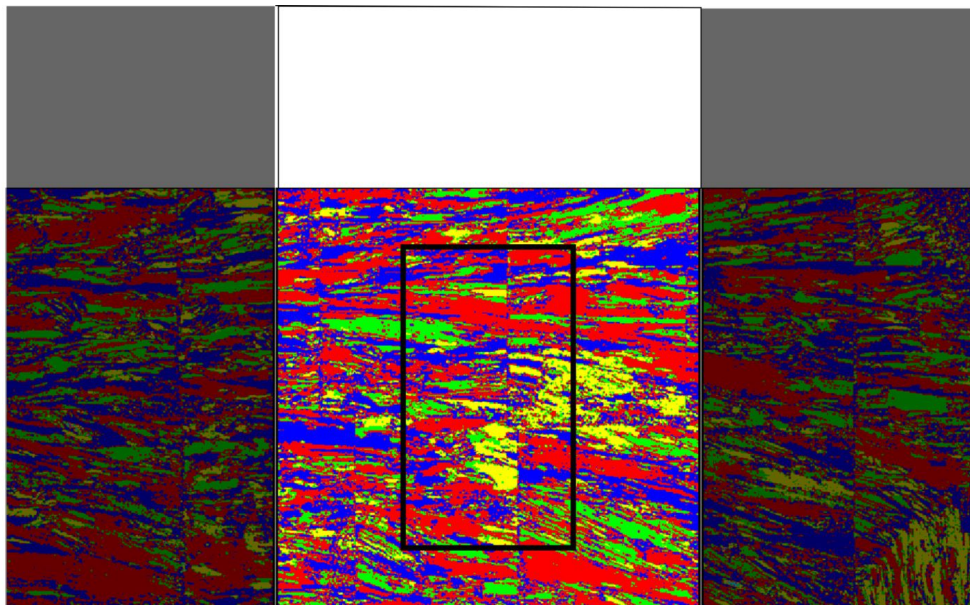


Figure 36 – Weld block with the modelled region highlighted. The white rectangle on top is the water layer and the imaged region is represented by the rectangle in the centre of the EBSD map. Source: the author.

The phased array probe was modelled by a set of 32 transducers on the uppermost boundary of the model, set to collect the acoustic vibrations arriving at them. On the other hand, the virtual probe was defined by a circle with a diameter of 0.2 mm, whose inner area was defined as a vacuum to force the sound waves to propagate exclusively outside the transducer and avoid problems related to reflection and reverberation inside it. The virtual transducer was excited with a linear prescribed pressure load defined by a Gaussian tone burst with a central frequency of 2.25 kHz. A representation of this tone burst is presented in Figure 37. The time needed to run this simulation strongly depends on the computational resources used, but it should be between 10^1 and 10^2 h order of magnitude.

The acquisition of an FMC was also simulated in order to create a simulated TFM image for comparison with the experimental one. For this task, in addition to the detection of acoustic waves, the phased array transducers also excited the model. Similarly to the virtual probe, the phased array transducers, in this case, were excited with the linear prescribed pressure load presented in Figure 37. The stiffness constants used to model the mechanical behaviour of the test block were the ones obtained from the single crystal measurements and presented in Chapter 5.

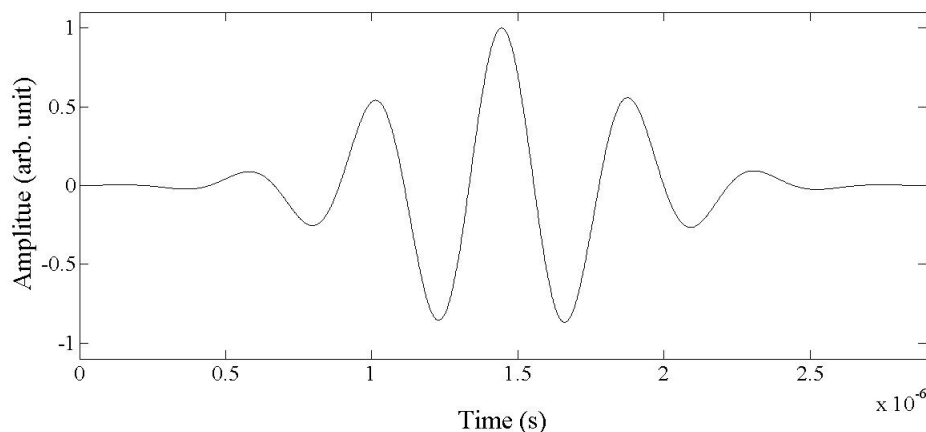


Figure 37 – Tone burst used to excite both the phased array and virtual transducers in the weld block simulations. Source: the author.

4.2 Coherence weights

As stated before in this thesis, austenitic welds can impair ultrasonic inspection significantly (4,6,46). Mechanically lined pipes, whose girth weld and the cladding around it have this microstructure, are subjected to this problem. In this chapter, a study focused on the investigation of data processing techniques, termed *coherence weights*, on the inspection of the triple joint present between the cladding, liner and external pipe via FMC/TFM is presented. This region is of great importance when the integrity of lined pipes is a concern. Those techniques aim to reduce the influence of phase aberration after focusing the beam. Coherence weights have been demonstrated to improve the quality of ultrasonic images on several occasions. Some of them are presented in references (54–56,59–61,77).

4.2.1 Mechanically lined pipes

A mechanically lined pipe is an assemblage compound of an external Carbon-Manganese steel alloy pipe and an internal corrosion resistant alloy pipe. The pipes are assembled by radially expanding the liner, which can be done via hydro-forming or mechanical tools (78,79); this process plastically deforms the inner pipe and, in some cases, the outer pipe as well (78) assuring an interference fitting between both parts. The terminations of the lined pipes are usually machined to remove the liner and then it receives a seal weld followed by an overlay clad covering the exposed inner surface of the external pipe (7,78). The length of the overlay portion is set to be long enough to allow repair in the joint and make the inspection of the region easier (78). Sections of pipes are usually joined by a girth weld employing a filler material made of a corrosion resistance alloy, which matches with both the liner and overlay clad portion. Figure 38 shows a schematic drawing of the geometry of lined pipes girth weld region.

Due to their manufacture characteristics, mechanically lined pipes have been considered to be an economical alternative to metallurgic bonded clad, or clad pipes (78,80). They are usually used on the transportation of corrosive multiphase fluids to and from onshore and offshore oil & gas well heads (80). Besides their economic benefits, those pipes are known to present good fatigue performance (81) and high-temperature tolerance

(80,81). Despite their advantages, lined pipes can suffer from liner buckling and are not entirely immune to fatigue cracking during their transport to the installation site or while being used as catenary raisers (7,78,80,81).

The girth weld is where the concerns about fatigue are mainly concentrated. There are four main stress concentration locations where a fatigue crack is more likely to nucleate (81). Those locations are indicated in Figure 38 by the numbers 1 to 4. The focus of this chapter is upon the regions 1 and 2, where the liner, overlay clad and external pipe meet. Those regions, especially region 1, are sources of uncertainties regarding the fatigue behaviour of girth welded mechanically lined pipes (7). In the work described by Johnston et al. (7) roughly two-thirds of the lined pipes specimens subjected to fatigue resonance tests failed from cracks nucleated in the triple joint, or point 1 in Figure 38.

Johnston et al. (7) emphasised that the strain data acquired during the fatigue test contain evidence for the liner cracked before the external steel pipe. This finding needs special attention because such fatigue cracks can significantly worsen the performance of installations employing lined pipes or facilitate catastrophic failure on pipelines. As a result of a through-wall crack in the liner taking place when the pipe is transporting corrosive materials, which is usually the case, the crack propagation in the outer pipe could speed-up due to the permeation of corrosive substances through the liner crack. With this in mind, it is of great importance to be able to assess any defect or crack around the triple joint region in order to deploy mitigation measures.

4.2.2 Lined plates description and experimental set-up

The region around the girth weld is challenging to be inspected using ultrasonic techniques due to its microstructure. As a result of the use of austenitic corrosion resistant alloys as filler materials, both the overlay and girth weld regions display anisotropic and inhomogeneous behaviour from the ultrasonic point of view. However, the usage of coherence weights to reduce the side and grating lobes present in the ultrasonic signals can significantly improve the quality of the TFM results.

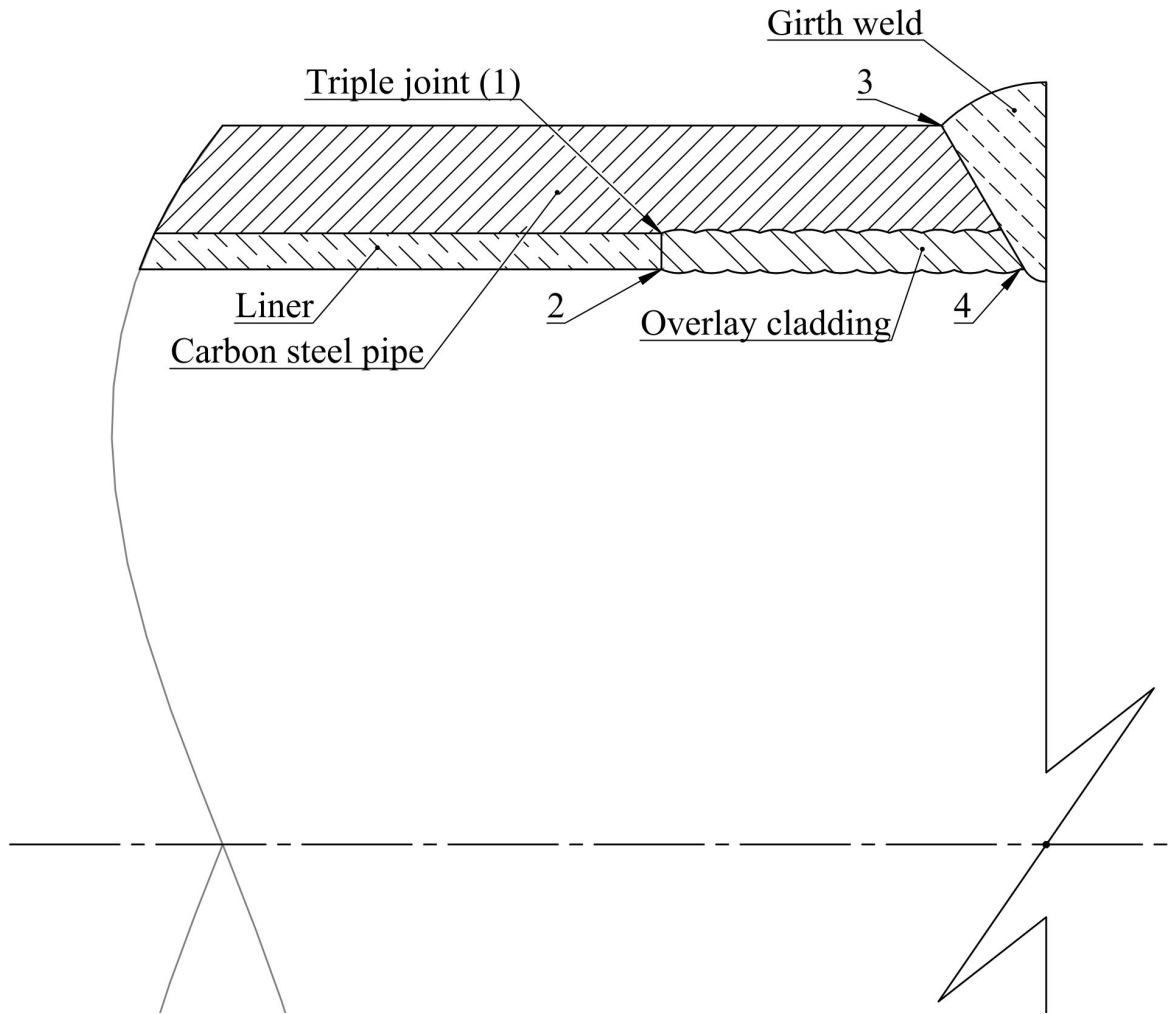


Figure 38 – Lined pipe cross-section schematic drawing. The numbers 1 to 4 indicate the most probable places to nucleate a fatigue crack. Source: the author.

To study the behaviour of some of the coherence weights, applied as a way to improve images obtained with TFM of the triple joint region of mechanically lined pipes, a lined plate was used as a mock-up of this region. The sample plate consisted of an API X65 steel plate with a thickness of 15 mm to mimic the external pipe. On one of its sides, the plate was lined with a 2.5 mm thick Nickel Alloy 625 plate on half of its surface. The other half of that surface received an overlay cladding using Nickel Alloy 625 as filler material. Two notches were inserted via EDM (Electrical Discharge Machining) on the boundary between the overlay and the liner to serve as reflectors for the ultrasonics tests. One of the notches has a depth of 0.8 mm and the other is 1.6 mm deep.

Figure 39 depicts the general geometry of the sample and inserted notches. Meanwhile, Figure 40 shows a cross-section macrograph of the plate showing the 0.8 mm deep

notch with indications for the main points of interest inside the plate. In Figure 40, the region named 'Transition' is the transition between the portion of the cladding which was dressed and the portion it was not. This point will tend to produce a strong indication in the TFM images.

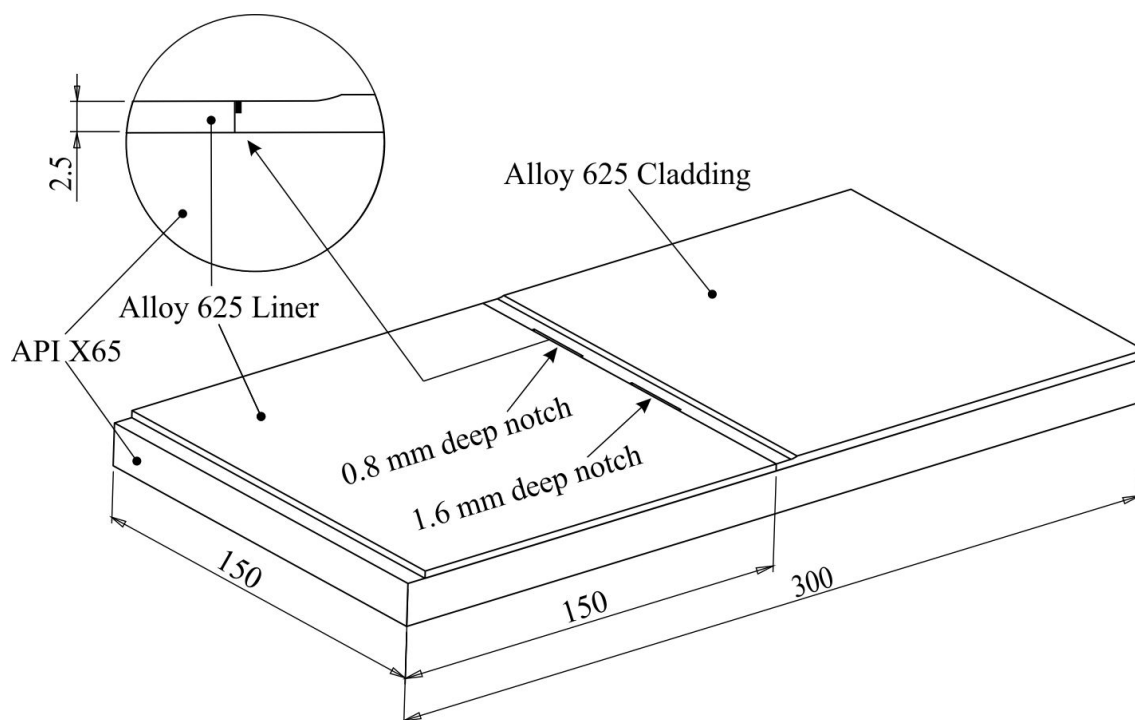


Figure 39 – Geometry of the sample used in this chapter showing in the detail circle the 0.8 mm deep notch. Dimensions are in millimetres. Source: the author.

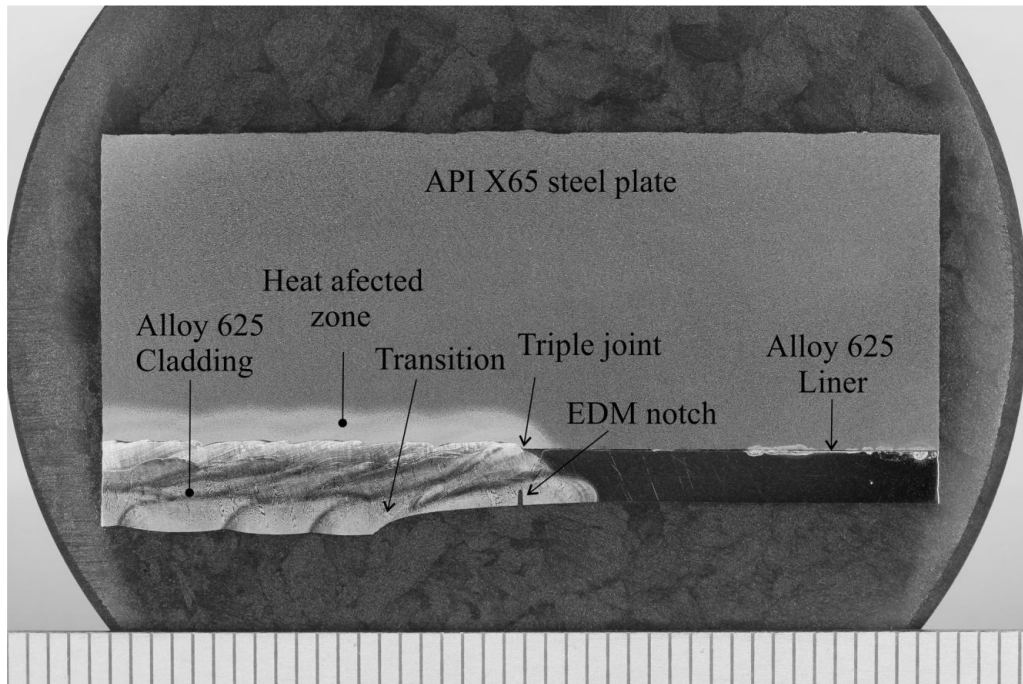


Figure 40 – Macrograph of the plate showing the 0.8 mm deep notch. The scale at the bottom of the image is in millimetres. Source: the author.

On figure 40 it is possible to see a macrograph of a cross-section of the lined plate showing one of the notches. In the region presented in this macrograph, it is possible to visualise part of the cladding on the bottom left and part of the liner on the bottom right. Above the cladding the heat affected zone is evident and following down a straight path from the triple joint one can find the 0.8 mm deep EDM notch.

In order to collect the FMC's for this chapter two probes were used. One of those was a 10 MHz linear phased array probe with a 0.3 mm pitch and 64 elements. The second probe was a 15 MHz linear phased array probe; the pitch of this second probe was 0.2 mm and it also had 64 elements. The data acquisition was carried out in the same immersion tank used in Section 4.1. Each probe was positioned with its centre forming a water path of 20 mm with the front wall of the sample. Since the acoustic beam with the highest amplitude is the one which leaves the transducer at a right angle to its surface, the incidence angle was adjusted to be equal to 11.5° to make its refraction angle equal to 50° according to the Snell's law 3.35⁵. Also, the centre of the probe was set to be aiming

⁵The sound velocity of the water was measured before the experiments. The value obtained for this parameter was 1483 m/s

at the triple joint. Figure 41 illustrates the general configuration of this experiment. The equipment and software used to control and collect data was the M2M Multi++ and Multi 2000, respectively, which are the same employed to acquire the experimental data for the ADTFM. The data was exported via .txt files and post-processed in Matlab, also following the same general procedure used for the ADTFM.

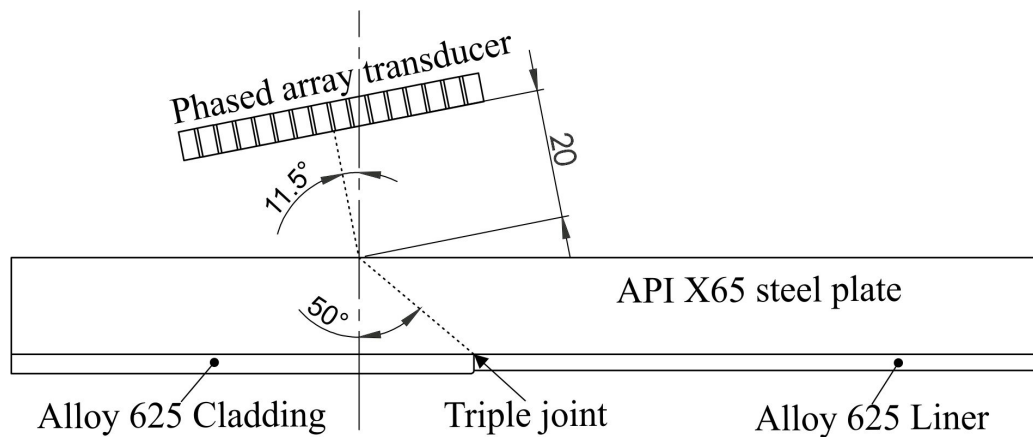


Figure 41 – Experimental configuration used to collect the FMC from the lined plates, dimension are in millimetres. Source: the author.

4.3 Summary

This chapter presented the methodology used throughout this thesis and was divided into two main sections. The first section focused on introducing ADTFM followed by the detailed methodology used to acquire the stiffness matrix of a single crystal made of the same alloy as the test sample. Next, the test sample was described, followed by the experimental and simulation methodologies. Meanwhile, the second section aimed at the description of mechanically lined pipes and sample used as a mock-up of the triple joint region of those pipes. The second section ends with a description of the experimental set-up used to collect the experimental data from the lined plate.

5 RESULTS AND DISCUSSION

Similarly to Chapter 4, this chapter is divided into two sections; the first section concentrates in the results obtained to demonstrate the ADTFM, while the second section focuses on the results obtained with the application of the coherence weights, for both the lined plates and for the austenitic dissimilar weld block. The latter allowed the combination of the results obtained with the ADTFM with those from the coherence weights.

5.1 Adaptive delay total focusing method

This section firstly presents the results obtained from the experimental measurements of the single crystal sample. The single crystal experimental results produced the experimental stiffness matrix of the dissimilar weld block, whose results were used in the simulation carried out to demonstrate the ADTFM method. The simulation and experimental results obtained from the dissimilar weld block and their combination to form ADTFM images encompass the second part of this section.

5.1.1 Single crystal experiment results

The measurements taken using the shear wave contact probe positioned on the flat top and bottom surfaces of the specimen yielded the values presented in Table 2. Meanwhile the measurements of the longitudinal wave with the probe positioned on the same places on the single crystal resulted in Table 3. The immersion experiment results for $V_{L\langle 100 \rangle}$ averaged over the three measurement planes are presented in Table 4. In Table 5 the results for $V_{L\langle 110 \rangle}$ measurements taken under immersion with the same set up as $V_{L\langle 100 \rangle}$ and also averaged over the three measurement planes are shown. On Tables 4 and 5 the results are presented in three columns, the first one was calculated by averaging the results obtained by each transducer for every orientation, thus combining the results from both probes. The remaining two columns are the average from every orientation for

the 10 MHz and 15 MHz probes, respectively. The results between transducers do not differ significantly enough to impair the results ¹. However, a slight difference between the results from each probe was noted, so it is thought to be a good practice to present them separately as complementary information.

Table 2 – Average velocity measured using the shear wave contact probe.

| Probe position | Average $V_{S1\{100\}}$ (m/s) |
|----------------|-------------------------------|
| Top | 3859 |
| Bottom | 3851 |

Table 3 – Average velocity measured using the longitudinal wave contact probe.

| Probe position | Average $V_{L\{100\}}$ (m/s) |
|----------------|------------------------------|
| Top | 5289 |
| Bottom | 5292 |

Table 4 – Immersion measurements results for $V_{L<100>}$

| Angle (°) | $V_{L<100>}$ (m/s) | | |
|-----------|-----------------------|------------------|------------------|
| | Average - both probes | Average - 10 MHz | Average - 15 MHz |
| 0 | 5296 | 5298 | 5288 |
| 90 | 5298 | 5301 | 5288 |
| 180 | 5292 | 5301 | 5283 |
| 270 | 5293 | 5293 | 5293 |

Table 5 – Immersion measurements results for $V_{L<110>}$

| Angle (°) | $V_{L<110>}$ (m/s) | | |
|-----------|-----------------------|------------------|------------------|
| | Average - both probes | Average - 10 MHz | Average - 15 MHz |
| 45 | 6148 | 6155 | 6141 |
| 135 | 6148 | 6151 | 6144 |
| 225 | 6151 | 6155 | 6148 |
| 315 | 6146 | 6148 | 6144 |

Table 6 summarises the immersion velocity measurement results for $V_{L<100>}$ and $V_{L<110>}$; the velocities mean values, standard deviation and confidence interval for 95%

¹The data from 10 MHz and 15 MHz were tested with the two-sample Kolmogorov-Smirnov test in Matlab (82) resulting in p-values of 0.3306 for $V_{L\{100\}}$ and 0.4333 for $V_{L\{110\}}$, such high p-values suggest that the data from both probes are from the same distribution. However, more results are required to improve the reliability of this test.

confidence level compose this table. The measurements of $V_{S1\{100\}}$ and $V_{L<100>}$ with the contact probes did not show sufficient variability above the equipment resolution to allow the calculation of the confidence level; nonetheless, the stiffness constants calculated from the velocities presented in Tables 2 and 3 are presented in Table 7. C_{11} values come from Equation 3.7, whereas C_{44} was calculated with Equation 3.6.

Furthermore, in Table 8, the stiffness matrix elements C_{11} and C_{12} are available alongside their standard deviation obtained using the velocity values from the immersion measurements presented in Table 6. Similarly to Table 7, C_{11} values were calculated with Equation 3.7. On the other hand, C_{12} values were calculated with Equation 3.9. To fill in the variables in Equation 3.9, the values of C_{44} from Table 7, the $V_{L<110>}$ measurements from Table 6 and the values of C_{11} from Table 8 were used.

The standard deviation values for C_{11} and C_{12} in Table 8 were calculated using Equation B.9; the resulting equations are presented as Equations 5.1 and 5.2. In those equations, $\sigma_{V_{L<100>}}$, σ_ρ , $\sigma_{V_{L<110>}}$ and $\sigma_{V_{S1\{100\}}}$ are the standard deviations of their respective subscript variables. Due to the impossibility to obtain the standard deviation of $\sigma_{V_{S1\{100\}}}$ the third term under the square root in Equation 5.2 was considered to be null.

The Monte Carlo method was applied to C_{11} and C_{12} to calculate the standard deviation as an alternative to Equations B.8 and B.9; it is also presented in Table 8 for comparison. Appendix B describes the approach to handle the experimental data presented in this section.

$$\sigma_{C_{11}} = \sqrt{\left(2\rho V_{L<100>} \sigma_{V_{L<100>}}\right)^2 + \left(V_{L<100>}^2 \sigma_\rho\right)^2} \quad (5.1)$$

$$\sigma_{C_{12}} = \sqrt{\left(4\rho V_{L<110>} \sigma_{V_{L<110>}}\right)^2 + \left(2\rho V_{L<100>} \sigma_{V_{L<100>}}\right)^2 + \left(4\rho V_{S1\{100\}} \sigma_{V_{S1\{100\}}}\right)^2 + \left[\left(2V_{L<110>}^2 - V_{L<100>}^2 - 4V_{S1\{100\}}^2\right) \sigma_\rho\right]^2} \quad (5.2)$$

A correlation between variables could mean, for example, that an error source capable of increasing the $V_{L<100>}$ value could also affect the immersion measurement of

$V_{L<110>}$ in a non-random manner. The correlation can be quantified via the calculation of the covariance; however, the covariance between the variables used in the calculation of C_{11} and C_{12} cannot be readily obtained because the different individual measurements do not have specific counterparts. For example, $V_{L<100>}$ and $V_{L<100>}$ measurements were taken from different positions in different times across the sample. Some error sources such as a dimensional variation on the sample, a local microstructure variation, a variation of the water acoustic properties during the measurements and the tilt angle between the sample axis and the probe can affect the correlation, but are considered to be insignificantly small given the experimental set-up used. Therefore, it was considered that the variables are not correlated to a meaningful extent.

Table 6 – Experimental velocities

| | $V_{L<100>} (m/s)$ | | | $V_{L<110>} (m/s)$ | | |
|---|--------------------|--------|--------|--------------------|--------|--------|
| | Both** | 10 MHz | 15 MHz | Both** | 10 MHz | 15 MHz |
| Average (m/s) | 5294 | 5298 | 5288 | 6148 | 6152 | 6144 |
| Standard deviation (m/s) | 9.9 | 7.7 | 8.9 | 9.2 | 7.7 | 8.6 |
| Confidence interval lower boundary (m/s)* | 5290 | 5293 | 5282 | 6144 | 6147 | 6139 |
| Confidence interval upper boundary (m/s)* | 5299 | 5303 | 5296 | 6152 | 6157 | 6149 |

*Confidence interval for 95% confidence level.

**These values were obtained by combining the data of both transducers in the same way of Tables 4 and 5.

Table 7 – Stiffness constants from contact velocities measurements

| Probe position | $C_{11} (GPa)$ | $C_{44} (GPa)$ |
|----------------|----------------|----------------|
| Top | 225.4 | 120.0 |
| Bottom | 225.7 | 119.5 |
| Mean | 225.5 | 119.7 |

From Tables 7 and 8, the stiffness matrix of the Nickel alloy 182 used in the simulations of the dissimilar weld block was considered to be equal to the following

stiffness elements: $C_{11} = 225.8$ GPa, $C_{12} = 143.9$ GPa and $C_{44} = 119.7$ GPa. These values were also used to calculate the slowness surfaces for the material, which are presented below.

Table 8 – Stiffness constants C_{11} and C_{12}

| | C_{11} (GPa) | | | C_{12} (GPa) | | |
|----------------------|----------------|--------|--------|----------------|--------|--------|
| | Both | 10 MHz | 15 MHz | Both | 10 MHz | 15 MHz |
| Mean | 225.83 | 226.18 | 225.4 | 143.85 | 144.25 | 143.53 |
| Standard deviation* | 0.84 | 0.66 | 0.76 | 2.00 | 1.77 | 1.97 |
| Standard deviation** | 0.87 | 0.66 | 0.76 | 1.97 | 1.66 | 1.86 |

*Standard deviation calculated using Equation 5.1 for C_{11} and Equation 5.2 for C_{12} .

**Standard deviation calculated via Monte Carlo method.

The phase slowness surfaces for the longitudinal, fast transversal and slow transversal modes, respectively, are presented in Figures 42, 43 and 44. Those figures were calculated by an algorithm written in Matlab which is capable of transforming the material's stiffness matrix, to solve the Christoffel Equation, to assemble the results and to plot the images.

The algorithm first solves Equation 3.29 for a given set of transformation angles α , β and γ , which defines the orientation of the material by controlling the matrix \mathbf{R}_{ij} (Equation 3.23). The transformed stiffness matrix is then used in Equation 3.1 in order to obtain the slowness curve for that given material's orientation. This process was repeated several times where the angle β was varied in 1° steps, while α and γ were set to be constant and equal to zero. By varying β in small steps while keeping α and γ equal to zero, the stiffness matrix was transformed around its y axis allowing the calculation of a set of slowness curves which were later assembled by the algorithm in the slowness surfaces presented below.

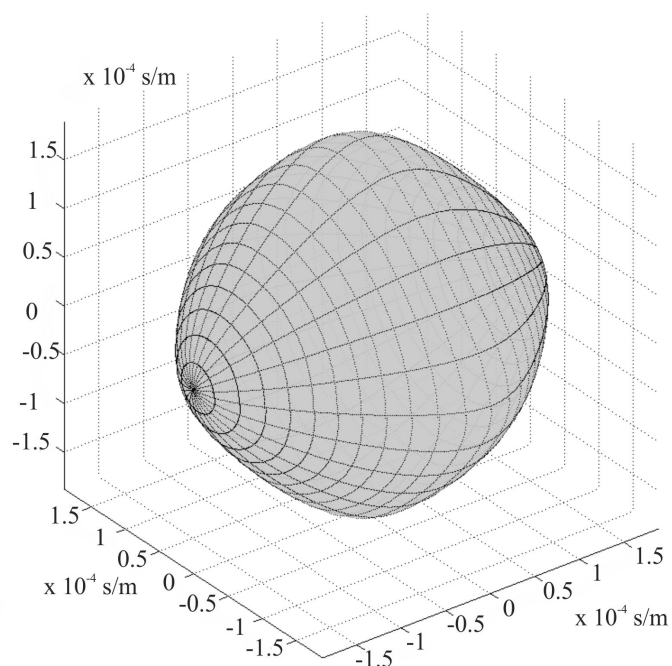


Figure 42 – Phase slowness surface for the longitudinal mode of the single crystal. Source: the author.

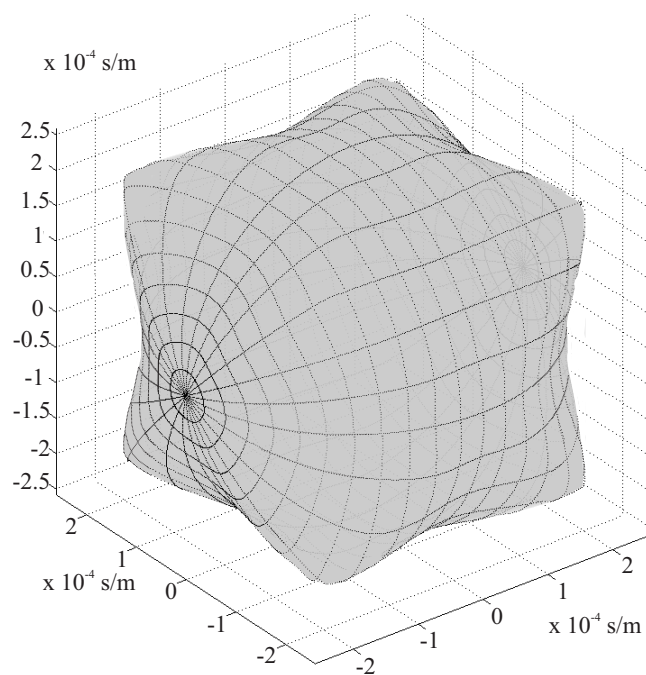


Figure 43 – Phase slowness surface for the fast transversal mode of the single crystal. Source: the author.

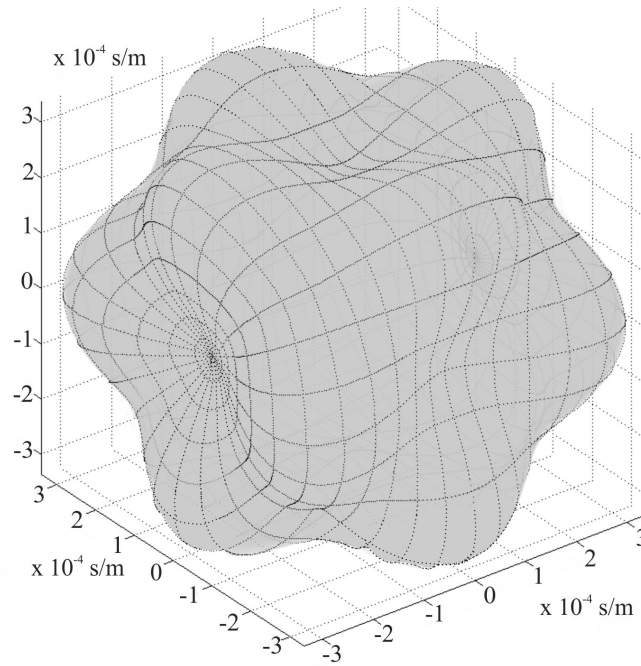


Figure 44 – Phase slowness surface for the slow transversal mode of the single crystal. Source: the author.

Figures 45, 46 and 47 present the group slowness surfaces for the single crystal. Similarly to the slowness surfaces for GaAs presented in Figures 5 to 7 and in Figures 12 to 14, the phase and group slowness surfaces have the same overall shape differing slightly for the longitudinal and fast transversal modes and more significantly for the slow transversal mode. To better illustrate this, Figure 48 presents the phase and group slowness curves for the three modes, for the (001) plane, in the same plot. In this figure, the fast transversal mode has the same phase and group slowness, which does not mean that for other orientations this is maintained (compare Figure 43 with 46). About the slow transversal mode, there are substantial differences between the group and phase slowness; however, both are coincident at 0° and at orientations that are multiples of 45° . Those orientations are equivalent to the $\langle 100 \rangle$ and $\langle 110 \rangle$ families of crystallographic orientations. Similarly, the transversal mode has the same phase and group slowness at 0° and at orientations multiple of 45° , but the variation between the two slowness in other orientations is much less significant than in other planes.

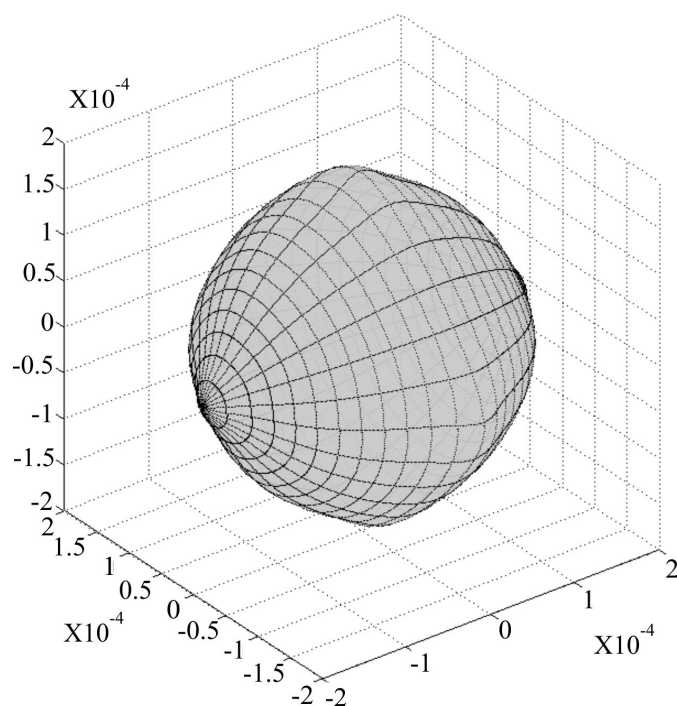


Figure 45 – Group slowness surface for the longitudinal mode of the single crystal. Source: the author.

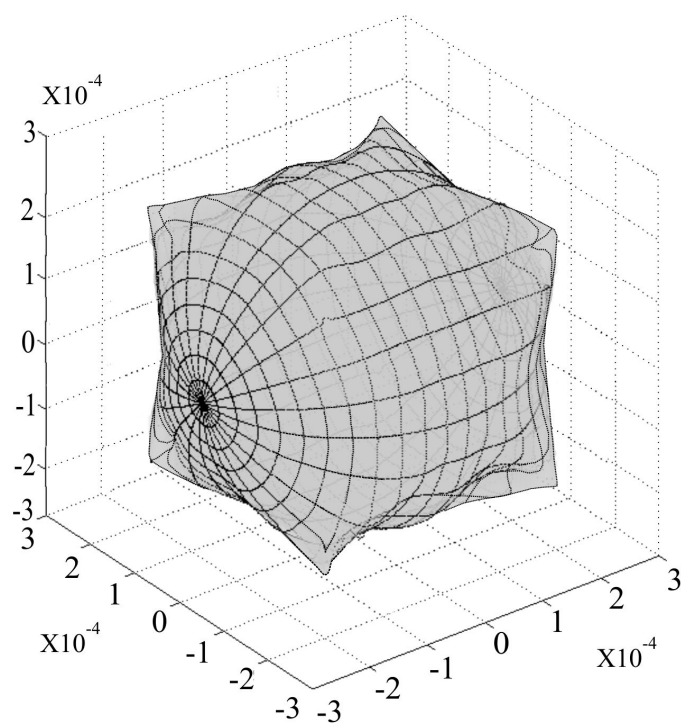


Figure 46 – Group slowness surface for the fast transversal mode of the single crystal. Source: the author.

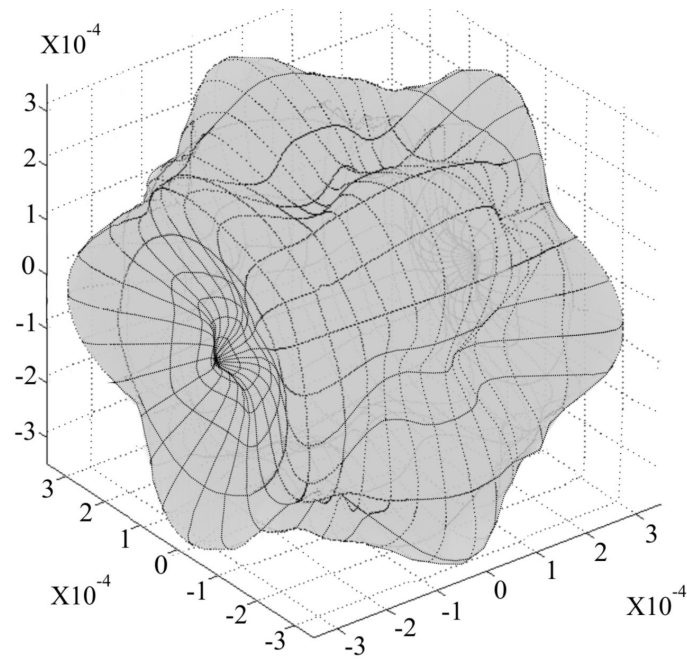


Figure 47 – Group slowness surface for the slow transversal mode of the single crystal. Source: the author.

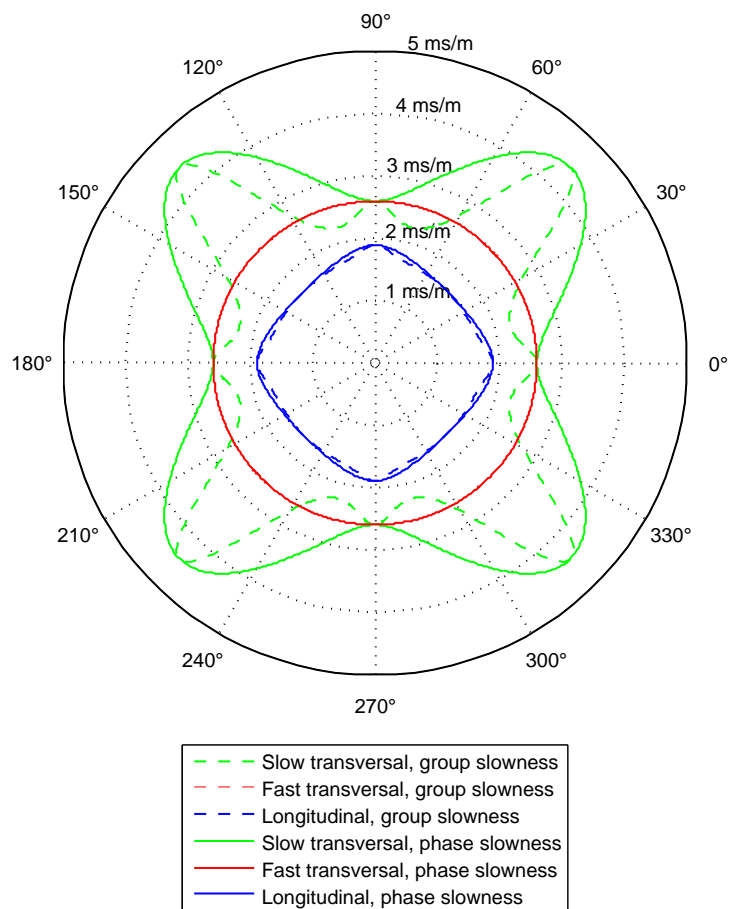


Figure 48 – Comparison between the phase and group slowness curves of the single crystal for the (001) plane. 0° is aligned with the [100] direction, while 90° is aligned with the [010] direction. Source: the author.

5.1.2 ADTFM results

In Figure 49 the results obtained by applying a conventional TFM algorithm on the experimental FMC's for the three parallel planes from which data were acquired are presented. The algorithm, written in Matlab, makes use of the Equation 3.34 to calculate the time of flight between the focusing points and the transducers and, then, applies the results in Equation 3.32 to create the images. In order to be able to compare the conventional TFM results with the ADTFM, the image grid used in Figure 49 was set in the same positions and with the same step size, equal to 0.5 mm, like the one used to simulate the time of flight, described in Section 4.1.5. The resulting images were linearly interpolated via *interp2* Matlab function and are presented on the decibel scale. The signals below -30 dB were truncated to -30 dB to standardise the images and facilitate the comparison with other images.

The true indications in Figure 49 are well above the false indications, with an exception for the top of the images, which are saturated due to the right gain level employed to overcome the attenuation of the material. Other than the top and the side-drilled hole indication, the highest amplitude is below -10 dB of the strongest point in the image, which happens to be on the side-drilled hole indication. As expected, due to the beam skewing caused by anisotropic and inhomogeneous characteristics of the sample, the position of the side-drilled hole indication is displaced from the actual position. In Figure 49, its actual position is represented by a circle in the middle of the images. The indication position should be located on the upper part of the circle if the sample was homogeneous and isotropic.

Before the presentation of the ADTFM images, it is thought to be convenient to present the simulated conventional TFM images. Figure 50 shows those images. It is possible to notice, in Figure 50 (a) the absence of the front wall indication. The vanishing of the front wall indication is expected since the saturation issue does not appear in the simulation. In the same figure, the side-drilled hole indication is positioned on the left side of its actual position. Since its position is approximately the same for the experimental conventional TFM images, it is possible to, qualitatively, assert that the model is capable of

mimicking the behaviour of the actual test piece regarding the side-drilled hole indication. However, the same cannot be said for the noise, which did not show a good correlation between the experimental and simulated images.

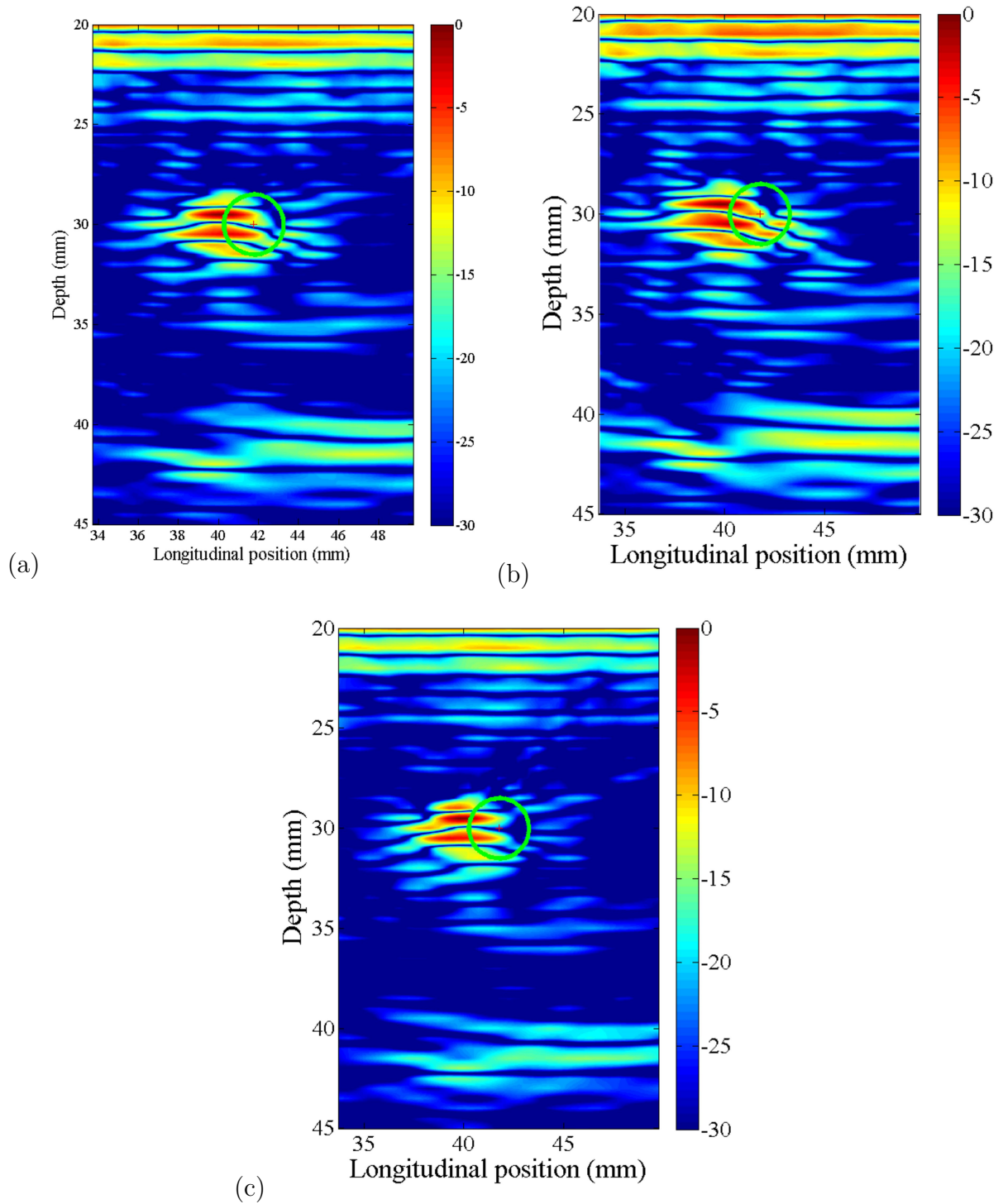


Figure 49 – Experimental conventional TFM results for the three inspected planes. Source: the author.

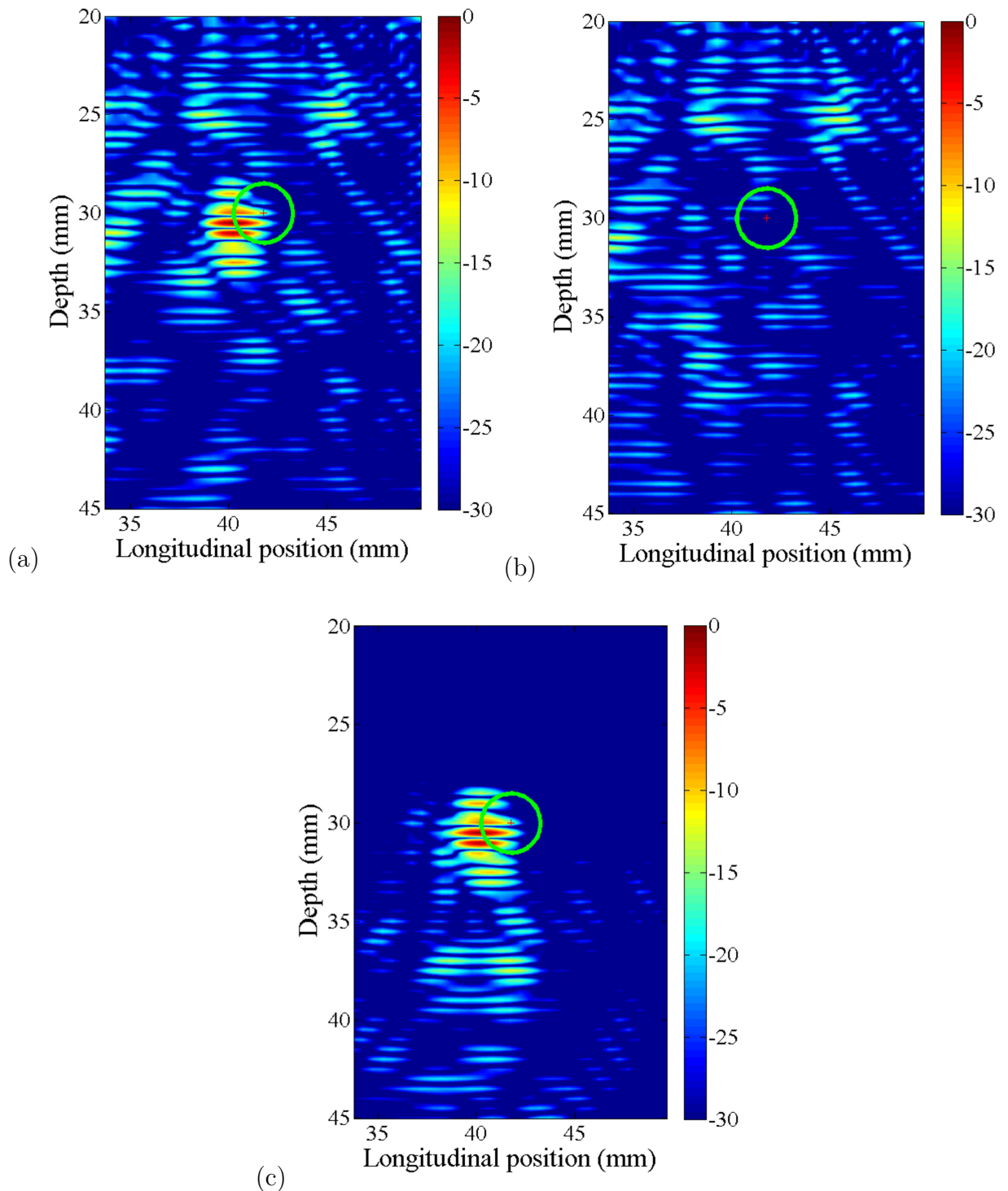


Figure 50 – Simulation results. (a) Simulated conventional TFM with side-drilled hole; (b) simulated conventional TFM without side-drilled hole; (c) the result of the subtraction of the image in (a) by the image in (b). Source: the author.

In Figure 50 (b) the same simulation as in part (a) is presented, but without the side-drilled hole². Due to the absence of a true reflector inside the block, Figure 50 (b) only displays background noise, which can be compared with part (a). Similarly to Figures 49, the scale was set in decibels and the values below -30 dB were truncated to -30 dB. The highest value of part (a) was arbitrary set as the 0 dB reference in part (b), in this way, both images have the same scale, which facilitates the comparison between them. From that comparison, one can notice that the noise matches well for the top portion until around the position of the reflector. Below the side-drilled hole level, the noise diverges significantly between both images, which can be explained by the perturbation caused by the hole on the acoustic waves travelling inside the block. Part (c) presents the result of the subtraction of part (b) from part (a), i.e. $(a) - (b)$, to better illustrate the hole influence on the acoustic waves.

In Figure 51 the ADTFM images generated from the same experimental data used to create the images shown in Figure 49 are presented. Following the same standard of the previous images shown in the present section, the images on Figure 51 are presented on the decibel scale whose values below -30 dB were truncated to -30 dB. The most remarkable feature found in Figure 51 is the correct position of the side-drilled hole indication for the three inspected planes. Comparing this figure with Figure 49, it is possible to notice that the noise level is equivalent among them. Moreover, overall, the false indications present in the conventional TFM images are also present in the ADTFM ones, which indicates that they come from experimental FMC and are not artefacts added from the simulated TOF.

²This was possible because the EBSD data used in the model was acquired prior to the machining of the side-drilled hole.

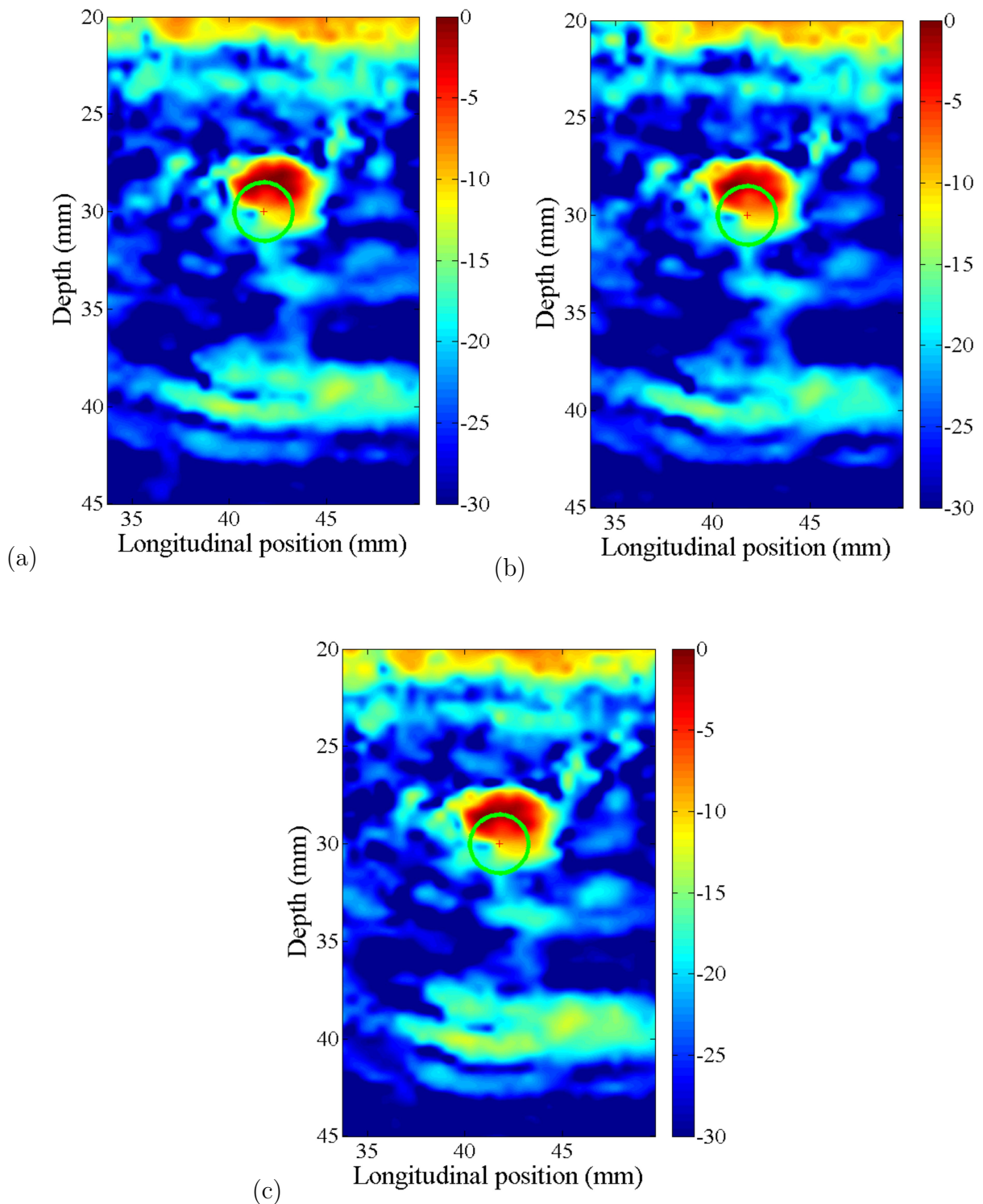


Figure 51 – ADFM results for the three inspected planes. Source: the author.

In addition, both TFM and ADFM images depict false indications in their top, from 20 mm to 24 mm, coming from the saturation of the A-scans around the front wall of the block. Another feature of the ADFM image is the absence of the peaks and

troughs structure on the indications that are shown both in the experimental and simulated conventional TFM images. This blurring is thought to be due to the uncertainties of the time of flight calculation. More specifically, the orientation unification and coarse step size employed for the EBSD map acquisition, the higher frequency phased array probe employed alongside the inaccuracy of the 2D stress state assumption are considered to be responsible for the blurring. Nonetheless, the EBSD map, the phased array probe and the numeric model used were demonstrated to be precise enough to position the side-drilled hole in the image correctly. However, further investigation on how to minimise the uncertainties involved in the generation of the numeric model and EBSD map are required. Also, it can be said that the lack of peaks and troughs are not a major concern of those ADTFM images.

5.2 Coherence weights

In this section one can find the results obtained from the application of coherence weights on conventional TFM images from the lined plate, which mimics the triple joint region of mechanically lined pipes. In addition, the results from the coherence weights applied to the conventional experimental TFM images and ADTFM images from the dissimilar weld block are presented.

5.2.1 Coherence weights applied on lined plate's images

Using the standard TFM algorithm in the data obtained with the sample and phased array probe immersed in water, some images were created to make the first assessment of those regions. A TFM image is displayed in Figure 52 where it is possible to visualise some of the points and regions indicated in Figure 40, but the boundary present between the overlay clad and the base material is not visible in this image. The gain used during the data acquisition was optimised to maximize the amplitude around the triple joint. As a consequence the signals became saturated around the front wall, where the ultrasonic beams enter the specimen causing noise and false indications in the region surrounding

it. However, since the study of the carbon steel plate is not among the objectives of this work, the saturation of signals coming from it is acceptable.

In order to visualise the boundary between the overlay clad and the base material, the image presented in Figure 52 is displayed in decibels in Figure 53, where all the indications pointed out in Figure 52 are also present. It is possible to notice an increase in the noise on this figure in comparison with the previous one. Here, signals below -60 dB, equivalent to one-thousandth of the maximum pixel amplitude, have not been taken into account and were truncated to -60 dB in order to create an image standard for better comparison with other results. For both Figures 52 and 53, a step size of 0.1 mm was used for the TFM grid and the original pixel images were linearly interpolated in Matlab.

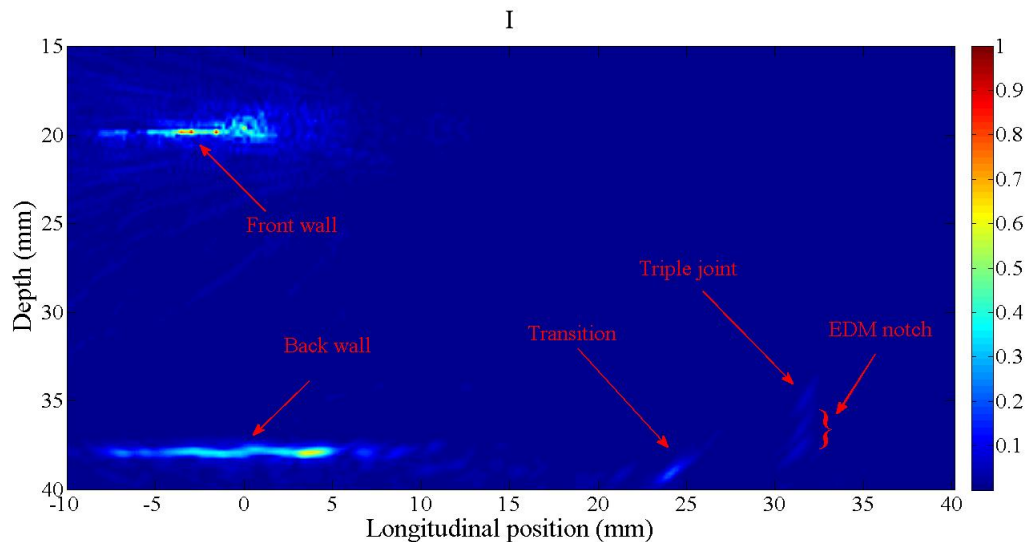


Figure 52 – Conventional TFM image of the triple joint region showing the 0.8 mm deep notch using the 10 MHz probe, linear scale and arbitrary units. Source: the author.

Figure 54 shows in detail the triple joint and 0.8 mm deep notch indications. The data used for this figure is the same as for Figures 52 and 53. The step size of Figure 54 was 0.1 mm and it was also subjected to linear interpolation. Also, this image is presented on the decibel scale with the pixel relative amplitude truncated at -60 dB as well. The three indications in Figure 54 come from the root of the notch, the tip of the notch and the triple joint, as indicated on it. The decibel colour scale was renormalised, which makes the indications shift towards the red colour in comparison with Figure 53, emphasising the

noise. Another characteristic of Figure 54 and, for consequence, Figures 52 and 53 is the distortion present in the cladding region. Since the conventional TFM and the coherence weights do not affect the image distortion caused by anisotropy and inhomogeneity, it is anticipated that the fraction of the images corresponding to the overlay clad will have some degree of distortion. In Figure 54 one can visualise that the distortion is mainly confined to the vertical direction.

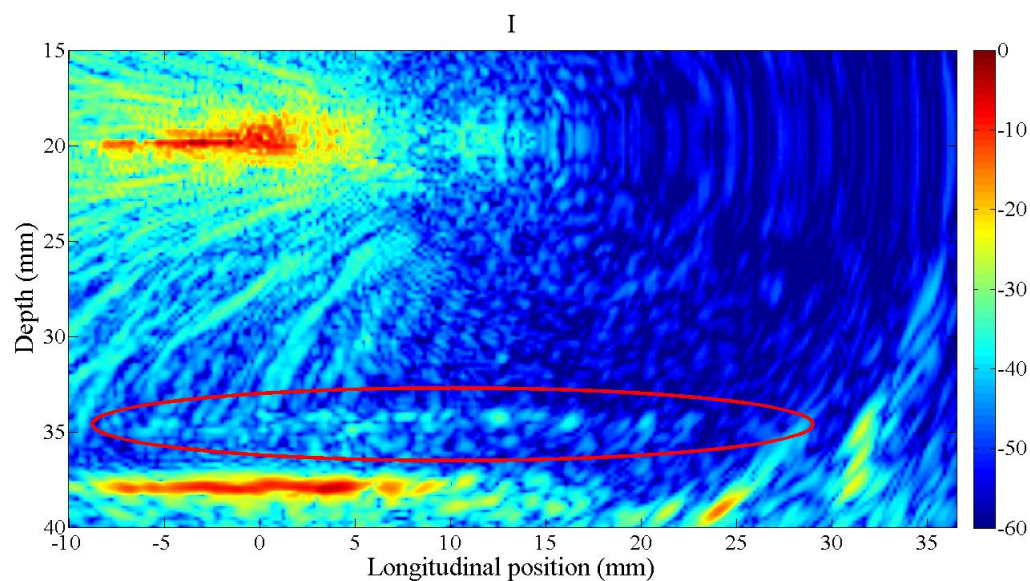


Figure 53 – Conventional TFM image of the triple joint region showing the 0.8 mm deep notch using the 10 MHz probe; the red ellipse indicates the boundary between the cladding and the steel plate. The image is in the decibel scale. Source: the author.

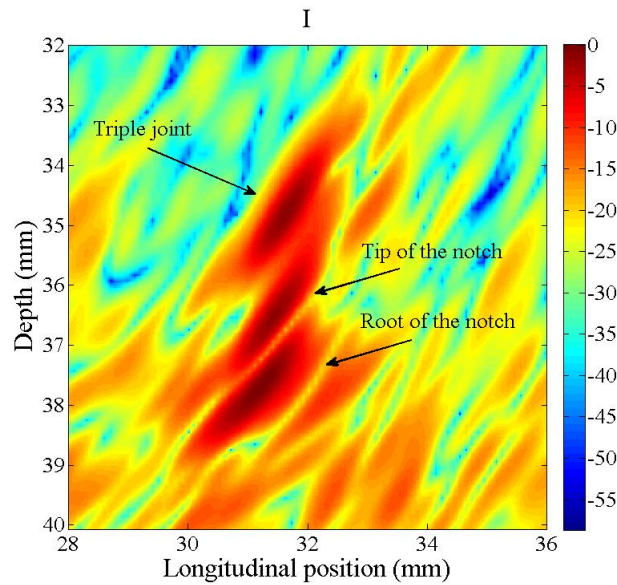


Figure 54 – Conventional TFM image of the triple joint region, showing in detail the triple joint, tip of the notch and root of the notch indications. This figure is presented on the decibel scale. Source: the author.

In Figure 55, the conventional TFM images of the three regions of the lined plates which were analysed are presented. Since the images introduced in this figure have a high level of noise, they are suitable to evaluate the performance of the different coherence weights. The 10 MHz phased array probe was used to collect the FMCs for Figure 55 and to calculate the pixel size chosen for the TFM images was 0.1 mm. After the TFM images were calculated, they were linearly interpolated in Matlab. In Figure 55, one can notice that the triple joint and notch indications are not the strongest indications in the images; the same can be said for Figures 52 and 53. The decision to include indications outside the region of interest (triple joint) is intended to provide strong reference points in all images and to evaluate the performance of the coherence weights better. It is worthwhile noticing that the triple joint and notch indications are stronger for the 0.8 mm notch than for the 1.6 mm notch. Also, the unnotched region has the weakest triple joint indication of all the three images.

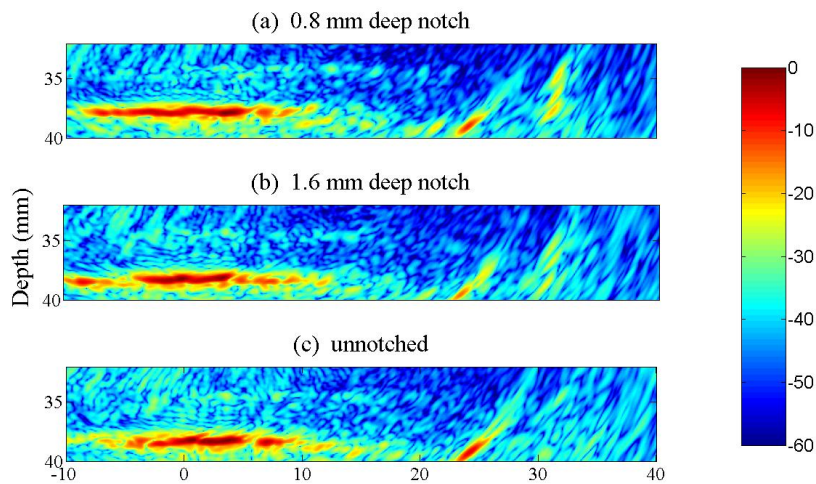


Figure 55 – Conventional TFM images of the three regions of the lined plate analysed. Data collected with the 10 MHz probe. Source: the author.

In Figures 56, 57 and 58 the TFM images of the bottom part of the lined plates where the CF was applied are shown. The figures are from the 0.8 mm deep notch, 1.6 mm deep notch and a region free of notches, respectively. In each of those figures, four images were presented where the sensitivity factor, P_{CF} , was varied from 0.5 to 2 with 0.5 step. As expected, the amplitude of all the indications diminishes as a function of the sensitivity factor³. For Figures 56 and 57 the best results were obtained when the sensitivity factor was equal to one. However, the triple joint and notch indications for Figure 56 (b) are better highlighted than for Figure 57 image b. On the other hand, Figure 58 does not show a clear indication of the triple joint, which can compromise the ability of the inspector in finding its position. Nonetheless, the images presented show that it is possible to distinguish between the three conditions (0.8 mm, 1.6 mm notch and unnotched) using TFM images and significantly improve the signal to noise ration with CF.

³The relative amplitude of the strongest pixel remains equal to 0 dB regardless of the sensitivity factor due to the normalization carried out in each figure.

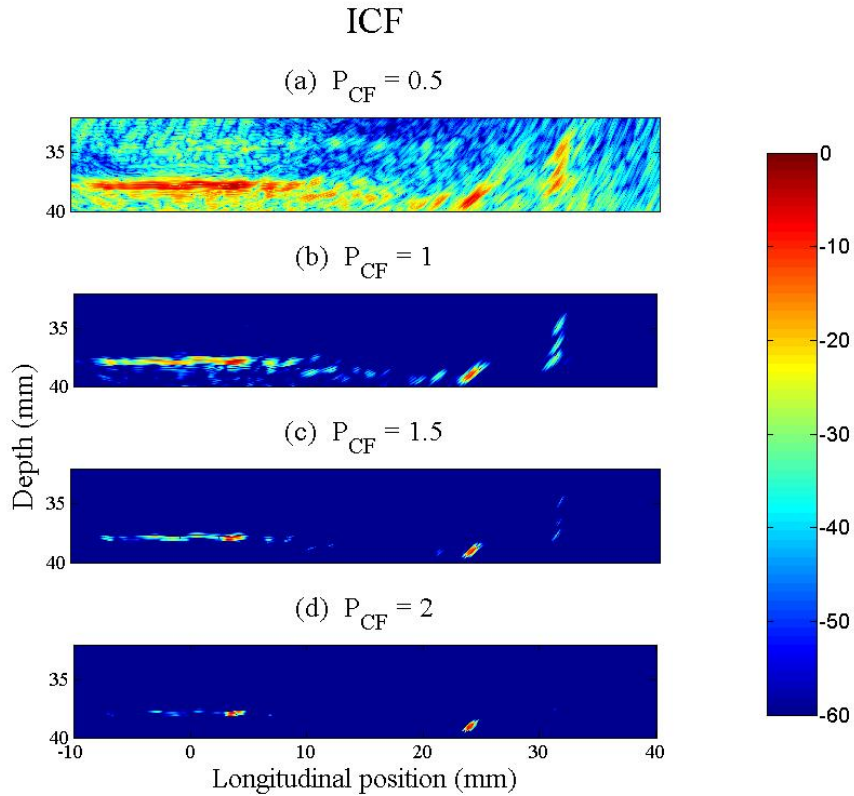


Figure 56 – ICF images for several P_{CF} from the 0.8 mm deep notch using the 10 MHz probe. Source: the author.

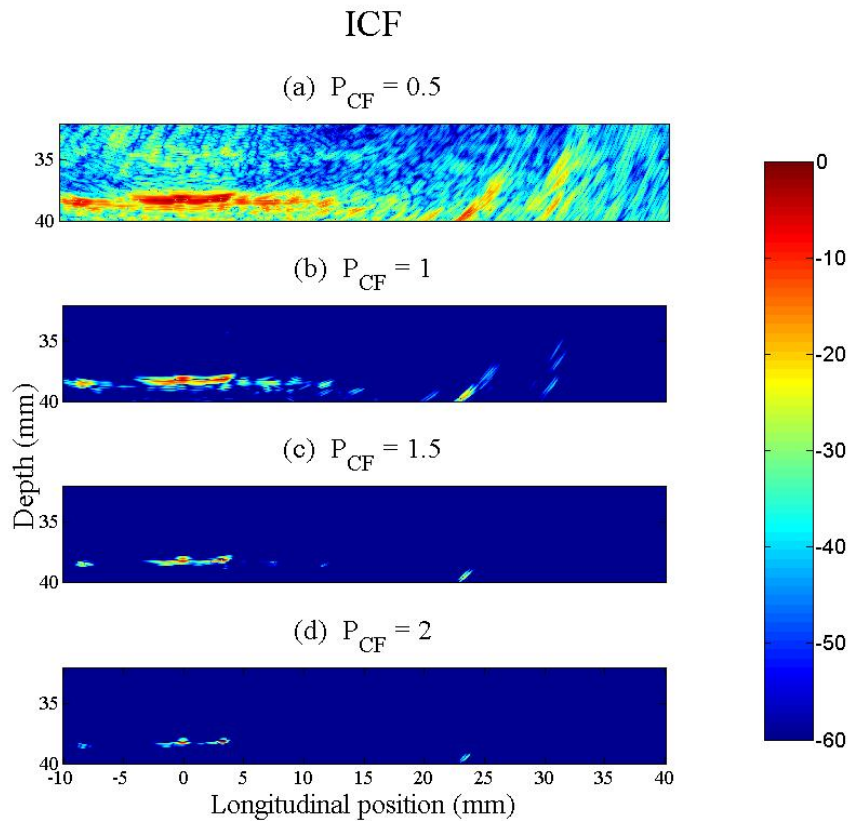


Figure 57 – ICF images for several P_{CF} from the 1.6 mm deep notch using the 10 MHz probe. Source: the author.

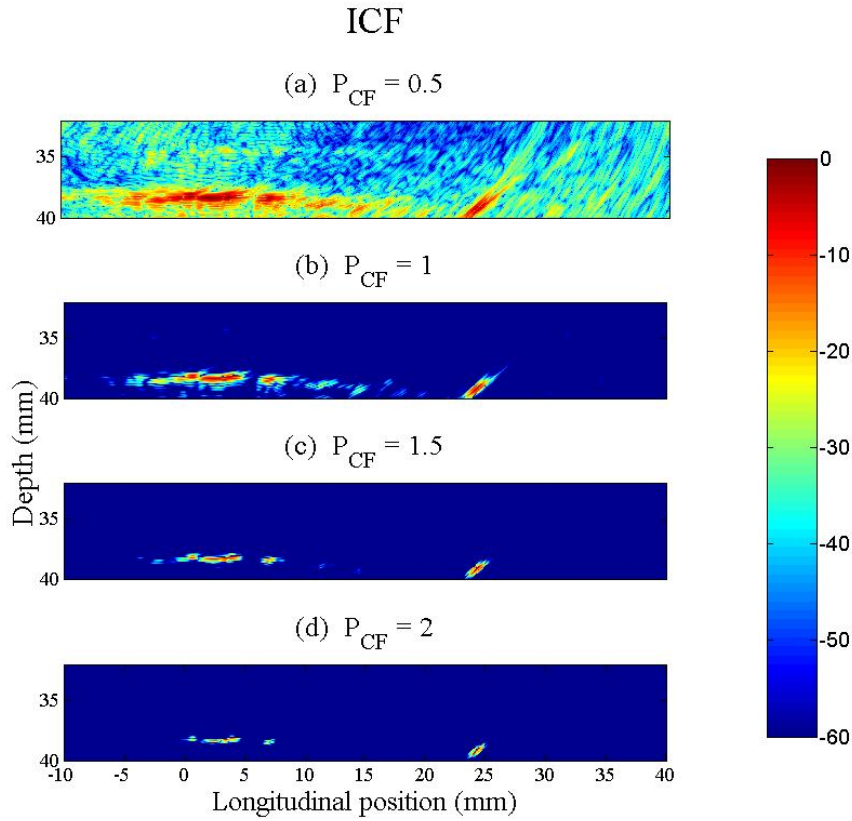


Figure 58 – CF images for several P_{CF} from the region without any notch using the 10 MHz probe. Source: the author.

Figures 59 and 60 present the IPCF and ISCF results for the 0.8 mm deep notch using the 10 MHz probe. Like the previous figures, four images are presented on each of Figures 59 and 60, where the sensitivity factors P_{PCF} and P_{SCF} are varied. P_{PCF} values used are 1, 2.6, 2.7 and 2.8, while P_{SCF} values are equal to the P_{CF} ones from Figures 56, 57 and 58. The remaining four figures regarding the IPCF and ISCF results for the 1.6 mm deep notch and from the unnotched region are presented as complementary information in Appendix C.

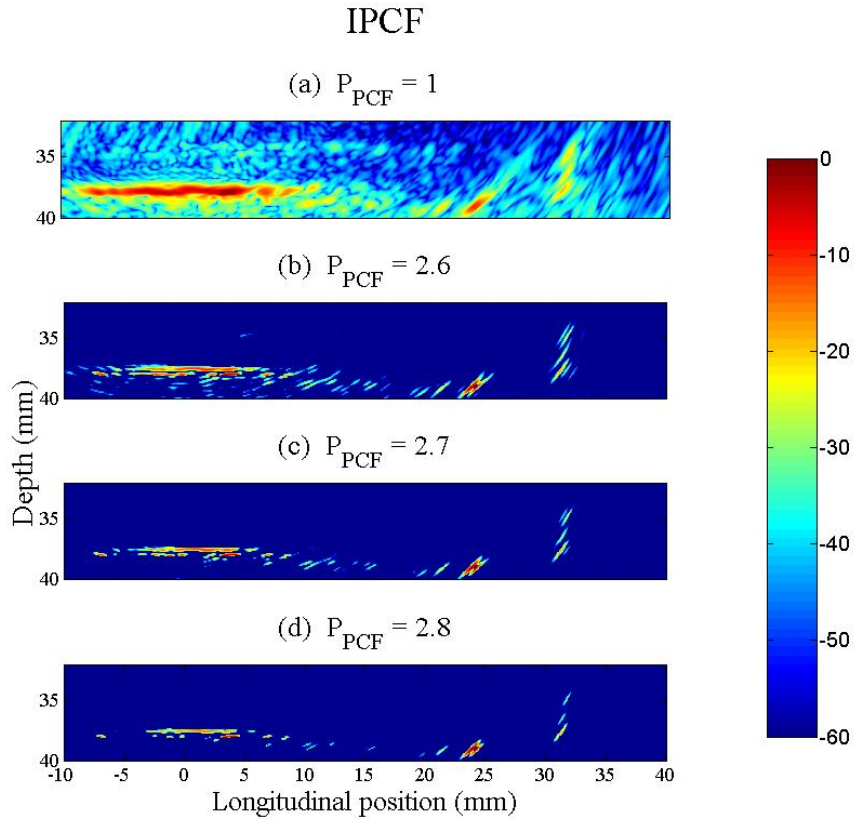


Figure 59 – IPCF images for several P_{PCF} from the 0.8 mm deep notch using the 10 MHz probe. Source: the author.

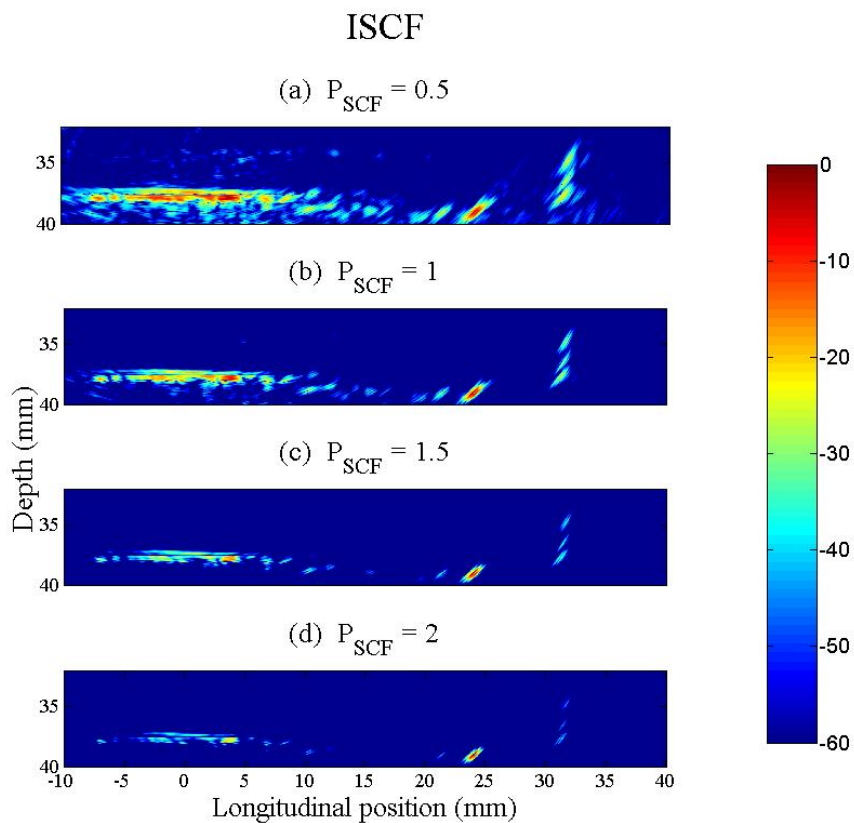


Figure 60 – ISCF images for several P_{SCF} from the 0.8 mm deep notch using the 10 MHz probe. Source: the author.

In Figure 59 the 0.8 mm deep notch TFM image subjected to PCF is presented, where it is possible to visualise that the triple joint, notch tip and notch root are present for the four sensitivity factor amplitudes. However, it is essential to keep in mind that above a specific value, P_{PCF} makes all pixel values equal to zero. Care has been taken in order to keep P_{PCF} below this threshold. Moving to Figure 60 one can notice that P_{SCF} sensitivity factor can reduce most of the noise even when its amplitude is equal to 0.5. Also, the three indications, triple joint, notch tip and notch root, are visible in all the four P_{SCF} amplitudes presented here.

Similarly to CF, both PCF and SCF are capable of improving the TFM image quality of the lined plate triple joint region when using the 10 MHz probe. However, the unnotched region could not be adequately imaged by any of the coherence weights used (see Figures 69 and 71 in Appendix C). For the notched regions, the performance of the coherence weights varies significantly as a function of the sensitivity factor. Because of that, it is important to adjust their value carefully, in order to minimise the noise amplitude without compromising the true indications.

In Figure 61 one can find the standard TFM images obtained from the data collected with the 15 MHz probe. This figure is equivalent to Figure 55, with the 15 MHz probe was positioned in the same three regions. By comparing the later with Figure 61, one can notice that the results obtained with the 15 MHz probe have a significantly higher noise level and the three indications corresponding to the triple joint, notch tip and notch root are challenging to identify. The parameters used to generate the images from the 15 MHz probe data were set to be the same used for the 10 MHz probe images.

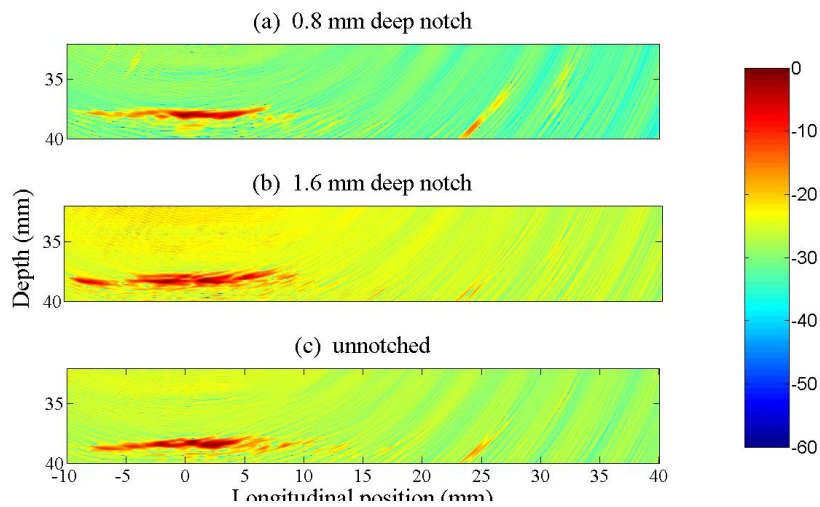


Figure 61 – Conventional TFM images of the three regions of the lined plate analysed. Data collected with the 15 MHz probe. Source: the author.

In Figures 62, 63 and 64 the TFM images from Figure 61 subjected to the SCF at four sensitivity factors values are presented. Those figures show that the performance of the coherence weights when using the 15 MHz probe is reduced when compared with the same results obtained by using the 10 MHz probe. The unsatisfactory performance can be attributed to the signal to noise ratio present in the data, which cannot be effectively improved by applying the coherence weights. Given that, the images regarding CF and PCF are omitted from this thesis.

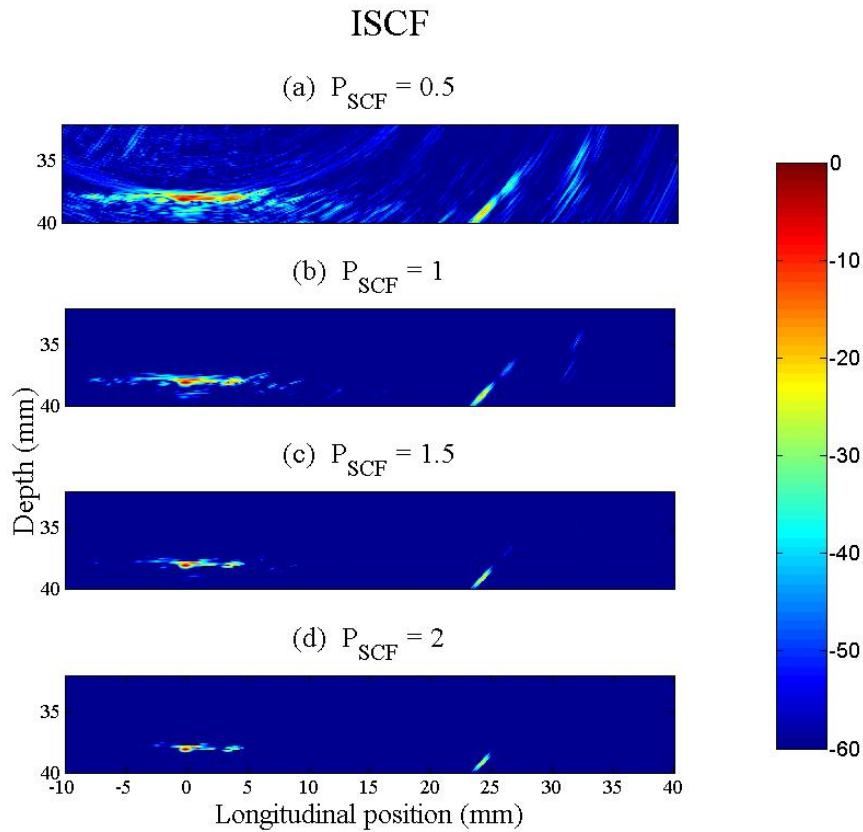


Figure 62 – ISCF images for several P_{SCF} from the 0.8 mm deep notch using the 15 MHz probe. Source: the author.

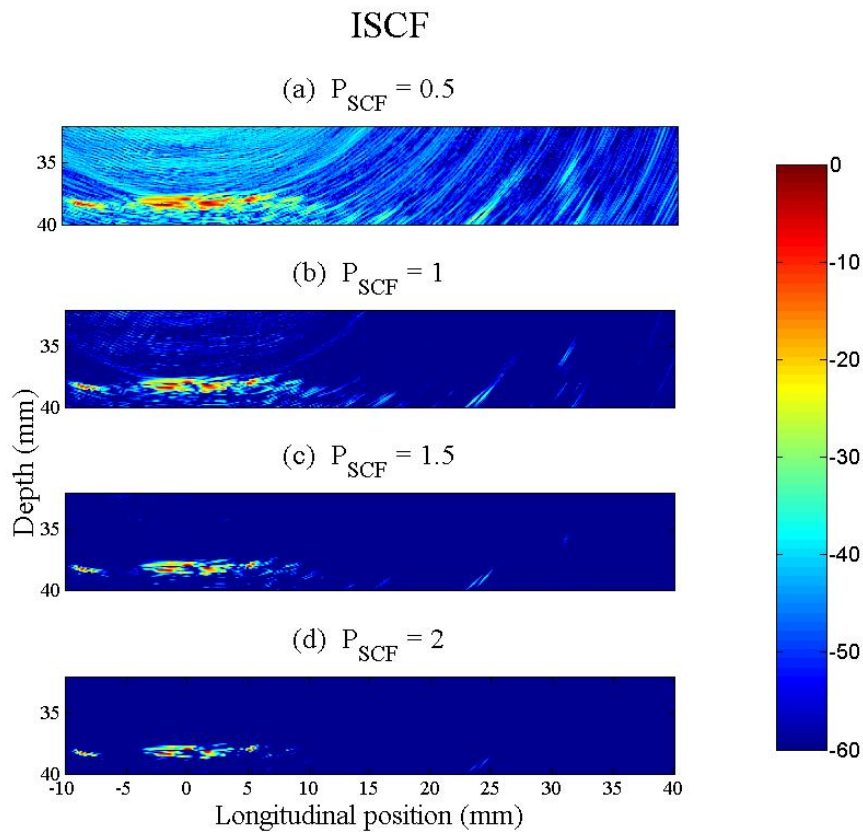


Figure 63 – ISCF images for several P_{SCF} from the 1.6 mm deep notch using the 15 MHz probe. Source: the author.

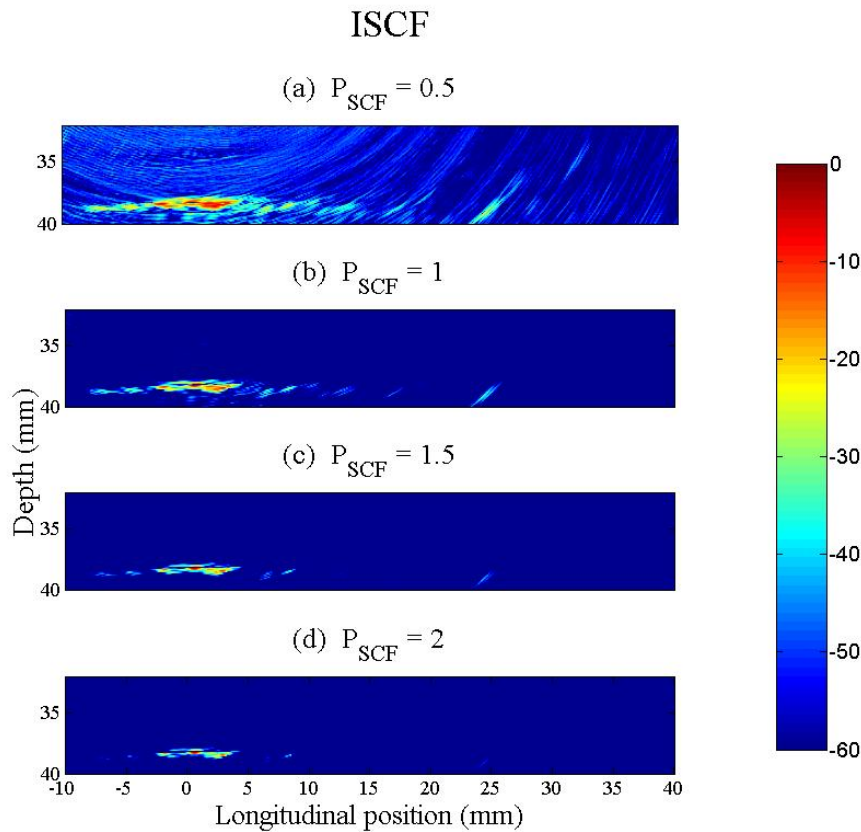


Figure 64 – ISCF images for several P_{SCF} from the unnotched region using the 15 MHz probe. Source: the author.

5.2.2 Coherence weights applied on dissimilar weld block images

Figures 65, 66 and 67 are the results obtained from applying the three coherence weight methods into the ADTFM image. The experimental data used to create these three figures is the same employed in the ADTFM image showed in Figure 51. As complementary information, in Appendix C one can find Figures 72 to 77 regarding the application of the coherence weights on the data corresponding to the images presented in Figure 51 (b) and (c).

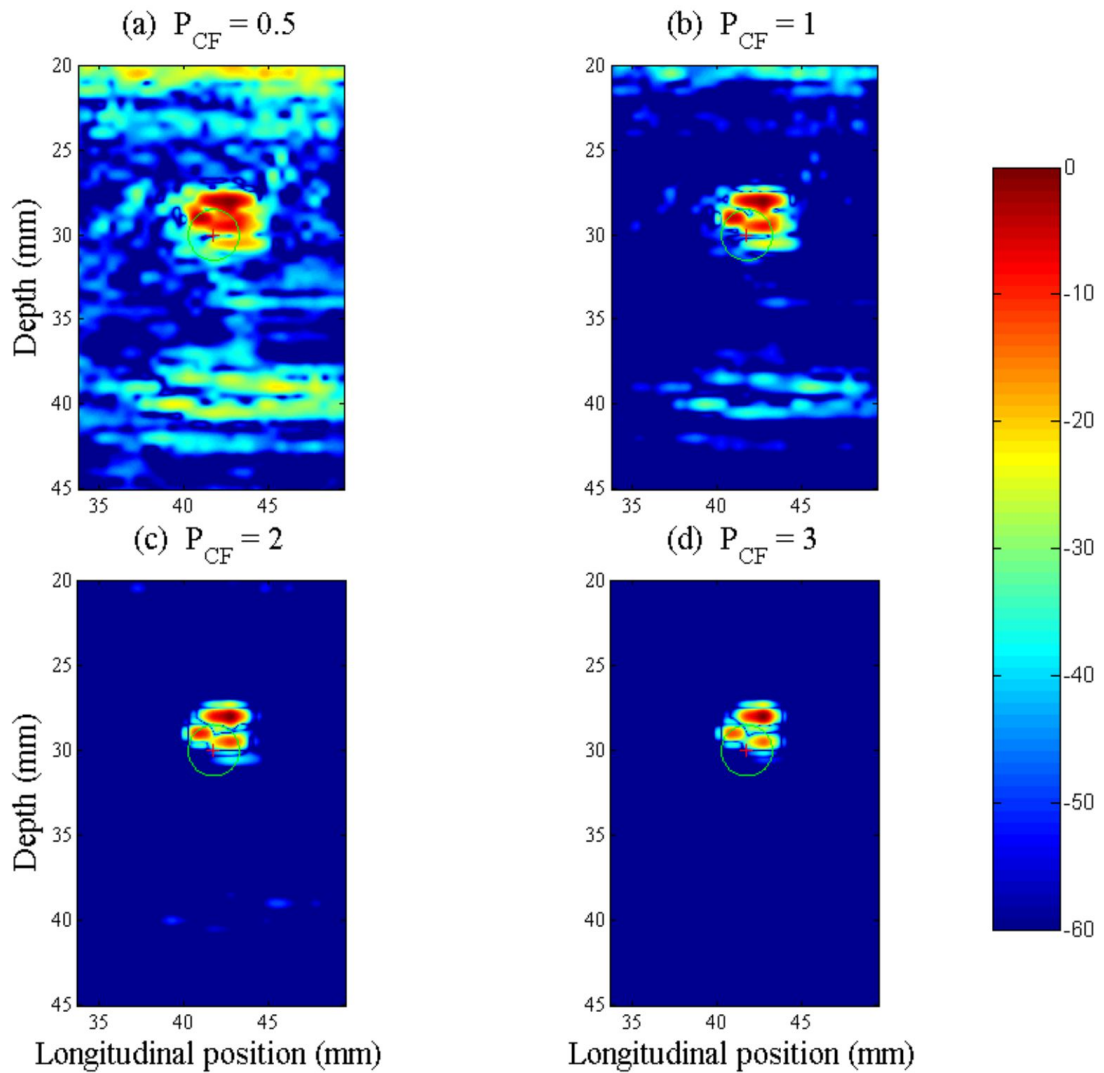


Figure 65 – ICF applied to the ADTFM image of the dissimilar weld block for four sensibility factor amplitudes. This image was obtained from the ADTFM image presented in Figure 51 (a). Source: the author.

The results of the application of the three coherence weights into ADTFM images was successful. All coherence weights used were capable of reducing the false indications, noise and the signal saturation on the top of the images below the threshold of $-60dB$ below the strongest pixel. Together with the ADTFM, the main issues with the weld block inspection caused by its inhomogeneity and anisotropy were bypassed.

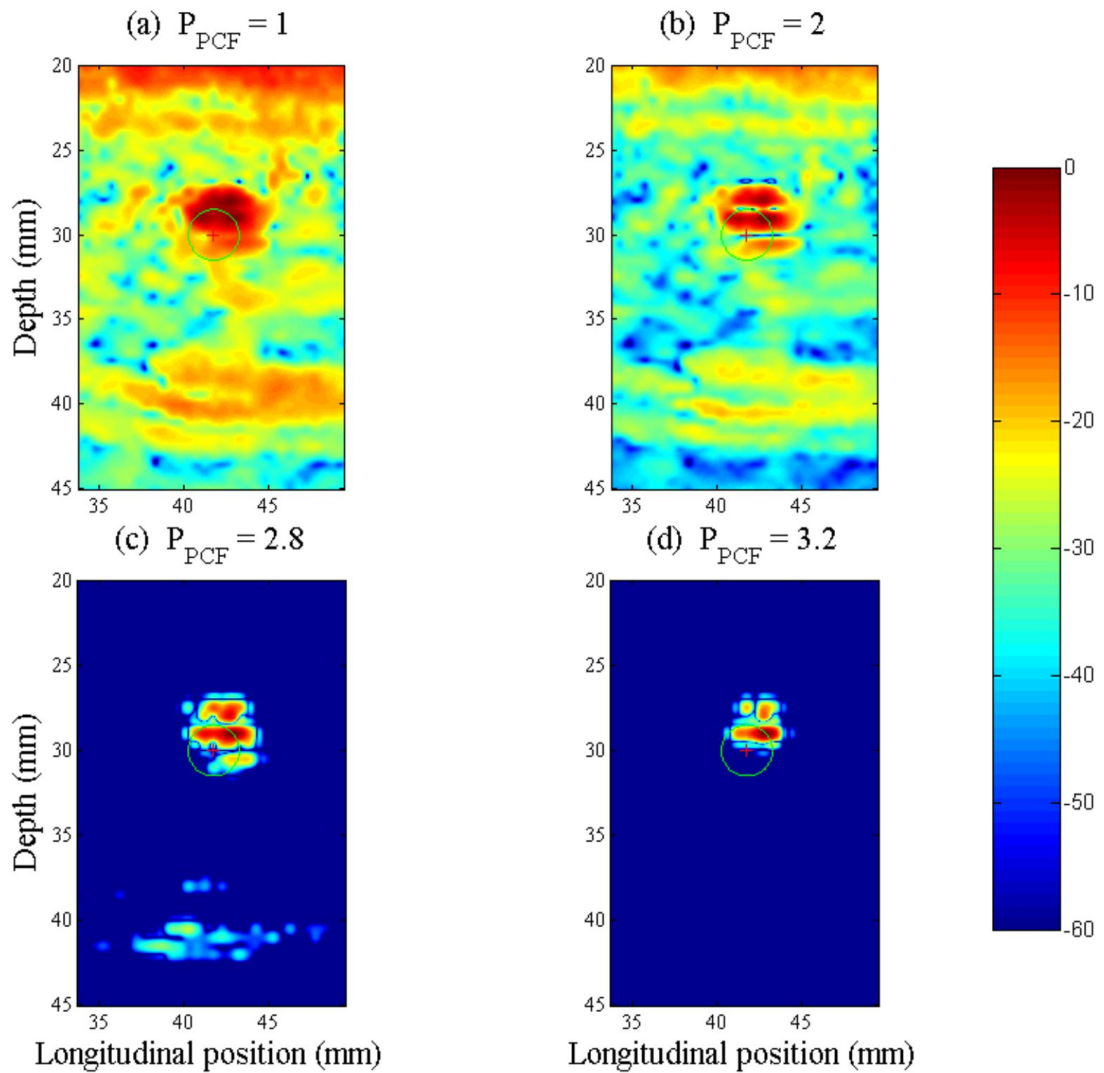


Figure 66 – IPCF applied to the ADTFM image of the dissimilar weld block for four sensibility factor amplitudes. This image was obtained from the ADTFM image presented in Figure 51 (a). Source: the author.

Since the images present in this subsection used the same ADTFM results shown in Section 5.1, some of the drawbacks pointed out there can still be valid here. The cost and time ineffective EBSD analysis and the inaccuracy of the 2D finite element modelling used to represent the weld block during the time of flight calculations are thought to be the most important ones. However, the results presented in Figures 65, 66 and 67, indicate that the noise problem can be solved by using coherence weights methods. Nonetheless, it is essential to investigate this method further in other samples made with other materials and with other grain structures.

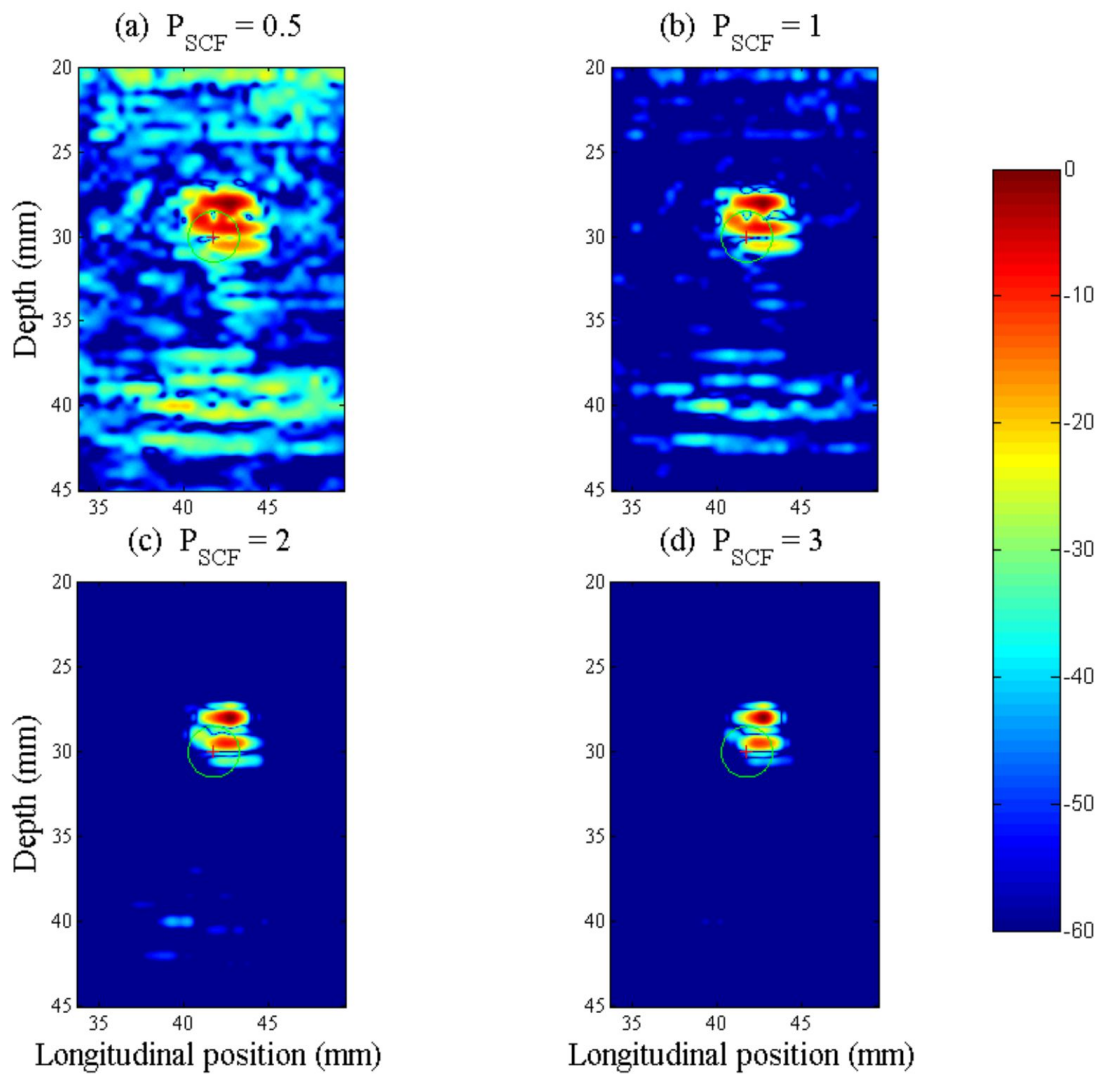


Figure 67 – ISCF applied to the ADTFM image of the dissimilar weld block for four sensibility factor amplitudes. This image was obtained from the ADTFM image presented in Figure 51 (a). Source: the author.

6 CONCLUSION

The proposed ADTFM method has been able to correct the position of a side-drilled hole indication from the dissimilar weld block studied, which demonstrated its viability. In order to allow the implementation of the ADTFM, it was necessary to acquire the stiffness matrix required for the computational modelling of the weld block. The stiffness constants that make up the stiffness matrix were obtained via acoustic measurements carried out on a single crystal sample made of Alloy 182, which is the same alloy most of the block is composed of. Two measuring approaches were used in order to obtain the necessary information. Both of them rendered equivalent results for the C_{11} stiffness constant. However, further measurements are required, especially for the shear wave measurements in order to improve the statistical relevance of C_{44} and C_{12} . Also, in order to improve the measurements, a more accurate method to detect the peak should be investigated. A cross-correlation approach may be suitable for this task. The ADTFM model needs a description of the grain structure and orientation inside the material, for the present work the block used was modelled using an EBSD map. Besides the results showing that the EBSD approach is capable of representing the weld with sufficient precision to be used in the creation of ADTFM images, it is not usually a viable option mainly due to the high cost involved in its obtainment. However, the destructive nature of the EBSD analysis and the time it takes to be accomplished are also meaningful drawbacks for this method of crystallographic orientation mapping. Other approaches capable of representing the sample's crystallographic orientation need to be investigated, such as MINA (11), ray-tracing methods (52) and the macrograph method (10).

Regardless of the positive results presented in this thesis, it is important to investigate the ADTFM method further by employing different materials and with different kinds of reflectors. Moving the inspection system further into the stochastic regime by either increasing the probe frequency or the sample grain size can also give a better insight about the ADTFM applicability in a more challenging situation. On the other hand, a

increase in the probe's frequency would mean an increase in the computation time needed to calculate the time of flight. Since the time taken to calculate the time of flight is one of the most critical concerns for ADTFM, one needs to consider the viability of the method when it is required to inspect a large area or before increasing the inspection frequency. Moreover, due to the time-consuming simulation step, the ADTFM would be more suitable for situations where the inspection needs to be executed repeatedly on several identical parts or regions, for example, in the inspection of girth welds in a pipeline.

In addition to the ADTFM, this thesis analysed three coherence weights as tools to reduce the noise and false indication in TFM images from a plate, built to mimic the triple joint region of mechanical lined pipes. This region is taken into serious consideration by those who operate this kind of pipe due to the susceptibility of crack nucleation. Overall, the coherence weights have been capable of improving the quality of the TFM images, especially for those images obtained from the data collected with the 10 MHz probe. When combined with ADTFM data from the weld block, the coherence weights have been capable of reducing the noise and false indications by at least 60 dB below the amplitude of the strongest pixel of those images, i.e. the noise amplitude drops to a value not higher than one-thousandth of the amplitude of the strongest pixel in the image. Furthermore, it has been demonstrated that it is possible to combine both approaches in order to minimise the deleterious effects of anisotropy and inhomogeneity in the inspection of the weld block. Moreover, it is necessary to investigate the behaviour of those combined methods in other samples and situations to be able to draw a full picture of their capabilities.

Bibliography

- 1 AULD, B. A. *Acoustic Fields and Waves in Solids*. [S.l.]: John Wiley & Sons, 1973.
- 2 CHEEKE, J. D. N. *Fundamentals and applications of ultrasonic waves*. Boca Raton: CRC Press LLC, 2002.
- 3 CONNOLLY, G. D. *Modelling of the propagation of ultrasound through austenitic steel welds*. Tese (Doutorado) — Imperial College, 2009.
- 4 DISSIMILAR CONSORTIUM. *Phased Array Ultrasonic Inspection of Dissimilar Metal Joints*. [S.l.], 2011. Tech. rep. TSB Project No: P11/MFE/6/I/AA058J.
- 5 LIMTHONGKUL, S. *Validation of wave propagation in austenitic welds using vibrometer*. Dissertação (Mestrado) — Brunel University London, 2015.
- 6 YE, J. et al. Influence of welding passes on grain orientation - The example of a multi-pass V-weld. *International Journal of Pressure Vessels and Piping*, 2012.
- 7 JOHNSTON, C.; NAGESWARAN, C.; LONDON, T. Investigations into the fatigue strength of cra lined pipe. In: *Offshore Technology Conference*. Houston: [s.n.], 2016.
- 8 PAMEL, A. V. *Ultrasonic inspection of highly scattering materials*. Tese (Doutorado) — Imperial College London, London, 2015.
- 9 NAGESWARAN, B. *Phased array ultrasonic techniques for the inspection of inhomogeneous anisotropic materials*. Tese (Doutorado) — University of Birmingham, Birmingham, 2008.
- 10 ZHAO, L.; NAGESWARAN, C. *Modelling and experimental verification of phased array ultrasonic inspection of thick-section austenitic stainless steel welds*. [S.l.], 2016.
- 11 MOYSAN, J. et al. Modelling the grain orientation of austenitic stainless steel multipass welds to improve ultrasonic assessment of structural integrity. *International Journal of Pressure Vessels and Piping*, v. 80, p. 77–85, 2003.
- 12 NAGESWARAN, C.; CARPENTIER, C.; TSE, Y. Y. Improving phased array ultrasonic testing using models to overcome austenitic weld distortion. In: *7th International Conference on NDE in Relation to Structural Integrity for Nuclear and Pressurized Components*. Yokohama: [s.n.], 2009.
- 13 HU, D. et al. Ultrasonic phased array for the circumferential welds safety inspection of urea reactor. *Procedia Engineering*, v. 43, p. 459–463, 2012.
- 14 HOEGH, K.; KHAZANOVICH, L. Extended synthetic aperture focusing technique for ultrasonic imaging of concrete. *NDT&E International*, v. 74, p. 33–42, 2015.
- 15 KIM, D.; BANG, J. Assortment of ultrasonic nondestructive evaluation signals using the centroid searching method with the LMS algorithm and SAFT. *NDT&E International*, v. 44, p. 760–767, 2011.

- 16 CALLISTER Jr, W. D.; RETHWISCH, D. G. *Materials science and engineering an introduction*. Eighth edition. [S.l.]: John Wiley & Sons, 2010.
- 17 CHEN, Y. et al. Modelling of ultrasonic propagation in heavy-walled centrifugally cast austenitic stainless steel based on ebsd analysis. *Ultrasonics*, 2015.
- 18 MASON, W. P.; MCSKIMIN, H. J. Energy losses of sound waves in metals due to scattering and diffusion. *The Journal of the Acoustical Society of America*, v. 99, 1996.
- 19 YE, J.; KIM, H. J.; SONG, S. J. Development of an ultrasonic ray model for phased array ultrasonic testing in austenitic weldments. In: *17th World Conference on Non-destructive Testing*. Shanghai: [s.n.], 2008.
- 20 SHAHJAHAN, S. et al. Improvement of flaw detection with ultrasonic array probes in multiple scattering polycrystalline materials by means of a random matrix approach. In: *13th International Symposium on Non-destructive Characterization of Materials*. Le Mans: [s.n.], 2013.
- 21 DEUTSCHE GESELLSCHAFT FÜR ZERSTÖRUNGSFREIE PRÜFUNG. *Handbook on the ultrasonic examination of austenitic and dissimilar welds*. Düsseldorf: DGZfp/DVS Media, 2008.
- 22 ROSE, J. L. *Ultrasonic guided waves in solid media*. New York: Cambridge University Press, 2014.
- 23 BOND, W. L. The mathematics of the physical properties of crystals. *The Bell System Technical Journal*, v. 22, 1943.
- 24 ROYER, D.; DIEULESAINT, E. *Elastic waves in solids I*. Berlin: Springer, 2000.
- 25 ACHENBACH, J. D. *Wave Propagation in Elastic Solids*. [S.l.]: North-Holland Publishing company, 1973.
- 26 HOLMES, C.; DRINKWATER, B. W.; WILCOX, P. D. Post-processing of the full matrix of ultrasonic transmit–receive array data for non-destructive evaluation. *NDT&E International*, v. 38, p. 701–711, 2005.
- 27 SUTCLIFFE, M. et al. Real-time full matrix capture for ultrasonic non-destructive testing with acceleration of post-processing through graphic hardware. *NDT and E International*, v. 51, p. 16–23, 2012.
- 28 STEPINSKI, T. An implementation of synthetic aperture focusing technique in frequency domain. *IEEE Transactions on Ultrasonics, Ferroelectrics, and Frequency Control*, v. 54, 2007.
- 29 LANGENBERG, K. J. et al. Synthetic aperture focusing technique signal processing. *NDT International*, v. 19, 1986.
- 30 KERR, W.; PIERCE, S. G.; ROWE, P. Investigation of synthetic aperture methods in ultrasound surface imaging using elementary surface types. *Ultrasonics*, v. 72, 2016.
- 31 WESTON, M. *Advanced Ultrasonic Digital Imaging and Signal Processing for Applications in the Field of Non-Destructive Testing*. Tese (Doutorado) — University of Manchester, 2011.

- 32 ZHANG, J.; DRINKWATER, B. W.; WILCOX, P. D. Effects of array transducer inconsistencies on total focusing method imaging performance. *NDT and E International*, v. 44, p. 361–368, 2011.
- 33 ZHANG, J. et al. Defect detection using ultrasonic arrays: The multi-mode total focusing method. *NDT and E International*, v. 43, p. 123–133, 2010.
- 34 GEKKO phased-array flaw detector. Disponível em: <<https://www.m2m-ndt.com/products/Spec%20Gekko.pdf>>. Acesso em: 29 May 2017.
- 35 WESTON, M. et al. Time efficient auto-focussing algorithms for ultrasonic inspection of dual-layered media using full matrix capture. *NDT&E International*, v. 47, p. 43–50, 2012.
- 36 JEUNE, L. L. et al. Plane wave imaging for ultrasonic non-destructive testing: Generalization to multimodal imaging. *Ultrasonics*, v. 64, p. 128–138, 2016.
- 37 PRADA, C. et al. Decomposition of the time reversal operator: Detection and selective focusing on two scatterers. *The Journal of the Acoustical Society of America*, v. 99, 1996.
- 38 BARBIERI, E.; MEO, M. Discriminating linear from nonlinear elastic damage using a nonlinear time reversal DORT method. *International Journal of Solids and Structures*, v. 47, p. 2639–2652, 2010.
- 39 AUBRY, A.; DERODE, A. Random matrix theory applied to acoustic backscattering and imaging in complex media. *Physical Review Letters*, v. 102, 2009.
- 40 AUBRY, A.; DERODE, A. Detection and imaging in a random medium: A matrix method to overcome multiple scattering and aberration. v. 106, 2009.
- 41 CHEN, Y. et al. Modeling of ultrasonic propagation in heavy-walled centrifugally cast austenitic stainless steel based on EBSD analysis. *Ultrasonics*, v. 59, p. 31–39, 2015.
- 42 NAGESWARAN, C.; CARPENTIER, C.; TSE, Y. Y. Microstructural quantification, modelling and array ultrasonics to improve the inspection of austenitic welds. *Insight*, v. 51, 2009.
- 43 APFEL, A. et al. Coupling an ultrasonic propagation code with a model of the heterogeneity of multipass welds to simulate ultrasonic testing. *Ultrasonics*, v. 43, p. 447–456, 2005.
- 44 GUEUDRE, C. et al. Direct model optimisation for data inversion. Application to ultrasonic characterisation of heterogeneous welds. *NDT&E International*, v. 42, p. 47–55, 2009.
- 45 MARK, A. F. et al. Investigation of the elastic/crystallographic anisotropy of welds for improved ultrasonic inspections. *Materials Characterization*, v. 98, p. 47–53, 2014.
- 46 FAN, Z. et al. Nonintrusive estimation of anisotropic stiffness maps of heterogeneous steel welds for the improvement of ultrasonic array inspection. *IEEE Transactions on Ultrasonics, Ferroelectrics, and Frequency Control*, v. 62, p. 1530–1543, 2015.

- 47 CHASSIGNOLE, B. et al. Modelling the attenuation in the ATHENA finite elements code for the ultrasonic testing of austenitic stainless steel welds. *Ultrasonics*, v. 49, p. 653–658, 2009.
- 48 PZFLEX. Disponível em: <<https://pzflex.com/>>. Acesso em: 23 October 2017.
- 49 OGILVY, J. A. Computerized ultrasonic ray tracing in austenitic steel. *NDT International*, 1985.
- 50 CONNOLLY, G. D. et al. The application of Fermat's principle for imaging anisotropic and inhomogeneous media with application to austenitic steel weld inspection. *Proceedings of The Royal Society A*, 2017.
- 51 HLKJÆR, S.; SØRENSEN, M. P.; KRISTENSEN, W. D. The propagation of ultrasound in an austenitic weld. *Ultrasonics*, v. 38, 2000.
- 52 NOWERS, O. et al. Novel ray-tracing algorithms in NDE: Application of Dijkstra and A* algorithms to the inspection of an anisotropic weld. *NDT&E International*, v. 61, 2014.
- 53 CIVA in a few words. Disponível em: <<http://www.extende.com/civa-in-a-few-words>>. Acesso em: 20 May 2017.
- 54 HOLLMAN, K. W.; RIGBY, K. W.; O'DONNELL, M. Coherence factor of speckle from a multi-row probe. In: *1999 IEEE Ultrasonics Symposium*. Lake Tahoe: [s.n.], 1999.
- 55 MALLART, R.; FINK, M. Adaptive focusing in scattering media through sound-speed inhomogeneities: The van Cittert Zernike approach and focusing criterion. *Journal of The Acoustical Society of America*, v. 96, 94.
- 56 KNIGHT-GREGSON, B. et al. Improvement of ultrasonic cross-sectional imagery via the application of coherence weighting and the total focussing method. In: *"55th Annual Conference of the British Institute for Non-Destructive Testing*. Nottingham: [s.n.], 2016.
- 57 GUO, W.; WANG, Y.; YU, J. Ultrasound harmonic enhanced imaging using eigenspace-based coherence factor. *Ultrasonics*, v. 72, p. 106–116, 2016.
- 58 SHEN, C.; XING, Y.; JENG, G. Autocorrelation-based generalized coherence factor for low-complexity adaptive beamforming. *Ultrasonics*, v. 72, p. 177–183, 2016.
- 59 CAMACHO, J.; PARRILLA, M.; FRITSCH, C. Phase coherence imaging. *IEEE Transactions on Ultrasonics, Ferroelectrics, and Frequency Control*, v. 56, p. 958–974, 2009.
- 60 CRUZA, J. F.; CAMACHO, J.; FRITSCH, C. Plane-wave phase-coherence imaging for NDE. *NDT&E International*, v. 87, p. 31–37, 2017.
- 61 FRITSCH, C.; CAMACHO, J.; PARRILLA, M. New ultrasound imaging techniques with phase coherence processing. *Ultrasonics*, v. 50, p. 122–126, 2010.
- 62 LU, S. et al. Real-time monitoring of controllable cavitation erosion in a vessel phantom with passive acoustic mapping. *Ultrasonics - Sonochemistry*, v. 39, p. 291–300, 2017.

- 63 ZHANG, J.; DRINKWATER, B. W.; WILCOX, P. D. Comparison of ultrasonic array imaging algorithms for nondestructive evaluation. *IEEE Transactions on Ultrasonics, Ferroelectrics, and Frequency Control*, v. 60, p. 1732–1745, 2013.
- 64 PAMEL, A. V. et al. Numerical simulations of ultrasonic array imaging of highly scattering materials. *NDT and E International*, v. 81, p. 9–19, 2016.
- 65 DANDEKAR, D. P.; MARTIN, A. G. Single crystal elastic constants of two nickel based superalloys. *Journal of Materials Science Letters*, v. 8, p. 1172–1173, 1989.
- 66 DANDEKAR, D. P.; MARTIN, A. G. Temperature dependence of flexural and torsional elastic constants of two nickel-based superalloys. *Journal of Materials Science*, v. 25, p. 3321–3326, 1990.
- 67 KELLER, C.; HABRAKEN, A. M.; DUCHENE, L. Finite element investigation of size effects on the mechanical behavior of nickel single crystals. *Materials Science and Engineering A*, v. 550, p. 342–349, 2012.
- 68 LANE, C. *The Development of a 2D Ultrasonic Array Inspection for Single Crystal Turbine Blades*. Tese (Doutorado) — University of Bristol, 2013.
- 69 CASTAGNÈDE, B. et al. Optimal determination of the elastic constants of composite materials from ultrasonic wave-speed measurements. *Journal of applied Physics*, v. 67, p. 2753–2761, 1990.
- 70 EVERY, A. G.; SACHSE, W. Determination of the elastic constants of anisotropic solids from acoustic-wave group-velocity measurements. *Physical Review B*, v. 42, n. 13, p. 8196–8205, 1990.
- 71 BARAZANCHY, D.; ROTH, W.; GIURGIUTIU, V. A non-destructive material characterization framework for retrieving a stiffness matrix using bulk waves. *Composite Structures*, v. 185, p. 27–37, 2018.
- 72 PENG, Q. et al. Effect of chemical composition on grain boundary microchemistry and stress corrosion cracking in alloy 182. *Corrosion Science*, v. 67, p. 91–99, 2013.
- 73 WANG, C.; MING, W.; CHEN, M. Milling tool's flank wear prediction by temperature dependent wear mechanism determination when machining Inconel 182 overlays. *Tribology International*, v. 104, p. 140–156, 2016.
- 74 WANG, F.; MA, D.; BÜHRING-POLACZEK, A. Microsegregation behavior of alloying elements in single-crystal nickel-based superalloys with emphasis on dendritic structure. *Materials Characterization*, v. 127, p. 311–316, 2017.
- 75 JUVA, A.; LENKKERI, J. The effect of anisotropy on the propagation of ultrasonic waves in austenitic stainless steel. In: *Proceedings of the Specialists' Meeting on Reliability of the Ultrasonic Inspection of Austenitic Materials*. Brussels: [s.n.], 1980.
- 76 MATHERS, G. Ultrasonic examination part 2. *TWI*. Disponível em: <<http://www.twi-global.com/technical-knowledge/job-knowledge/ultrasonic-examination-part-2-128/>>. Acesso em: 13 Dec 2017.
- 77 DIAS, J. C. S. *Imagen ultrasónica por coherencia de fase*. Tese (Doutorado) — Universidad Complutense de Madrid, Madrid, 2011.

- 78 DENNIEL, S.; TKACZYK, T.; PEPIN, A. Reeled mechanically lined pipe: cost efficient solution for static and dynamic applications in corrosive environment. In: *Deep Offshore Technology Conference*. Perth: [s.n.], 2012.
- 79 MECHANICALLY lined pipes – the BuBi® pipe. Disponível em: <<https://www.butting.com/en/mechanically-lined-pipes/>>. Acesso em: 27 October 2017.
- 80 WILMOT, D.; MONTAGUE, P. The suitability of CRA lined pipes for flowlines susceptible to lateral buckling. In: *SUT Global Pipeline Buckling Symposium*. Perth: [s.n.], 2011.
- 81 TKACZYK, T.; PÉPIN, A.; DANNIEL, S. Fatigue and fracture of mechanically lined pipes installed by reeling. In: *International Conference on Ocean, Offshore and Arctic Engineering*. Rio de Janeiro: [s.n.], 2012.
- 82 TWO-SAMPLE Kolmogorov-Smirnov test. Disponível em: <<http://uk.mathworks.com/help/stats/kstest2.html>>. Acesso em: 19 November 2017.
- 83 MAITLAND, T.; SITZMAN, S. Electron backscatter diffraction (EBSD) technique and materials characterization. In: ZHOU, W.; WANG, Z. L. (Ed.). *Scanning Microscopy for Nanotechnology: Techniques and Applications*. New York: Springer, 2006. cap. 2.
- 84 WRIGHT, S. I. et al. Electron imaging with an EBSD detector. *Ultramicroscopy*, v. 148, p. 132–145, 2015.
- 85 TAYLOR, J. R. *An Introduction to Error Analysis*. 2. ed. Sausalito: University Science Books, 1997.
- 86 DROSG, M. *Dealing with Uncertainties*. Berlin: Springer, 2007.
- 87 HUGHES, I. F.; HASE, T. P. A. *Measurements and their Uncertainties*. New York: Oxford University Press, 2010.
- 88 BERENDSEN, H. J. C. *A student's guide to data and error analysis*. Cambridge: Cambridge University Press, 2011.
- 89 BARLOW, R. J. *Statistics*. Chichester: John Wiley & Sons, 1989.

Appendix

APPENDIX A – EBSD introduction and methodology

In order to make this thesis more self-sufficient, this appendix gives a brief introduction to EBSD, followed by further details about the EBSD measurements and data processing conducted during the DISSIMILAR project whose results were also used in this thesis.

A.1 Introduction to EBSD

Electron Backscatter Diffraction (EBSD) is a technique associated with the Scanning Electron Microscope (SEM) capable of assessing the grain orientation information from the sample being analysed (83, 84). According to Maitland and Sitzman (83), the EBSD images are obtained from a flat, highly polished sample positioned with the normal of its surface at 70° from the incident electron beam. The interaction of the beam with the lattice induces the formation of an interference pattern in the backscattered electrons that can be detected by a phosphor screen, known as Kikuchi pattern after Seishi Kikuchi, who, alongside Shoji Nishikawa, first observed this phenomenon.

The processing of Kikuchi pattern data is conducted by dedicated computer software, which reports the phase and orientation of the sample. This is accomplished by employing a Hough transform to identify the position of the Kikuchi bands. From the calibrated data it is possible to obtain the angles between the planes and comparing those with a list of interplanar angles for the specific crystal structure being analysed. The final result is usually given in terms of Euler angles from the coordinate axis fixed in the sample (4, 83).

The EBSD results are provided as a set of Euler angles ϕ_1 , ϕ and ϕ_2 and need to be converted to the angle rotation notation around the sample's axis defined by the angles α , β and γ (4) defined in Subsection 3.2.2. This transformation is necessary to represent

the angles correctly in the modelling software. To accomplish this, one needs to obtain the equivalent version of Equation 3.23 for rotation sequence used by the EBSD equipment, make both \mathbf{R} matrices equal and solve for the unknown angles. The matrix \mathbf{R} is defined in Equation A.1 for the Euler angles used to describe the crystallographic orientations of the EBSD.

$$\mathbf{R}_{ij} = \begin{bmatrix} \cos(\phi_2)\cos(\phi_1) - \cos(\Phi)\sin(\phi_2)\sin(\phi_1) & \cos(\phi_2)\sin(\phi_1) + \cos(\Phi)\sin(\phi_2)\cos(\phi_1) & \sin(\phi_2)\sin(\Phi) \\ -\cos(\phi_1)\sin(\phi_2) - \cos(\phi_2)\cos(\Phi)\sin(\phi_1) & -\sin(\phi_2)\sin(\phi_1) + \cos(\phi_2)\cos(\Phi)\sin(\phi_1) & \cos(\phi_2)\sin(\Phi) \\ \sin(\Phi)\sin(\phi_1) & -\sin(\Phi)\cos(\phi_1) & \cos(\Phi) \end{bmatrix} \quad (\text{A.1})$$

A.2 EBSD methodology

As stated in Section 4.1.3, the resolution of the EBSD measurements taken from the block was set to be 40 μm . This number was chosen in order to reduce the time and cost of the EBSD analysis by leaving out of the analysis small changes in the crystallographic orientation unable to significantly scatter the ultrasonic beam. Nonetheless, even with a grid resolution of 40 μm , the area to be scanned (83.5 mm x 35 mm) required more than 1.8 million measurement points¹. This number of measurement points needed to be reduced in order to be introduced into the modelling software. In order to help to solve this issue the *orientation unification* processing step was created (4). It consisted of the selection of the misorientation range and of the identification of the major orientations that could represent the weld.

The misorientation range can be defined as the orientation range inside which adjacent measurement points can vary and still be considered to belong to the same grain. The need to unify the orientations inside a grain also raises from the impossibility to model orientation variation inside a grain in a software such as CIVA² which was extensively used during the DISSIMILAR project. The criterion to define the misorientation range

¹The original region analysed had 3.8 million sampling points, however only a fraction of the original image was used in this thesis

²A semi-analytical software, such as CIVA, requires closed, well defined homogeneous representation of grains to properly work.

was the maximum angle range in which the smallest grains were around the same size of the minimum scatterer; for the EBSD data used in this thesis such angle range is 20° .

On the other hand, the number of significant orientations was optimised via statistical analysis to be eleven. However, unlikely the original study (4), in the block used in the present work the buttering is mostly absent, and the number of major orientations can be reduced even further to only six, as it is presented in Table 1.

APPENDIX B – Confidence interval and uncertainty propagation

This appendix is intended to give further details about the statistical analysis used to handle the data presented in Section 5.1.1. Firstly, it will be presented the best estimate for the population mean and standard deviation according to Taylor (85). Next, the confidence interval calculation method will be introduced followed by a brief description of the uncertainty propagation calculation method using both an analytical and the Monte Carlo methods.

B.1 Best estimate for the population mean and standard deviation

For a finite set of measurements of a generic quantity X , it is not possible to determine its value nor the standard deviation of the limiting distribution, but only estimate them (85). It is demonstrated by Taylor (85) that if the measured values $\chi_1, \chi_2, \dots, \chi_N$ follow a normal distribution the best estimate of X and σ are the ones which the observed $\chi_1, \chi_2, \dots, \chi_N$ are most likely. The maximum likelihood occurs when the exponent of Equation B.1 is minimum.

$$Prob(\chi_1, \chi_2, \dots, \chi_N) \propto \frac{1}{\sigma^N} e^{-\sum_{i=1}^N \frac{(x_i - X)^2}{2\sigma^2}} \quad (\text{B.1})$$

To find the minimum value of the exponent one can find the derivative of $\sum_{i=1}^N \frac{(x_i - X)^2}{\sigma^2}$ and set it to be equal zero, leading to Equation B.2.

$$\sum_{i=1}^N (x_i - X) = 0 \quad (\text{B.2})$$

Since the estimate of X is constant, it is possible to take it out of the summation. After rearranging the results, one obtains Equation B.3, which is the mean of the measurements.

$$X_{best} = \bar{x} = \frac{\sum_{i=1}^N x_i}{N} \quad (\text{B.3})$$

For the population standard deviation estimation, the procedure is equivalent to the one adopted for the mean; initially, Equation B.1 is differentiated with respect to the population standard deviation σ followed by setting the result equal to zero. Those steps will result in the sample standard deviation equation, here presented as Equation B.4.

$$\sigma_{best} = \sigma = \sqrt{\frac{1}{N-1} \sum_{i=1}^N (x_i - X_{best})^2} \quad (\text{B.4})$$

Another important parameter, the standard deviation of the mean, is introduced in Equation B.5 below. This parameter represents the uncertainties presented in the measurements χ_i and, as a consequence, how reliable the mean is. Unlike the standard deviation, σ , the standard deviation of the mean σ_m can change significantly with the number of measurements made. The proof of Equation B.5, which describes the standard deviation of the mean, can be obtained by applying the error propagation principle described in Section B.3.

$$\sigma_m = \frac{\sigma}{\sqrt{N}} \quad (\text{B.5})$$

B.2 Confidence interval using Student's t distribution

For large data samples, the distribution is often close enough to be represented by the normal distribution. This simplification can be used because the data distribution gets close to a Gaussian curve. However, when the data sample is relatively small, distortions take place and can significantly impair the results (86). For those cases, it is an ordinary practice to represent the distribution as a Student t distribution. This distribution is close

to a Gaussian curve for large data samples, but it gets wider for smaller sample sizes, thus compensating for the reduction of the statistical confidence.

It is possible to use the Student's t_s factor in order to correct the standard deviation calculated by Equation B.4. This factor is often found in the format of a table which gives the t_s factor from the magnitude of the confidence and the number of degrees of freedom (number of independent data values (86,87)). Variations of the Student's t_s factor table can be found in references (86,88), the t_s values used in the present thesis come from those sources. Drogg (86) illustrates the usage of those tables using the following example:

When using only six independent data points, 68.27% of the data are situated in an interval of $\pm 1.11\sigma$ (instead of $\pm 1\sigma$), for 95.45% of the data to be inside of this interval its size has to be $\pm 2.57\sigma$ (instead of $\pm 2\sigma$), and to reach a confidence level of 99.73%, the interval has to be $\pm 5.51\sigma$ (instead of $\pm 3\sigma$).

To calculate the confidence interval, Barlow (89) uses the mean of the data plus and minus the standard deviation of the mean (Equation B.5) multiplied by the corresponding t_s factor, expound here in Equation B.6 below:

$$\text{Confidence interval} = \bar{x} \pm t_s \frac{\sigma}{\sqrt{N}}. \quad (\text{B.6})$$

The results obtained with Equation B.6 do not mean that there is a given probability, chosen in a Student's t_s factor table, of the interval containing the true mean. Instead, that percentage refers to the probability of repeated experiments carried out in the same way to contain the true mean.

B.3 Error propagation

It is common to find quantities that cannot be measured directly, such as the stiffness matrix of the single crystal, whose measurements results are presented in Chapter 5. In such cases other quantity or quantities of which the quantity of interest is a function needs to be measured, followed by the usage of one or more equations to finally obtain the desired quantity (85,88). Here, it is described the general approach to determine how the

uncertainties of the measured quantities propagate into the equations and how to estimate the resulting uncertainties in the quantity of interest based on the work of Taylor (85), Drogg (86) and Hughes (87).

Assuming a quantity q as a function of X , it was demonstrated that the best estimate for X is $\bar{\chi}$ and by assuming an uncertainty of $\delta\chi$, it is possible to state that $X = \bar{\chi} \pm \delta\chi$. Then, the uncertainty in q , δq , can be defined by Equation B.7.

$$\delta q = q(\bar{\chi} + \delta\chi) - q(\bar{\chi}) \quad (\text{B.7})$$

Considering $\delta\chi$ to be small it is possible to state that the value of δq is:

$$\delta q = \left| \frac{\partial q}{\partial \chi} \right| \delta \chi \quad (\text{B.8})$$

The vertical bars indicating the absolute value of $\partial q / \partial \chi$ were added because just one side of the uncertainty is used in the calculation (the uncertainty is symmetrical) and its derivative can be negative.

On the other hand, for quantities that are functions of more than one measurable quantity the uncertainties of each measured quantity need to be combined in order to obtain the final uncertainty. Combining uncertainties of different variables, such as those present in C_{11} , C_{44} , ρ and $V_{L<110>}$ when solving Equation 3.9 for C_{12} is not straightforward as for when there is only one quantity with uncertainty (85, 87). Nonetheless, Hughes (87) demonstrated that if the variables whose uncertainties are to be combined are not correlated, the combination can be done by calculating the square root of the summation of the squared individual uncertainties, this is presented in Equation B.9.

$$\delta q = \sqrt{\left(\frac{\partial q}{\partial \chi_1} \delta \chi_1 \right)^2 + \left(\frac{\partial q}{\partial \chi_2} \delta \chi_2 \right)^2 + \dots + \left(\frac{\partial q}{\partial \chi_N} \delta \chi_N \right)^2} \quad (\text{B.9})$$

Where χ_i represent the input quantities, i.e. for the Equation 3.9 example it would be the C_{11} , C_{44} , ρ and $V_{L<110>}$ quantities.

Equation B.9 is the lower limit for δq , which considers $\delta\chi_i$ to be independent among themselves. In addition to this, the upper limit of δq can be calculated by directly adding $\delta\chi_i$; this can be visualised in Equation B.10

$$\delta q = \frac{\partial q}{\partial \chi_1} \delta \chi_1 + \frac{\partial q}{\partial \chi_2} \delta \chi_2 + \dots + \frac{\partial q}{\partial \chi_N} \delta \chi_N \quad (\text{B.10})$$

Equation B.10 calculates the uncertainty for the extreme case of total dependence among $\delta\chi_i$ quantities. For intermediate cases between Equations B.9 and B.10, it is required to calculate the covariance between the variables (85). The covariance, or how two variables depend on one another (89), is not simply calculated for the present case, since individual measurements of one variable have no counterparts on the other. A solution for the error calculation in an equation such as Equation 3.9 can be achieved via the Monte Carlo method (88).

To apply Monte Carlo method, according to Herman (88) it is required to know the mean and standard deviation of all the input quantities; followed by the generation of distributions with the same mean and standard deviation. Next, all the possible combinations between the generated distributions samples are fed to the equation in order to obtain a distribution of results whose mean, standard deviation and confidence interval for a given confidence level can be obtained. In Section 5.1.1 it is presented the uncertainties of C_{12} calculated both by the Monte Carlo method and Equation B.9.

APPENDIX C – Complementary images

Here some complementary images to those presented in Chapter 5 are shown. Figures 68, 69, 70 and 71 follow Figure 60 from Subsection 5.2.1. While Figures 72, 73, 74, 75, 76 and 77 follow Figure 67 from Subsection 5.2.2 .

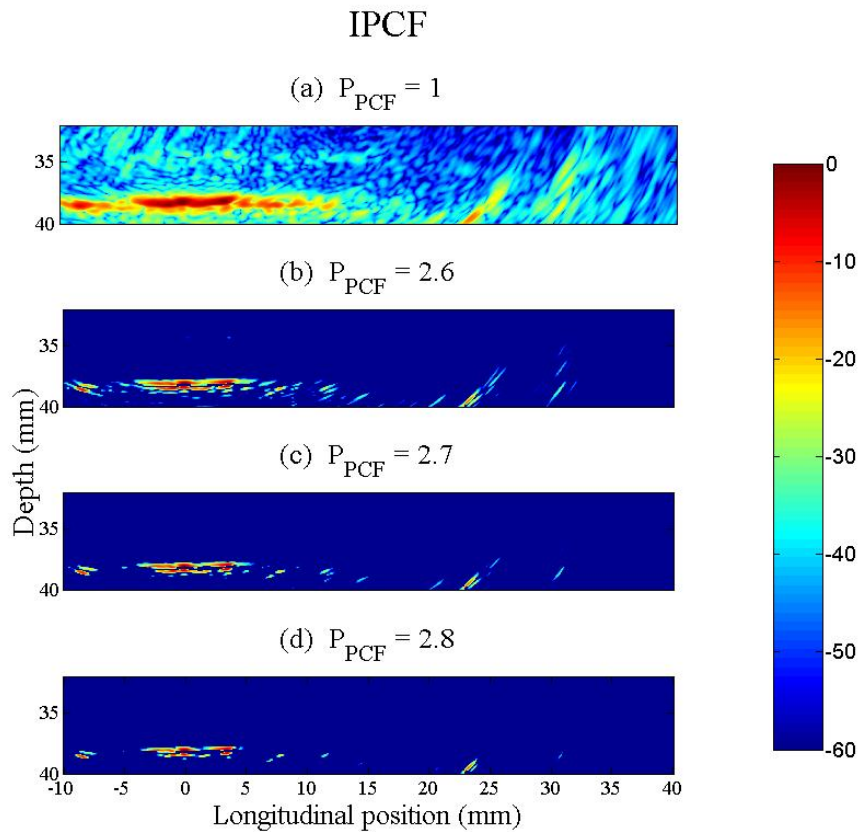


Figure 68 – IPCF images for several P_{PCF} from the 1.6 mm deep notch using the 10 MHz probe. Source: the author.

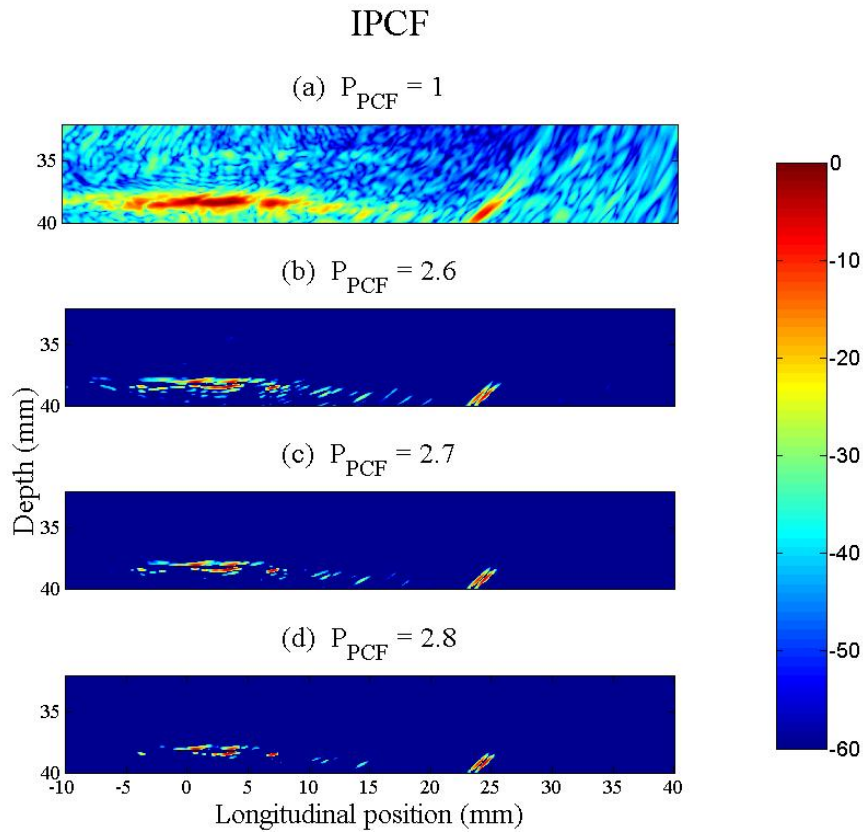


Figure 69 – IPCF images for several P_{PCF} from the region without any notch using the 10 MHz probe. Source: the author.

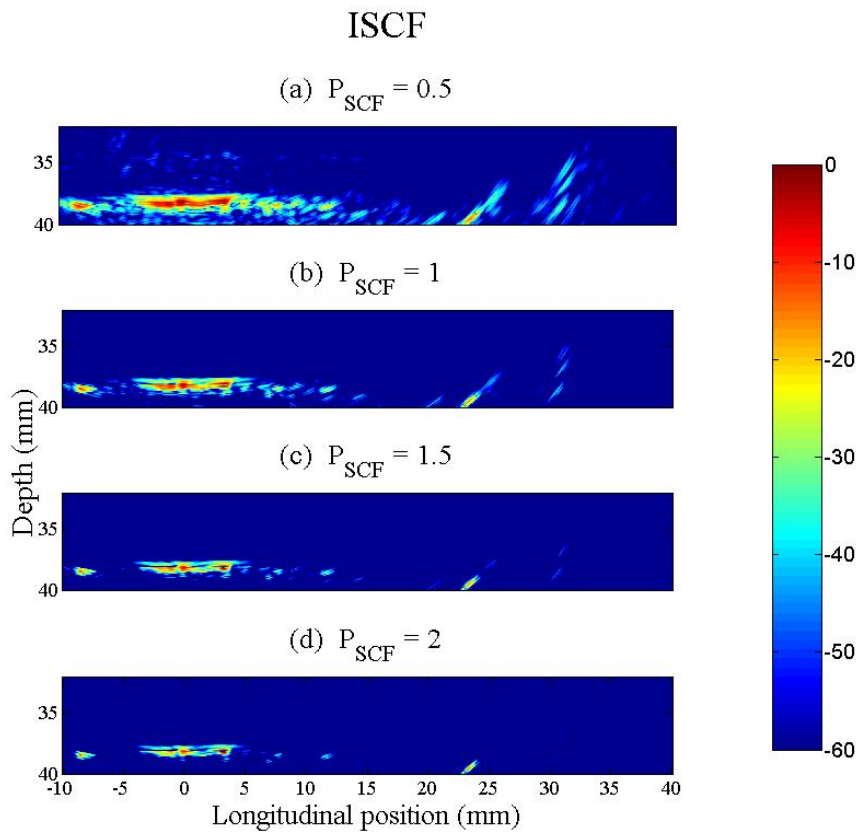


Figure 70 – ISCF images for several P_{SCF} from the 1.6 mm deep notch using the 10 MHz probe. Source: the author.

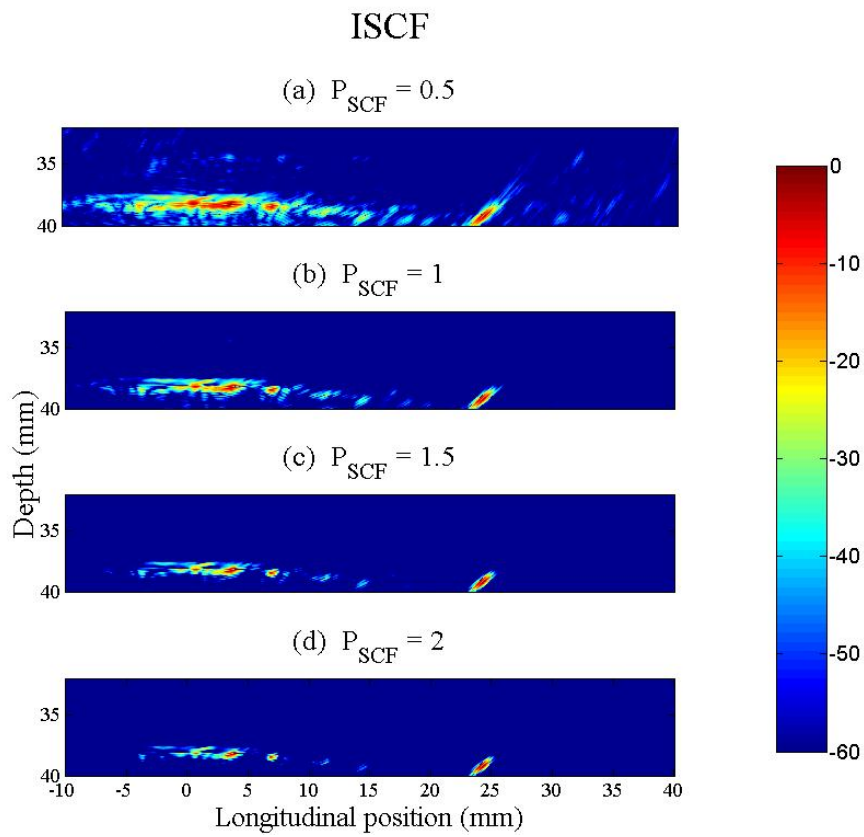


Figure 71 – ISCF images for several P_{SCF} from the region without any notch using the 10 MHz probe. Source: the author.

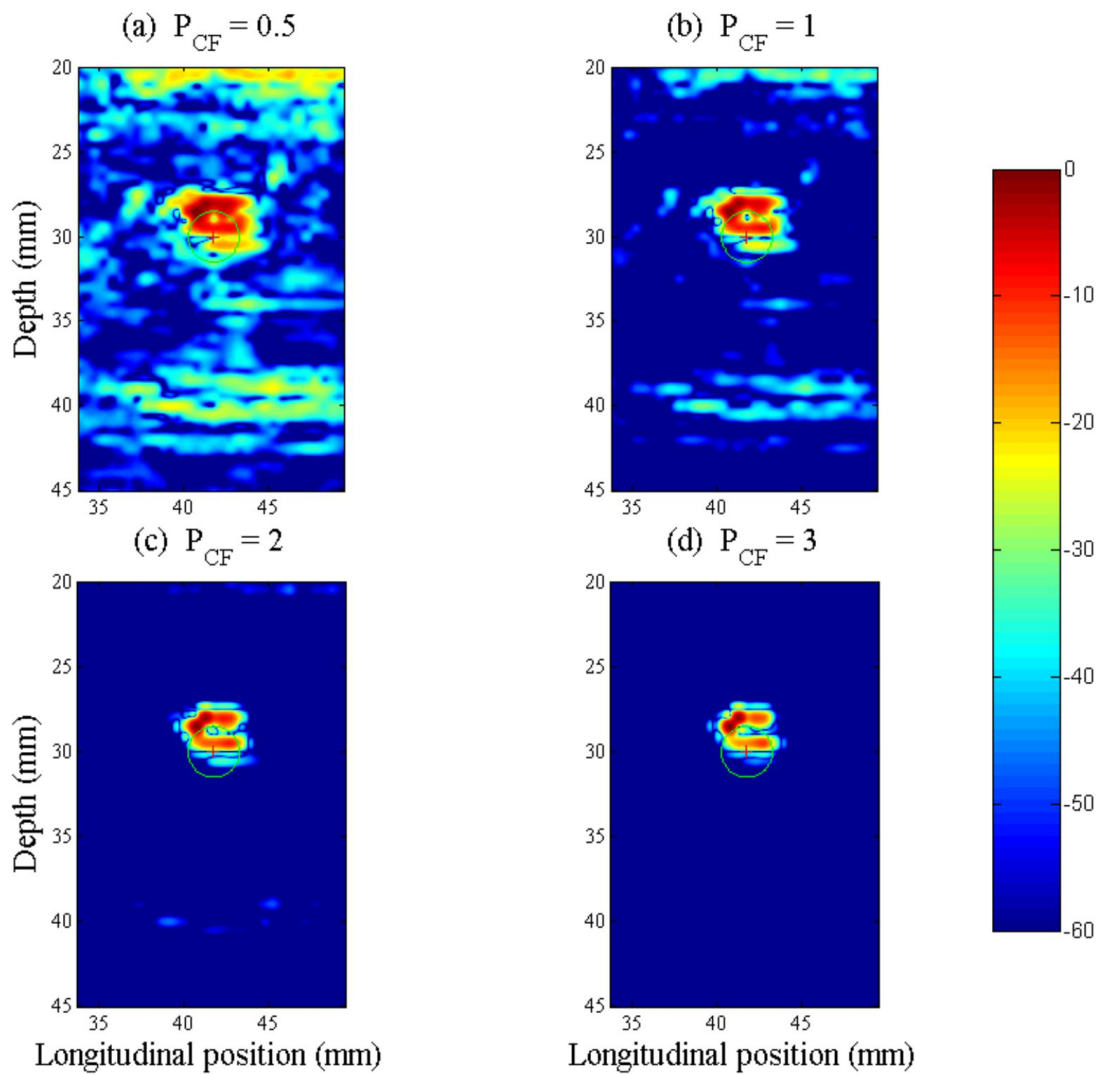


Figure 72 – ICF applied to the ADTFM image of the dissimilar weld block for four sensibility factor amplitudes. This image was obtained from the ADTFM image presented in Figure 51 (b). Source: the author.

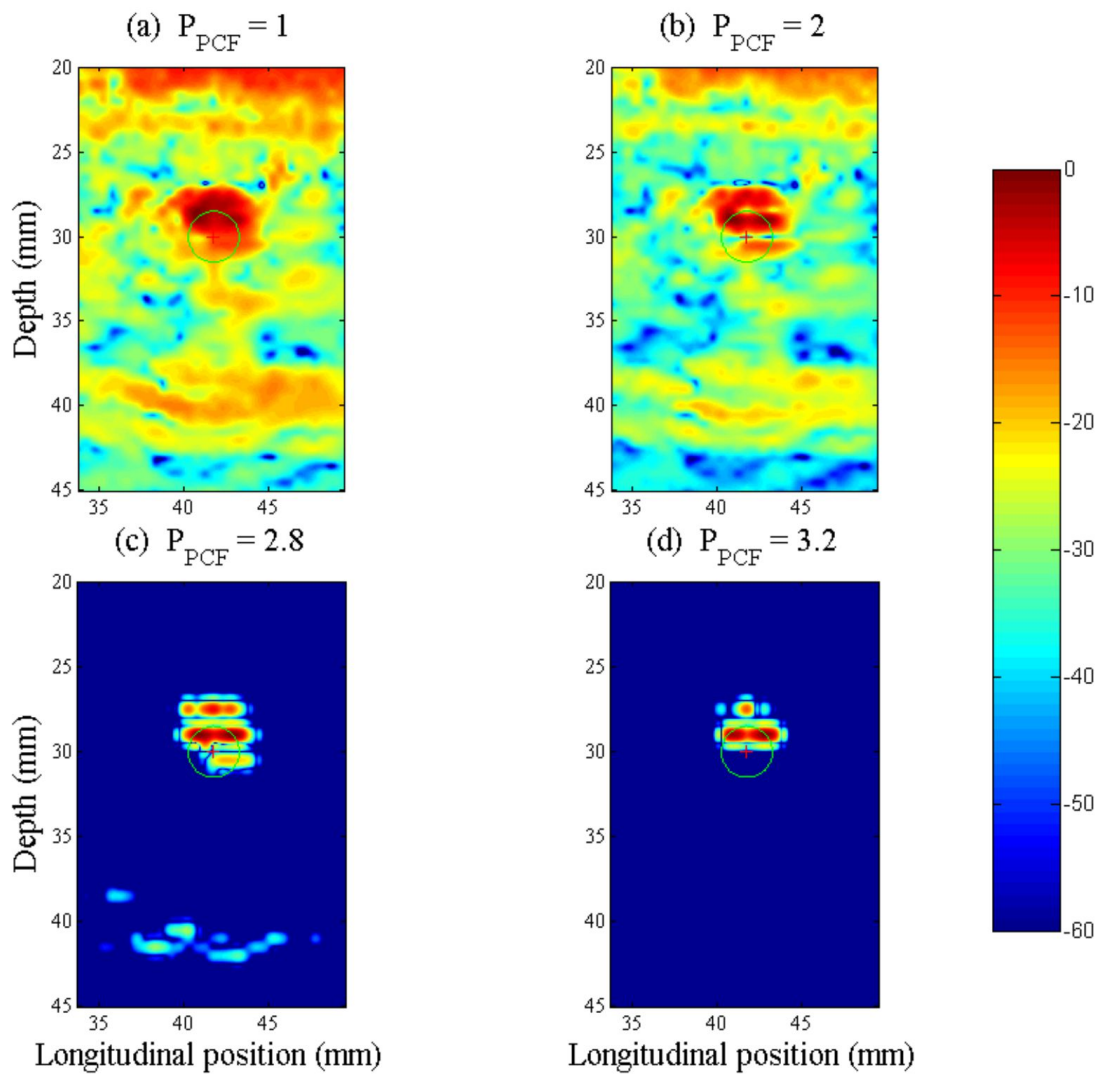


Figure 73 – IPCF applied to the ADTFM image of the dissimilar weld block for four sensibility factor amplitudes. This image was obtained from the ADTFM image presented in Figure 51 (b). Source: the author.

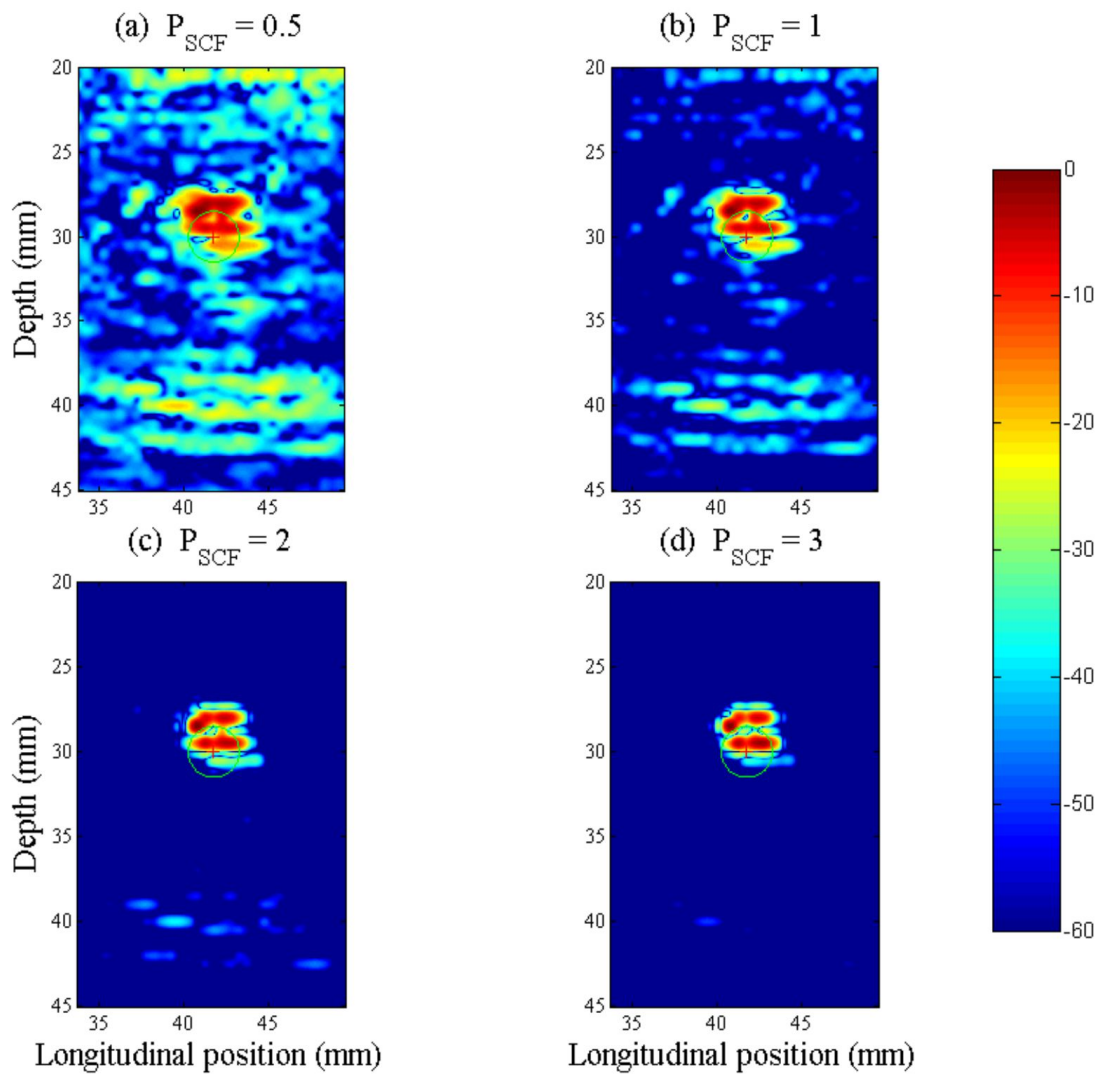


Figure 74 – ISCF applied to the ADTFM image of the dissimilar weld block for four sensibility factor amplitudes. This image was obtained from the ADTFM image presented in Figure 51 (b). Source: the author.

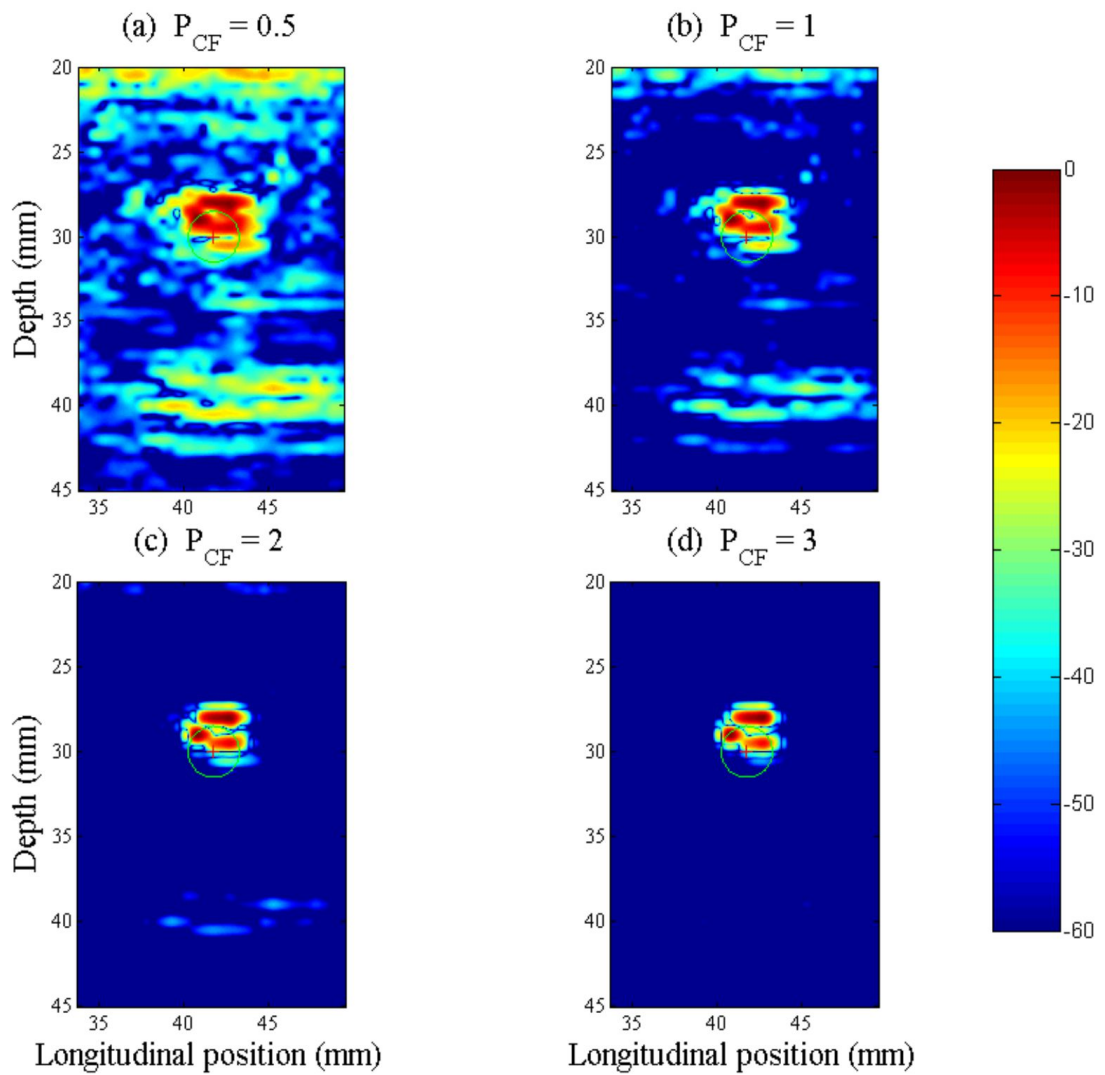


Figure 75 – ICF applied to the ADTFM image of the dissimilar weld block for four sensibility factor amplitudes. This image was obtained from the ADTFM image presented in Figure 51 (c). Source: the author.

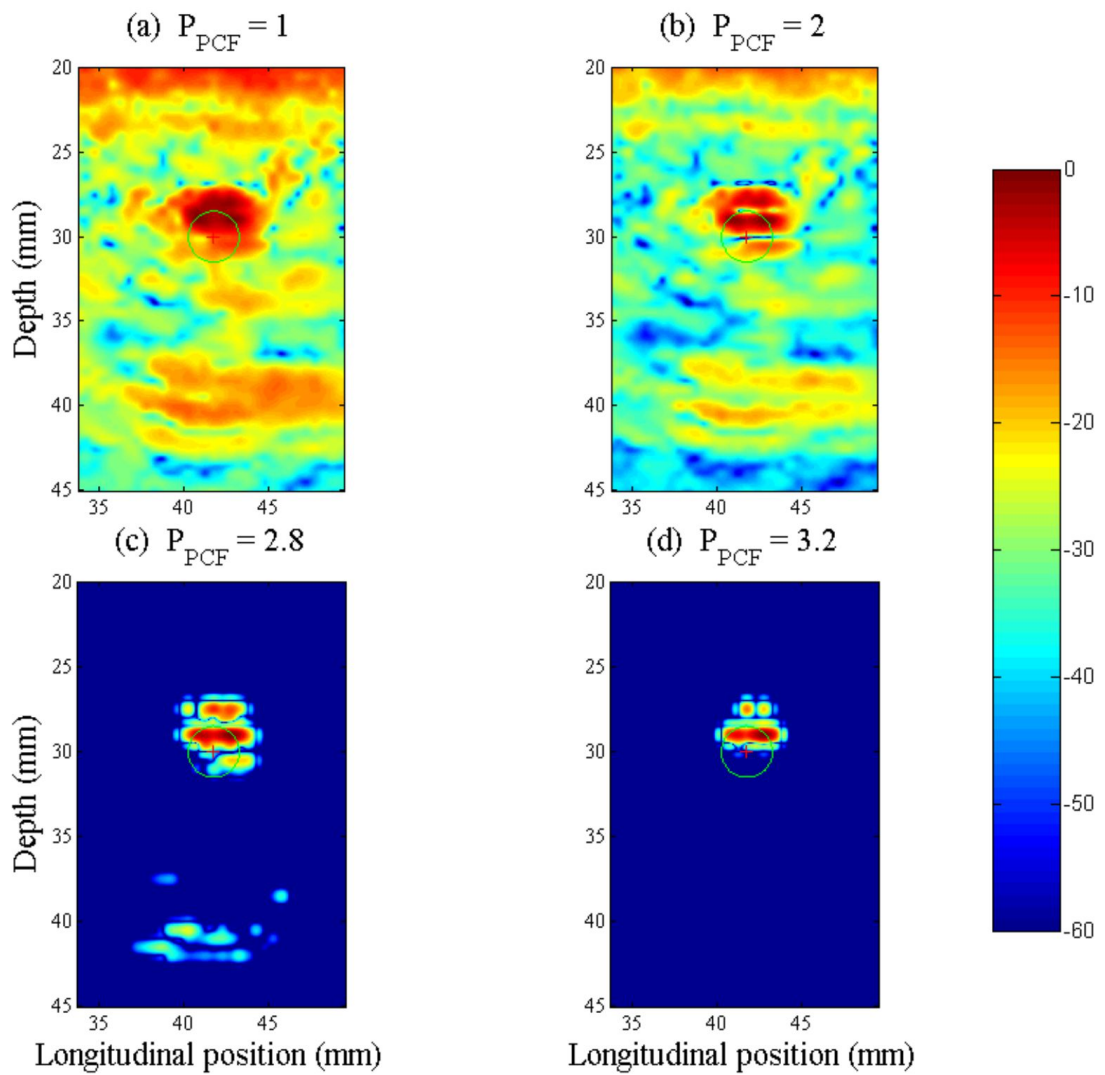


Figure 76 – IPCF applied to the ADTFM image of the dissimilar weld block for four sensibility factor amplitudes. This image was obtained from the ADTFM image presented in Figure 51 (c). Source: the author.

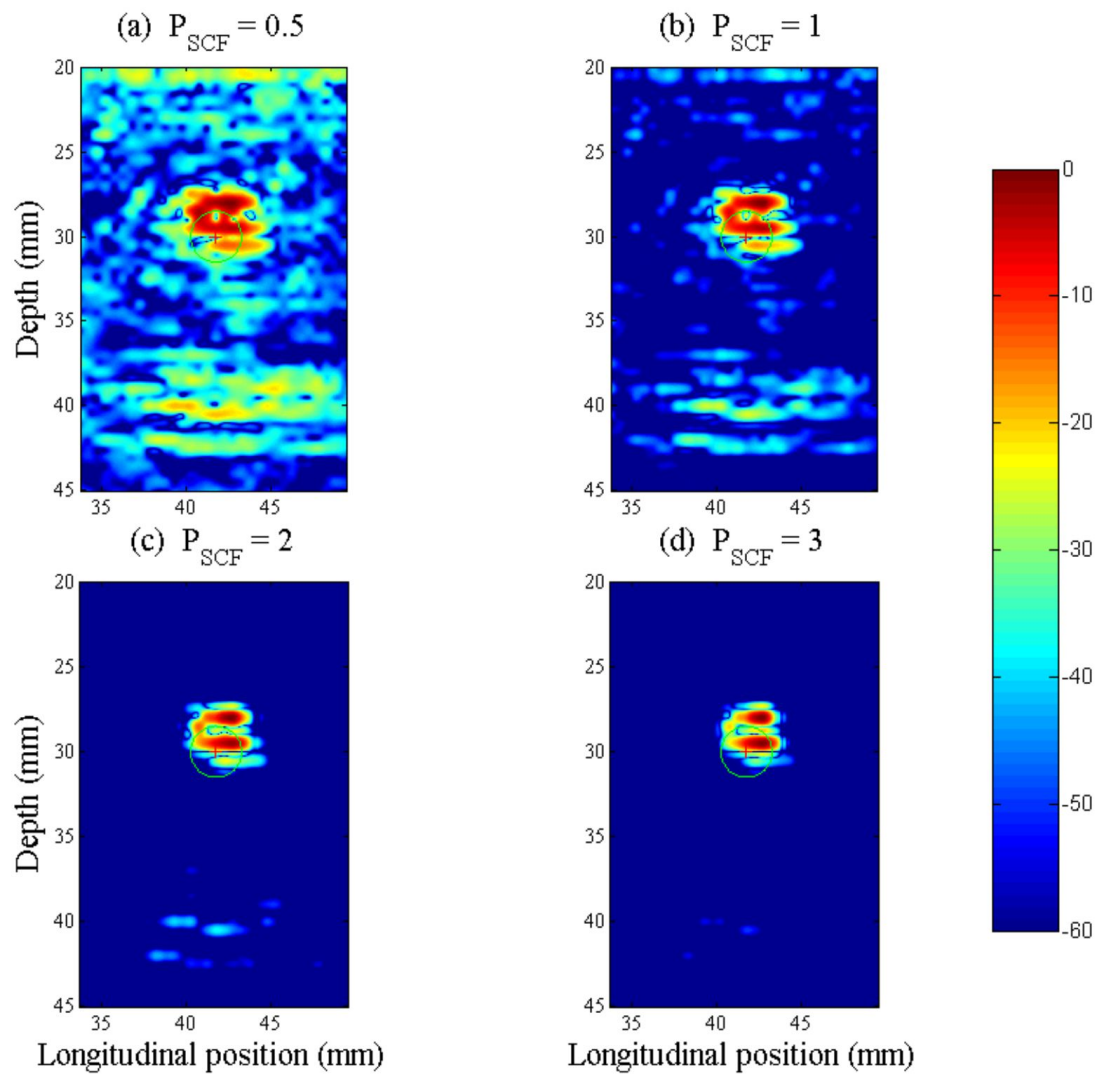


Figure 77 – ISCF applied to the ADTFM image of the dissimilar weld block for four sensibility factor amplitudes. This image was obtained from the ADTFM image presented in Figure 51 (c). Source: the author.